# Lyman alpha forest power spectrum in effective field theory

Mikhail M. Ivanov[*]

*Center for Theoretical Physics, Massachusetts Institute of Technology,
Cambridge, Massachusetts 02139, USA*

We derive an effective field theory (EFT) for cosmological Lyman alpha forest fluctuations valid for the power spectrum at the one-loop order. The "bottom-up" EFT expansion at the level of the transmitted flux is identical to the line-of-sight dependent bias model first derived by Desjacques *et al.* We confirm this result by a "top-down" derivation based on the exponential map of the optical depth field. Specifically, we show that the combination of the exponential map and conditions of renormalizability generates the same EFT expansion as the "bottom-up" approach. In passing, we point out inconsistencies of the tree-level perturbative expansion of the exponential map without counterterms. To facilitate practical applications, we generalize the FFTLog method for efficient calculations of one-loop integrals from new line-of-sight dependent operators. Finally, we compare the one-loop EFT model against data from the Sherwood hydrodynamic simulation. The theory fits the data with subpercent accuracy up to $k = 3 \, h \, \mathrm{Mpc}^{-1}$ at $z = 2.8$ for both 3D and 1D correlations. Our model can be readily used for cosmological full-shape analyses of Lyman alpha forest data.

## I. INTRODUCTION

The Lyman alpha forest is the key source of information on the matter power spectrum at small scales ($\sim$Mpc and smaller) and high redshifts, $2 \lesssim z \lesssim 5$ [1–6]. It has been extensively used to constrain the $\Lambda$CDM model [7–15], as well as neutrino masses [12,16–19], primordial black hole dark matter [20], dark-matter baryon interactions [21], and other nonminimal cosmological models [22–24]. The forest is also a unique probe of warm dark matter [25–34] and fuzzy dark matter models [35–37] that is not affected by ambiguities of the galaxy formation physics. In addition, the large-scale Lyman alpha forest is a valuable source of high-redshift baryon acoustic oscillation (BAO) information, see e.g. [38–41]. In addition to the BAO, the broadband shape of the large-scale 3D Lyman alpha power spectrum may also be a powerful probe of cosmology [42–45].

The Lyman alpha forest has been one of the key targets for past and ongoing large-scale structure surveys such as BOSS [15,46], eBOSS [41], XQ-100 [14], MIKE/HIRES [28], and DESI [45,47,48]. Entering the regime of high-precision Lyman alpha cosmology with DESI requires a robust theoretical understanding of the forest. The standard approach to the forest modeling has been hydrodynamical simulations, see e.g. [49–56]. In this work we explore an alternative method and study to what extent the Lyman alpha fluctuations can be modeled perturbatively [19,22,57–60].

On the one hand, perturbative approaches break down at short scales, where the power spectrum is fully nonlinear, which ultimately limits their utility. On the other hand, they provide a high level of accuracy and flexibility on mildly nonlinear scales. Indeed, as long as the EFT formally applies,[1] it gives a systematic program of consecutive approximations that can be executed to arbitrary accuracy. The high flexibility of the EFT is especially important for the efficient exploration of beyond-$\Lambda$CDM models. For example, it is currently unfeasible to run a full simulation-based Monte Carlo analysis of a large grid of $\Lambda$CDM extensions similar to the analysis by the Planck Collaboration [61].[2] Such an analysis, is, however, perfectly possible with perturbation theory-based pipelines analogous to the ones recently applied to galaxy clustering data, see e.g. [67–78]. In addition, perturbative descriptions are based on different assumptions than simulations. In principle, they provide alternative first-principle models that are agnostic about the physics of intergalactic medium.[3] Therefore, they represent a valuable addition to the Lyman alpha cosmology toolbox.

---

[1]The conditions of the applicability of the EFT will be specified shortly.

[2]Although recently there has been significant progress in cosmological analyses of Lyman alpha forest beyond $\Lambda$CDM based on approximating, interpolating [17,62,63] and emulating [64–66] a grid of simulations.

[3]See [79,80] for relationship between the underlying physics of the Lyman alpha forest and perturbation theory parameters.

[*]ivanov99@mit.edu

The aim of this work is to develop an effective field theory (EFT) description for the Lyman alpha forest, analogous to that of other large-scale structure tracers [81–85]. The main philosophy of the EFT is to describe dynamics on large scales using only relevant symmetries. These ideas have been explored before both in the context of the Lyman alpha forest [22,58,59] and for general line-of-sight dependent bias tracers [86]. In particular, our work is a direct extension of Refs. [59,86]. Desjacques *et al.* [86] derived a general perturbative model for a tracer of matter that depends on the line-of-sight selection effects. Although this description has been developed primarily in the context of galaxies [87], one can argue that it applies, practically without modifications, to the Lyman alpha forest. This is quite natural, as the EFT bias expansion [83] is based on symmetries, and the galaxies in the presence of selection effects enjoy the same key symmetries as the Lyman alpha forest; the $SO(2)$ rotations around the line of sight and the equivalence principle.

Chen *et al.* [59] pursued an alternative route and built a perturbative expansion for the Lyman alpha forest flux $F$ starting from the exponential map of the effective optical depth field $\tau$, $F = \exp(-\tau)$. This field is often assumed to be a selection-independent tracer of dark matter, whose density is conserved during transformations from real to redshift space, see e.g. [79,80]. Chen *et al.* then showed how the combination of dynamics and the exponential map produces terms in the anisotropic bias expansion for the Lyman alpha forest derived in [83]. In this regard, the main theoretical goal of this work is to establish a direct connection between the two approaches. We will explicitly show that the combination of the exponential map and the EFT renormalizability principle explicitly reproduces the complete set of EFT operators. In order to emphasize the role of renormalization, we also carry out an alternative derivation in which we ignore counterterms, i.e. treat the perturbative expansion *à la* standard perturbation theory (SPT) [88]. In that case the exponential map produces an incomplete set of line-of-sight dependent bias operators at the tree level, with strong constraints on their bias coefficients. We call this naive SPT-like expansion "the tree-level Tau model." We show explicitly that this model is mathematically inconsistent. Once the model is properly renormalized, its tree-level constraints get violated by loops. We argue that within this particular derivation the loops should also generate the rest of the EFT operators allowed by symmetries. Our calculations thus suggest that the "renormalized" SPT-like approach is equivalent to the full EFT[4] once the loop corrections are taken into account.

It is also important to note that Refs. [53,89,90] found that the optical depth is actually a selection-dependent

tracer, i.e. in contrast to idealized galaxies[5] its fluctuations trace the line-of-sight velocity gradients. This further strengthens the motivation for a bottom-up approach such as the EFT.

On a more practical side, we extend a fast logarithmic Fourier transform (FFTLog) algorithm of Refs. [93,94] to quickly compute the full EFT one-loop power spectrum of the 3D Lyman alpha forest. Having done this calculation, we compare our EFT power spectrum model to the Lyman alpha forest data from the Sherwood simulations [52]. We find this model to be subpercent level accurate up to $k_{\max} = 3 \, h \, \mathrm{Mpc}^{-1}$ for $z = 2.8$, and up to $k_{\max} = 5 \, h \, \mathrm{Mpc}^{-1}$ for $z = 3.2$. We have also detected strong deviations from the predictions of the tree-level Tau model. This may be considered an "experimental" evidence in favor of the full EFT expansion and validity of the renormalization program. Finally, we show how the EFT approach works out at the level of the one-dimensional flux power spectrum. The methods that we have presented are ready to be applied to data. This paves the way for systematic and efficient EFT-based cosmological analyses of the Lyman alpha forest.

Our paper is structured as follows. In Sec. II we recap the Lyman alpha forest physics and discuss its aspects relevant for the EFT; scales and power counting. Section III outlines the EFT model first derived by [83] and discusses its features relevant for the Lyman alpha. There we also discuss the FFTLog implementation of our one-loop calculation. Section IV establishes the relationship between the EFT model and the exponential map. There we also introduce the tree-level Tau model, which we use as a case study to underline the importance of loop corrections and renormalization. In Sec. V we compare the full one-loop EFT model with Sherwood simulations. Section VI is devoted to the one-dimensional flux power spectrum modeling. Finally, we outline our main results and draw conclusions in Sec. VII. Some technical material is collected in Appendixes.

## II. PRELIMINARIES

### A. Basics of Lyman alpha forest

Our Universe is filled with optically thin neutral hydrogen (HI) clouds at redshifts $2 \lesssim z \lesssim 5$. Background quasars emit UV radiation that propagates towards us through these clouds along given lines of sight. The atoms in the cloud absorb the background radiation if the radiation's rest-frame frequency happens to match that of a transition between hydrogen levels. Notably, if the relevant wavelength is 121.6 nm, a hydrogen atom undergoes a Lyman alpha transition. Since the quasar spectrum is continuous in

---

[4]At least at the level of the one-loop power spectrum.

[5]From now on when discussing galaxies, we will always assume an idealized situation when the line-of-sight selection effects [86,87] are negligible, although this assumption may not always be warranted, see e.g. [91,92].

a wide frequency range, and there are many clouds along the line of sight at different redshifts, the observed quasar spectrum features a dense "comb" of absorption lines, called the Lyman alpha forest. The fraction of transmitted flux for each quasar spectrum is not homogeneous, and its fluctuations trace cosmological mass fluctuations along the line of sight. Specifically, under the assumption of photoionization-recombination equilibrium, the optical depth of neutral hydrogen clouds is proportional the Lyman alpha absorption cross section and the neutral hydrogen density $n_{HI}$ along the line of sight. The latter scales with the fractional overdensity of gas (baryons) $\delta_b$, gas temperature $T$, and the ionizing background amplitude $J$ as

$$n_{HI} \propto \frac{(1+\delta_b)^2}{T^{0.7} J}. \qquad (2.1)$$

Assumptions of the adiabatic expansion and the photoionization equilibrium lead to the tight relation between temperature and density, $T = T_0 (1+\delta_b)^{\gamma-1}$, where $\gamma \simeq 1.6$. Assuming that $T_0$, $J$ and $\gamma$ are constants (i.e. do not have spatial fluctuations), we arrive at the well-known conclusion (see e.g. [35,95,96]) that the fluctuations of $n_{HI}$ observed through the forest trace the underlying fluctuations of gas density, which in turn, must reflect the matter over-density $\delta$.[6] In this simplified model, known as the fluctuating Gunn-Peterson approximation [4,99], the optical depth $\tau$ is proportional to $n_{HI}$, while the transmitted flux we measure is simply given by $F = \exp(-\tau)$.

One way to study the Lyman alpha fluctuations is to model the optical depth field. In our work, however, we employ a different approach. Since we are interested in fluctuations of the flux, we focus directly on this observable. Instead of modeling explicitly underlying physics that affects the flux, we will build a perturbative (gradient) expansion that is based on symmetries of the problem and a minimal set of additional assumptions. In particular, we will not explicitly employ relations such as Eq. (2.1), but simply assume that the large-scale flux contrast is a certain unknown function of only a few variables (degrees of freedom); the tidal field, velocity gradients, and stochastic noise. This function is then represented as a general Taylor expansion that contains all possible dependencies allowed by symmetries. This approach in general is known as the EFT of large-scale structure [81,82,84,85].

In the EFT of large-scale structure one builds a perturbative expansion of relevant observables in terms of the matter over field, which is linear on large scales. This linear field $\delta^{(1)}$ is the seed function of all perturbative EFT calculations. Its statistical properties are fully fixed in terms of the linear matter power spectrum,

$$\langle \delta^{(1)}(\mathbf{k}) \delta^{(1)}(\mathbf{k}') \rangle = (2\pi)^3 \delta_D^{(3)}(\mathbf{k} + \mathbf{k}') P_{lin}(k, z). \qquad (2.2)$$

In what follows we will often drop the explicit redshift dependence and assume that all quantities are evaluated at a given redshift of the Lyman alpha forest, which we take to be $z = 2.8$ to match the simulation data that we use here. This redshift is similar to the redshifts of Lyman alpha forest data from BOSS [15], eBOSS [100], and DESI [47].

### B. Relevant scales

The EFT is a gradient expansion based on the assumption of scale separation. Let us discuss how well this assumption is satisfied by the Lyman alpha forest fluctuations.

The first relevant scale in the Lyman alpha forest physics is the nonlinear scale where the density field becomes fully nonlinear. In momentum space, it can be estimated as a wave number for which the amplitude of the dimensionless linear matter power spectrum becomes unity,

$$\frac{k_{NL}^3}{2\pi^2} P_{lin}(k_{NL}, z) = 1, \quad \Rightarrow \quad k_{NL} \simeq 5 \, h \, \text{Mpc}^{-1}, \quad \text{for } z \simeq 3. \qquad (2.3)$$

A perturbative description of the Lyman alpha forest is possible only if $k \ll k_{NL}$. The second relevant parameter is the smoothing scale. The forest is smoothed by two effects[7]; gas pressure (3D effect) [101] and thermal broadening (1D effect) [8,102,103]. These smoothing effects are naturally incorporated within the EFT as part of the gradient expansion. The gas perturbations are smoothed by pressure on the Jeans scale $k_J \sim 18 \, h \, \text{Mpc}^{-1}$ [19,101]. The absorption lines are also subject to thermal broadening, whose characteristic scale $k_S \sim 11 \, h \, \text{Mpc}^{-1}$ in the 1D flux power spectrum is comparable to that of the Jeans smoothing [19].[8] Both smoothing length scales are typically shorter than the nonlinear scale at the lower end of redshifts relevant for the forest, $z \simeq 3$. This gives us the following hierarchy of scales in the EFT for Lyman alpha:

$$k \ll k_{NL} \lesssim k_J, \quad k_s. \qquad (2.4)$$

High redshift Lyman alpha forest is affected by potentially significant spatial fluctuations of the ionizing background, and temperature fluctuations due to inhomogeneous (patchy) reionization.[9] The first effect modulates

---

[6]Recall that in standard linear cosmological perturbation theory $\delta_b = \delta$ sufficiently deep into the matter domination regime. Note that this condition is not always correct beyond $\Lambda$CDM, see e.g. [97,98].

[7]It is worth mentioning that the actual data features certain observational effects that effectively act as an additional source of smoothing, e.g. an imperfect resolution [17]. These effects can also be absorbed, to some extent, into the EFT expansion.

[8]We stress that both scales are not known exactly. The values quoted in [19] are benchmark values that are sufficient for our order-of-magnitude estimates.

[9]In our notation this can be thought of a spatial variation of $T_0$ in Eq. (2.1).

the power spectrum shape on a broad range of scales, up to $100\ h^{-1}$ Mpc [104,105]. These modulations are, however, quite smooth, which suggest that they can be captured perturbatively with an appropriately modified bias expansion. As far as the patchy reionization is concerned, Ref. [106] suggests that the gas temperature fluctuates on a scale of $\sim 25\ h^{-1}$ Mpc at $z \sim 5$. These results are consistent with simulations of Ref. [107], which additionally imply that patchy reionization may impact the 3D Lyman alpha power spectrum on wave number as large as $0.2\ h\,\mathrm{Mpc}^{-1}$ at a few percent level at low redshifts. This suggests that the typical scales associated with UV background and temperature fluctuations are significantly longer than the nonlinear scale, and hence their systematic description within a gradient expansion approach, such as EFT, may present a theoretical challenge.[10] In this work we build the EFT for Lyman alpha forest starting with an idealized scenario where the photoionization and temperature fluctuations are absent. We stress though that our description is still realistic at low redshifts ($z \sim 3$) and small scales ($k \gtrsim 0.1\ h\,\mathrm{Mpc}^{-1}$), where the effects in question are suppressed [105,107].

Within our approximation, the most relevant scale for the EFT expansion is the nonlinear scale, just like in the usual EFT of LSS. In what follows we will construct a perturbative expansion of the Lyman alpha forest fluctuations around linear theory, which will be implicitly controlled by a small parameter $k/k_{\mathrm{NL}}$. Let us sketch the structure of this expansion.

### C. Estimates of perturbative terms in the scaling Universe

Let us estimate the size of various terms in perturbation theory. It is convenient to approximate the actual $\Lambda$CDM power spectrum with a power-law $P_{\mathrm{lin}} \propto k^n$. For the range of scales relevant for our analysis, and for $z \approx 3$,
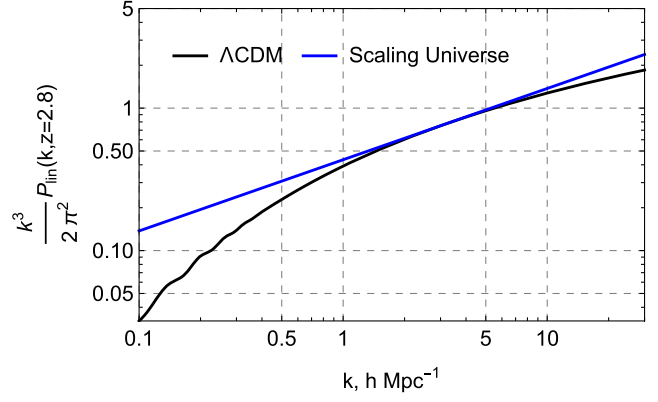


FIG. 1. The dimensionless linear matter power spectrum in $\Lambda$CDM and a scaling Universe from Eq. (2.5). Here we assume $z = 2.8$, a redshift of the Sherwood simulation snapshot that we use in this work.

$k \approx 3\ h\,\mathrm{Mpc}^{-1}$, the linear matter power spectrum can be well-approximated as

$$P_{\mathrm{lin}}(k) = 2\pi^2 \frac{k^n}{k_{\mathrm{NL}}^{n+3}}, \quad \text{with} \quad n \approx -2.5, \quad k_{\mathrm{NL}} \approx 5.3\ h\,\mathrm{Mpc}^{-1},$$

(2.5)

see Fig. 1, where the scaling Universe curve is normalized to the linear power spectrum at $k = 3\ h\,\mathrm{Mpc}^{-1}$. From the dimensional analysis, the $L$th-loop correction to this power spectrum must scale as [88,109]

$$\frac{k^3}{2\pi^2} P_{L-\mathrm{loop}}(k) = \frac{\alpha_L (2\pi^2)}{k_{\mathrm{NL}}^3} \left( \frac{k}{k_{\mathrm{NL}}} \right)^{(n+3)(L+1)}, \quad (2.6)$$

where $\alpha_L$ is an order one number. These terms will be refereed to as "mode-coupling corrections" in what follows. The higher-derivative (counterterm) corrections scale as $k^2 P_{\mathrm{lin}} \propto k^{n+2}$. Thus, the total power spectrum in the EFT reads, schematically

$$P_{\mathrm{NL}}(k) = 2\pi^2 \frac{k^n}{k_{\mathrm{NL}}^{n+3}} \left( \underbrace{1}_{\text{linear}} + \underbrace{\alpha_1 \left( \frac{k}{k_{\mathrm{NL}}} \right)^{n+3}}_{1-\text{loop}} + \underbrace{\alpha_2 \left( \frac{k}{k_{\mathrm{NL}}} \right)^{2(n+3)}}_{2-\text{loop}} + \underbrace{\alpha_{k^2} \left( \frac{k}{k_{\mathrm{NL}}} \right)^2}_{\text{higher deriv}} + \cdots \right)$$

$$= 2\pi^2 \frac{k^{-2.5}}{k_{\mathrm{NL}}^{0.5}} \left( \underbrace{1}_{\text{linear}} + \underbrace{\alpha_1 \left( \frac{k}{k_{\mathrm{NL}}} \right)^{0.5}}_{1-\text{loop}} + \underbrace{\alpha_2 \left( \frac{k}{k_{\mathrm{NL}}} \right)^{1}}_{2-\text{loop}} + \underbrace{\alpha_{k^2} \left( \frac{k}{k_{\mathrm{NL}}} \right)^2}_{\text{higher deriv}} + \cdots \right), \quad (2.7)$$

where we used $n = -2.5$ from Eq. (2.5) in the second line. Note that we explicitly included only the mode coupling and $k^2$ corrections above. We see that in our toy model scaling Universe the one-loop corrections due to mode coupling are the leading contributions in the regime $k \ll k_{\mathrm{NL}}$. The $k^2$ corrections become important only at the three-loop order.[11]

---

[10]See however Ref. [108] for an approach to resumm the large gradients due to the radiation transfer effects.

[11]See [110,111] for the three-loop order matter calculations.

Our discussion so far has considered nonlinearity in the context of the matter density field. In the EFT, additional nonlinearities appear due to biasing and redshift-space distortions. These effects are conceptually similar to the dark matter nonlinearities, and hence our scaling Universe estimates are expected to apply to the more realistic case without significant modifications.[12] One aspect worth mentioning is the presence of constant stochastic shot noise contribution, which is, however, negligibly small in the scaling Universe where it scales as $P_{\text{shot}} \sim k_{\text{NL}}^{-3}$.

From Eq. (2.7) we see that in contrast to galaxies (see e.g. [114,115]), the leading order corrections to linear theory in the Lyman alpha forest case come from the one-loop mode coupling effects.[13] Recall that for the scales relevant to galaxy clustering the effective power law is less steep, $n \approx -1.5$, so that the $k^2$-type higher-derivative terms become important already at the one-loop level. Our $\Lambda$CDM Universe is, of course, more complicated than the toy model we consider here. Nevertheless, the scaling Universe model gives us a good sense of the importance of various terms in the perturbation expansion.

## III. EFFECTIVE FIELD THEORY FOR LYMAN ALPHA FLUCTUATIONS

### A. Overview of galaxies in redshift space

It is instructive to start our discussion of the bias model for the Lyman alpha with a recap of the bias model for galaxies. In real space, and on large scales, the galaxy overdensity field $\delta_g$ can be expressed through a perturbative expansion over the velocity gradients and tidal fields [83,116–119]. This expansion is, in general, nonlocal in time, but at the cubic in density order, relevant for the one-loop power spectrum calculation, it can be expressed through local in time operators [83]. Specifically, at this order, we have the following expression for the deterministic part of the galaxy bias relation,

$$\delta_g(\mathbf{x}) = b_1^g \delta(\mathbf{x}) + \frac{b_2^g}{2}(\delta(\mathbf{x})^2 - \langle \delta(\mathbf{x})^2 \rangle) + b_{\mathcal{G}_2}^g \mathcal{G}_2(\mathbf{x})$$
$$+ b_{\Gamma_3}^g \Gamma_3(\mathbf{x}) + b_{\nabla^2 \delta}^g R_*^2 \nabla^2 \delta, \qquad (3.1)$$

where $\delta$ is the (nonlinear) matter overdensity field, and we also defined

$$\mathcal{G}_2(\mathbf{x}) = (\partial_i \partial_j \Phi)^2 - (\partial^2 \Phi)^2,$$
$$\Gamma_3(\mathbf{x}) = \mathcal{G}_2[\Phi] - \mathcal{G}_2[\Phi_v], \qquad (3.2)$$

where we introduced velocity and density potentials $\Phi$ and $\Phi_v$, respectively, which satisfy

$$\partial^2 \Phi = \delta, \qquad \partial_i \Phi_v = v^i, \qquad (3.3)$$

where $v^i$ is the peculiar velocity field. The bias coefficients $b_1^g, b_2^g, b_{\mathcal{G}_2}^g, b_{\Gamma_3}^g, b_{\nabla^2 \delta}^g$ are free parameters that characterize a given galaxy selection; $R_*$ is the typical length scale associated with galaxies, which we inserted to make $b_{\nabla^2 \delta}^g$ dimensionless. Typically, this scale is assumed to be of the order of the Lagrangian radius of the host halos [83,120], but it can be as large as $100\,h\,\text{Mpc}^{-1}$ if the radiation transfer effects are included, see e.g. [108,121].

There are several aspects of the galaxy bias model in Eq. (3.1) that are worth emphasizing. It is the most general local in time perturbative expansion in the matter density in real space, modulo terms that do not contribute at the level of the one-loop galaxy power spectrum, e.g. $\delta^3$. This expansion involves all possible operators allowed by symmetries of the problem, the spherical symmetry and the equivalence principle. In our context this means the relevant operators are scalars under $SO(3)$ rotations, and there is no velocity bias on large scales, i.e. galaxies undergo the same acceleration as dark matter. Using the general symmetry-motivated expansions like (3.1) is the key principle of effective field theory. In this philosophy, the distribution of galaxies on large scales is expressed in terms of underlying basic long-wavelength degrees of freedom, which in our context are matter density, velocity gradients, and tidal fields, plus stochastic terms that will be discussed later. The tree-level bias coefficients that appear in (3.1) are, strictly speaking, not well-defined since they receive formally infinite-loop corrections. In the EFT jargon these are called "bare" parameters, or Wilson coefficients. Only their finite "renormalized" parts make physical sense and can be matched to the data that describes physical observables.

Since the galaxies are observed in redshift space, one needs to transform the galaxy bias expansion (3.1) using the following velocity-dependent mapping (see e.g. [88]),[14]

$$\delta_g^{(s)}(\mathbf{k}) = \delta_g(\mathbf{k}) + \int d^3x\, e^{-i\mathbf{k}\mathbf{x}}\left(e^{-ik_z v_{gz}(\mathbf{x})/(aH)} - 1\right)$$
$$\times (1 + \delta_g(\mathbf{x})), \qquad (3.4)$$

---

[12]It is important to note that the velocity field is more nonlinear than the density one, see e.g. [112,113], i.e. the wave number associated with the velocity nonlinear scale is smaller.

[13]Here we distinguish between the one-loop mode-coupling integrals and higher-derivative counterterms, both of which are parts of the one-loop power spectrum.

[14]Using this expansion, we assume a flat-sky approximation that is accurate for small scales relevant for our work.

where we have switched to the Fourier-space representation, and used $a$ and $H$ to denote the metric scale factor and the Hubble parameter, respectively, $\mathcal{H} = aH$ is the conformal Hubble parameter, whilst the subscript $z$ stands for the projection onto the line of sight, which we will describe with the unit vector $\hat{\mathbf{z}}$. $v_g$ above is the tracer's velocity, which is equal to the matter peculiar velocity $v$ at the zeroth order in the derivative expansion due to the equivalence principle.

In what follows it will be convenient to use the following notation for the normalized velocity gradient of matter along the line of sight,

$$\eta \equiv \frac{\partial_z v_z}{aH}. \tag{3.5}$$

Note that in linear theory in Fourier space we have

$$\eta \approx -f\mu^2 \delta_{\mathbf{k}}^{(1)}, \qquad \mu = \frac{(\hat{\mathbf{z}} \cdot \mathbf{k})}{k}, \tag{3.6}$$

where we introduced $f \equiv d\ln D_+/d\ln a$ ($D_+$ is the growth factor).

Assuming that the velocity field is perturbative, one Taylor expands the exponent in (3.4) and finds, at linear order,

$$\delta_g^{(s)} = b_1^g \delta - \eta. \tag{3.7}$$

Crucially, the second term, which depends on the line of sight, does not have any free parameter in front of it. This embodies the absence of selection effects, and follows from the conservation of the galaxy number density under the coordinate transformation from the galaxy rest frame to observed redshift space.

Going to higher order in the Taylor expansion of (3.4), one obtains corrections to the observed galaxy overdensity due to redshift-space distortions (RSD). Note that this expansion generates extra UV sensitivity, which must be removed by appropriate counterterms [122,123], which start at order $k^2\delta$. Apart from these higher-derivative contributions, RSD mapping (3.4) does not generate new free parameters for the deterministic part of the galaxy power spectrum in redshift space. The redshift space galaxy overdensity reads[15]

$$\delta_g^{(s)}(\mathbf{k}) = Z_1(\mathbf{k})\delta_{\mathbf{k}}^{(1)} + \int_{\mathbf{q}_1}\int_{\mathbf{q}_2}(2\pi)^3\delta_D(\mathbf{k}-\mathbf{q}_{12})Z_2(\mathbf{q}_1,\mathbf{q}_2)\delta_{\mathbf{q}_1}^{(1)}\delta_{\mathbf{q}_2}^{(1)}$$
$$+ \int_{\mathbf{q}_1}\int_{\mathbf{q}_2}\int_{\mathbf{q}_3}(2\pi)^3\delta_D(\mathbf{k}-\mathbf{q}_{123})Z_3(\mathbf{q}_1,\mathbf{q}_2,\mathbf{q}_3)\delta_{\mathbf{q}_1}^{(1)}\delta_{\mathbf{q}_2}^{(1)}\delta_{\mathbf{q}_3}^{(1)} + \cdots, \tag{3.8}$$

where the dots denote higher-loop corrections and higher-derivative counterterms, $\delta_{\mathbf{k}}^{(1)}$ is the linear matter density field, while the redshift-space kernels $Z_{1,2,3}$ are given by

$$Z_1(\mathbf{k}) = b_1^g + f\mu^2, \tag{3.9a}$$

$$Z_2(\mathbf{k}_1,\mathbf{k}_2) = \frac{b_2^g}{2} + b_{\mathcal{G}_2}^g\left(\frac{(\mathbf{k}_1\cdot\mathbf{k}_2)^2}{k_1^2 k_2^2} - 1\right) + b_1^g F_2(\mathbf{k}_1,\mathbf{k}_2) + f\mu^2 G_2(\mathbf{k}_1,\mathbf{k}_2)$$
$$+ \frac{f\mu k}{2}\left(\frac{\mu_1}{k_1}(b_1^g + f\mu_2^2) + \frac{\mu_2}{k_2}(b_1^g + f\mu_1^2)\right), \tag{3.9b}$$

$$Z_3(\mathbf{k}_1,\mathbf{k}_2,\mathbf{k}_3) = 2b_{\Gamma_3}^g\left[\frac{(\mathbf{k}_1\cdot(\mathbf{k}_2+\mathbf{k}_3))^2}{k_1^2(\mathbf{k}_2+\mathbf{k}_3)^2} - 1\right][F_2(\mathbf{k}_2,\mathbf{k}_3) - G_2(\mathbf{k}_2,\mathbf{k}_3)]$$
$$+ b_1^g F_3(\mathbf{k}_1,\mathbf{k}_2,\mathbf{k}_3) + f\mu^2 G_3(\mathbf{k}_1,\mathbf{k}_2,\mathbf{k}_3) + \frac{(f\mu k)^2}{2}(b_1^g + f\mu_1^2)\frac{\mu_2}{k_2}\frac{\mu_3}{k_3}$$
$$+ f\mu k\frac{\mu_3}{k_3}[b_1^g F_2(\mathbf{k}_1,\mathbf{k}_2) + f\mu_{12}^2 G_2(\mathbf{k}_1,\mathbf{k}_2)] + f\mu k(b_1^g + f\mu_1^2)\frac{\mu_{23}}{k_{23}}G_2(\mathbf{k}_2,\mathbf{k}_3)$$
$$+ b_2^g F_2(\mathbf{k}_1,\mathbf{k}_2) + 2b_{\mathcal{G}_2}\left[\frac{(\mathbf{k}_1\cdot(\mathbf{k}_2+\mathbf{k}_3))^2}{k_1^2(\mathbf{k}_2+\mathbf{k}_3)^2} - 1\right]F_2(\mathbf{k}_2,\mathbf{k}_3) + \frac{b_2^g f\mu k}{2}\frac{\mu_1}{k_1}$$
$$+ b_{\mathcal{G}_2}^g f\mu k\frac{\mu_1}{k_1}\left[\frac{(\mathbf{k}_2\cdot\mathbf{k}_3)^2}{k_2^2 k_3^2} - 1\right], \tag{3.9c}$$

---

[15]We use the notation $\int_{\mathbf{q}} \equiv \int \frac{d^3q}{(2\pi)^3}$.

where the density and velocity SPT kernels $F_n$ and $G_n$ can be found, e.g. in [88]. Note that $Z_3$ must be symmetrized over its arguments. We also introduced cosines between the line of sight and momentum vectors,

$$\mu_i \equiv \frac{(\hat{\mathbf{z}} \cdot \mathbf{k}_i)}{k_i}, \qquad (3.10)$$

and use $\mathbf{k}$ to denote the sum of all arguments, i.e. for $Z_3$ we have $\mathbf{k} \equiv \mathbf{k}_1 + \mathbf{k}_2 + \mathbf{k}_3$.

Note that the density field variance $\langle \delta(\mathbf{x})^2 \rangle$ is used in the Eq. (3.1) in order to enforce the vanishing of the over-density vacuum expectation value, $\langle \delta \rangle = 0$, which a properly defined fluctuating field must satisfy. The $\mathbf{k} = 0$ correction to (3.9) produced by the density variance is not explicitly shown above, but it is needed to ensure that the line-of-sight dependent bias operators are not generated by loop corrections for galaxies.

## B. General bias expansion for the Lyman alpha forest

The Lyman alpha forest is different from galaxies in several important aspects. First, unlike galaxies, the forest has a preferred direction—the line of sight. Indeed, in contrast to galaxies, the flux fluctuations intrinsically exist only in redshift space. This means that new operators are allowed in the Lyman alpha forest bias expansion. Physically, this happens because the absorption probability for the Lyman-$\alpha$ line depends on the tidal field along the line of sight. Mathematically, this property may traced to the nonlinear mapping between flux and the optical depth, $F = \exp(-\tau)$. If one assumes that the $\tau$ field is a matter tracer whose number density is conserved, just like for galaxies, there would be no selection effects, and the bias expansion would take the form (3.7) at the lowest order. The nonlinear mapping, however, breaks the conservation of tracer number density [79] and forces us to introduce line of sight selection effects. At linear order, and in the rest frame of a neutral hydrogen cloud, we should write

$$\frac{F - \bar{F}}{\bar{F}} \equiv \delta_F = b_1 \delta + b_\eta \hat{z}^i \hat{z}^j \partial_i \partial_j \Phi, \qquad (3.11)$$

where $\bar{F} \equiv \langle F \rangle$ is the mean transmitted flux. In linear theory the tidal field is related to the velocity gradient $\eta$ defined in Eq. (3.5), so that one can rewrite the above expression as

$$\delta_F = b_1 \delta + b_\eta \eta, \qquad (3.12)$$

The new selection-dependent parameter $b_\eta$ will be referred to as "velocity gradient bias" in what follows [80]. The linear model (3.12) produces the well-known tree-level result

$$P_{\text{tree}}(k, \mu) = (b_1 - b_\eta f \mu^2)^2 P_{\text{lin}}(k), \qquad (3.13)$$

which is a simple generalization of the Kaiser formula for galaxies [124]. We stress that Eq. (3.11) is not the most general expression. As in the context of galaxies, a consistent

bias expansion should depend on the history of the relevant operators along their fluid trajectories $\mathbf{x}_{\text{fl}}(\mathbf{x}, \tau)$ ($\mathbf{x}$ is the last point of the trajectory) [83,85,116,118,125],[16]

$$\delta_F(\mathbf{x}, \tau) \supset \int^\tau T(\tau, \tau') \mathcal{O}(\tau', \mathbf{x}_{\text{fl}}(\mathbf{x}, \tau')), \qquad (3.14)$$

where $\tau$ is conformal time. Using the matter equations of motion, the dependence on the fluid trajectory and time can be Taylor expanded and summed up into a finite number of linearly independent terms, which eventually reproduce the *local-in-time* bias expansion similar to Eq. (3.12). All in all, it is important to keep in mind that the bias expansion is intrinsically nonlocal in time, but for the purposes of the one-loop power spectrum calculation this nonlocality is irrelevant, so we will proceed with the local in time expansion.

It is straightforward to generalize the bias model (3.12) to operators that are higher order in the linear density field. Specifically, Ref. [86] showed that a general selection-dependent biased tracer has the following deterministic bias model up to cubic order:

$$\delta_F = b_1 \delta + \frac{b_2}{2} \delta^2 + b_{\mathcal{G}_2} \mathcal{G}_2 + b_{\Gamma_3} \Gamma_3 + b_\eta \eta$$
$$+ b_{(KK)_\parallel} K_{ij} K_{jl} \hat{z}^i \hat{z}^l + b_{\delta\eta} \eta\delta + b_{\eta^2} \eta^2 + b_{\Pi_\parallel^{[2]}} \Pi_{ij}^{[2]} \hat{z}^i \hat{z}^j$$
$$+ b_{\delta\Pi_\parallel^{[2]}} \delta\Pi_{ij}^{[2]} \hat{z}^i \hat{z}^j + b_{\eta\Pi_\parallel^{[2]}} \eta\Pi_{ij}^{[2]} \hat{z}^i \hat{z}^j + b_{(K\Pi^{[2]})_\parallel} K_{ij} \Pi_{jl}^{[2]} \hat{z}^i \hat{z}^l$$
$$+ b_{\Pi_\parallel^{[3]}} \Pi_{ij}^{[3]} \hat{z}^i \hat{z}^j, \qquad (3.15)$$

where we kept only the terms that contribute nontrivially to the one-loop power spectrum, and introduced the new operators

$$K_{ij} = \frac{\partial_i \partial_j \delta}{\Delta} - \frac{1}{3} \delta_{ij} \delta$$
$$\Pi_{ij}^{[1]} = \partial_i \partial_j \Phi = \frac{\partial_i \partial_j \delta}{\Delta},$$
$$\Pi_{ij}^{[n]} = \frac{1}{(n-1)!} \left[ (aHf)^{-1} \frac{D}{D\tau} \Pi_{ij}^{[n-1]} - \Pi_{ij}^{[n-1]} \right], \quad n > 1,$$
$$(3.16)$$

where we used the convective derivative $\frac{D}{D\tau} = \partial_\tau + v^i \partial_i$. The explicit expressions for the tensors $\Pi_{ij}^{[2]}$ and $\Pi_{ij}^{[3]}$ in perturbation theory can be found in Ref. [86]. In total, we have nine new selection-bias coefficients in addition to the four selection-free ones.[17]

---

[16]In analogy with the smoothing scale of the Lyman alpha fluctuations [101], one may say that the Lyman alpha bias parameters in general are expected to depend on the whole reionization history of the Universe.

[17]Our discussion so far does not include higher-derivative counterterms and stochastic-bias contributions, which will generate additional free parameters.

The expression (3.15) is written in the rest-frame of the tracer. In order to describe the actual observations, this has to be transferred to the observer's frame using the standard RSD mapping (3.4) [83,86]. Note that the physical meaning of the RSD mapping here is somewhat different from that in the galaxies' case. Neglecting selection effects, the mapping simply acts on the real-space bias expansion that captures the actual number density in tracer's rest frame. If the probability to detect a galaxy depends on line-of-sight properties [87,92], the line-of-sight selection effects should be treated as part of the bias expansion that describes the *apparent* number density of the tracer in its rest frame. The apparent density can be defined as the observed galaxy distribution formally inversely transformed from redshift space to real space. Obviously, it is different from the *actual*, rest-frame (real-space) galaxy number density, which, in principle, can be reconstructed with better selection criteria or better measurements [87]. Contrasting the actual number density and the observed one in redshift space, we may say that the RSD mapping does not conserve the galaxy number density in the presence of selection effects. In the Lyman alpha case, the line-of-sight

dependent bias expansion also captures the apparent number density. This number density is by definition subject to the RSD mapping that conserves it. The conceptual difference with galaxies is that the Lyman alpha fluctuations intrinsically live along lines of sight, so that a notion of the actual rest-frame density does not make sense in this case. From the technical point of view, however, the treatment of the mapping is similar: on has to apply the RSD mapping (3.4) to the selection-dependent bias expansion (3.15).

When expanded, the RSD mapping will produce additional velocity-dependent contributions into (3.15), most of which will be degenerate with the selection terms that are already present. This will lead to an unobservable redefinition of the selection bias coefficients. There will be, however, a few extra operators that are not present in (3.15). These terms correspond to pure projection effects, i.e. they explicitly depend on locally unobservable tracer's velocity. The coefficients in front of these terms are protected by the equivalence principle and do not get renormalized by nonlinear effects. With these terms included, we have the net expression [86]:

$$\delta_F^{(s)} = \delta_F + \frac{v_z}{aH}\hat{z}^i\partial_i[b_1\delta + b_\eta\eta + b_{\Pi_\parallel^{[2]}}\Pi_{kl}^{[2]}\hat{z}^k\hat{z}^l]. \tag{3.17}$$

The final mode-coupling three-dimensional one-loop power spectrum that comes from the expansion (3.17) is given by

$$\Delta P^{1-\text{loop}}(k,\mu) \equiv 2\int_{\mathbf{q}} K_2^2(\mathbf{q},\mathbf{k}-\mathbf{q})P_{\text{lin}}(|\mathbf{k}-\mathbf{q}|)P_{\text{lin}}(q)$$
$$+ 6K_1(\mathbf{k})P_{\text{lin}}(k)\int_{\mathbf{q}} K_3(\mathbf{k},-\mathbf{q},\mathbf{q})P_{\text{lin}}(q), \tag{3.18}$$

where we introduced the new selection-dependent redshift space kernels,

$$K_1(\mathbf{k}) = b_1 - b_\eta f\mu^2,$$

$$K_2(\mathbf{k}_1,\mathbf{k}_2) = \frac{b_2}{2} + b_{\mathcal{G}_2}\left(\frac{(\mathbf{k}_1\cdot\mathbf{k}_2)^2}{k_1^2 k_2^2} - 1\right) + b_1 F_2(\mathbf{k}_1,\mathbf{k}_2) - b_\eta f\mu^2 G_2(\mathbf{k}_1,\mathbf{k}_2)$$

$$- fb_{\delta\eta}\frac{\mu_2^2 + \mu_1^2}{2} + b_{\eta^2}f^2\mu_1^2\mu_2^2 + b_1 f\frac{\mu_1\mu_2}{2}\left(\frac{k_2}{k_1} + \frac{k_1}{k_2}\right) - b_\eta f^2\frac{\mu_1\mu_2}{2}\left(\frac{k_2}{k_1}\mu_2^2 + \frac{k_1}{k_2}\mu_1^2\right)$$

$$+ b_{(KK)_\parallel}\left(\mu_1\mu_2\frac{(\mathbf{k}_1\cdot\mathbf{k}_2)}{k_1 k_2} - \frac{\mu_1^2 + \mu_2^2}{3} + \frac{1}{9}\right)$$

$$+ b_{\Pi_\parallel^{(2)}}\left(\mu_1\mu_2\frac{(\mathbf{k}_1\cdot\mathbf{k}_2)}{k_1 k_2} + \frac{5}{7}\mu^2\left(1 - \frac{(\mathbf{k}_1\cdot\mathbf{k}_2)^2}{k_1^2 k_2^2}\right)\right), \tag{3.19}$$

$$\int_{\mathbf{q}} K_3(\mathbf{k},\mathbf{q},-\mathbf{q})P_{\text{lin}}(q) = b_1\int_{\mathbf{q}} F_3(\mathbf{k},\mathbf{q},-\mathbf{q})P_{\text{lin}}(q) - fb_\eta\mu^2\int_{\mathbf{q}} G_3(\mathbf{q},-\mathbf{q},\mathbf{k})P_{\text{lin}}(q) + \int_{\mathbf{q}}[1 - (\hat{k}\cdot\hat{q})^2]P_{\text{lin}}(q)$$

$$\times\left\{\frac{4}{21}(5b_{\mathcal{G}_2} + 2b_{\Gamma_3})\left[\left(\frac{(\mathbf{k}-\mathbf{q})\cdot\mathbf{q}}{|\mathbf{k}-\mathbf{q}|q}\right)^2 - 1\right] - \frac{2}{21}fb_{\delta\eta}\left[\frac{3(k_\parallel - q_\parallel)^2}{|\mathbf{k}-\mathbf{q}|^2} + \frac{5q_\parallel^2}{q^2}\right]\right\}$$

$$+ \frac{4}{7} f^2 b_{\eta^2} \frac{q_\parallel^2}{q^2} \frac{(k_\parallel - q_\parallel)^2}{|\mathbf{k} - \mathbf{q}|^2} + \frac{20}{21} b_{(KK)_\parallel} \left[ \frac{(\mathbf{k} \cdot \mathbf{q} - q^2)(k_\parallel - q_\parallel) q_\parallel}{|\mathbf{k} - \mathbf{q}|^2 q^2} - \frac{1}{3} \frac{(k_\parallel - q_\parallel)^2}{|\mathbf{k} - \mathbf{q}|^2} - \frac{1}{3} \frac{q_\parallel^2}{q^2} + \frac{1}{9} \right]$$

$$+ \frac{10}{21} b_{\Pi_\parallel^{[2]}} \frac{(\mathbf{k} \cdot \mathbf{q} - q^2)}{|\mathbf{k} - \mathbf{q}|^2} \frac{(k_\parallel - q_\parallel)^2}{q^2} + \frac{10}{21} \left[ b_{\delta \Pi_\parallel^{[2]}} - \frac{1}{3} b_{(K\Pi^{[2]})_\parallel} - f b_{\eta \Pi_\parallel^{[2]}} \frac{q_\parallel^2}{q^2} \right] \frac{(k_\parallel - q_\parallel)^2}{|\mathbf{k} - \mathbf{q}|^2}$$

$$+ \frac{10}{21} b_{(K\Pi^{[2]})_\parallel} \frac{(\mathbf{q} \cdot \mathbf{k} - q^2)}{q|\mathbf{k} - \mathbf{q}|} \frac{q_\parallel (k_\parallel - q_\parallel)}{q|\mathbf{k} - \mathbf{q}|} + \frac{10}{21} f b_{\Pi_\parallel^{[2]}} \frac{q_\parallel (k_\parallel - q_\parallel)^3}{q^2 |\mathbf{k} - \mathbf{q}|^2}$$

$$+ (b_{\Pi_\parallel^{[3]}} + 2 b_{\Pi_\parallel^{[2]}}) \left[ \frac{13}{21} \frac{\mathbf{k} \cdot \mathbf{q} - q^2}{|\mathbf{k} - \mathbf{q}|^2} \frac{q_\parallel (k_\parallel - q_\parallel)}{q^2} - \frac{5 \mu^2}{9} \left[ \left( \frac{(\mathbf{k} - \mathbf{q}) \cdot \mathbf{q}}{|\mathbf{k} - \mathbf{q}| q} \right)^2 - \frac{1}{3} \right] \right]$$

$$+ \frac{2}{21} f b_1 \left[ 5 \frac{q_\parallel (k_\parallel - q_\parallel)}{q^2} + 3 \frac{q_\parallel (k_\parallel - q_\parallel)}{|\mathbf{k} - \mathbf{q}|^2} \right] - \frac{2}{7} f^2 b_\eta \frac{q_\parallel (k_\parallel - q_\parallel)}{q^2 |\mathbf{k} - \mathbf{q}|^2} [(k_\parallel - q_\parallel)^2 + q_\parallel^2] \Bigg\}. \quad (3.20)$$

Note that for convenience, we presented the $K_3$ integrand instead of the kernel, as in this case the expression greatly simplifies.

## C. Higher-derivative counterterms and stochastic contributions

The line-of-sight dependent higher-derivative and stochastic contributions relevant for the one-loop power spectrum of a generic selection-dependent tracer are also known [86],

$$\delta_F^{(s)}\big|_{\text{stoch+h.d.}} = \epsilon + b_{\nabla^2 \delta}^g R_*^2 \nabla^2 \delta + b_\eta R_*^2 \nabla^2 (\beta_{\nabla^2 \mathbf{v}} \nabla^2 \eta + \beta_{\partial_\parallel^2 \mathbf{v}} \nabla^2 \eta), \quad (3.21)$$

where $\epsilon$ is the stochastic field uncorrelated with $\delta$. Note that we do not explicitly add the redshift-space EFT counterterms $\sim k^2 \mu^{2n} \delta$ [122] in Eq. (3.21) as they are fully degenerate with the higher-derivative operators that we already have. On the one hand, our scaling Universe analysis suggests that the higher-derivative contributions scale as three-loop order contributions, and hence may be ignored at the one-loop order we are interested in. On the other hand, the precision of the Sherwood simulation data is sufficient to nominally detect these terms even when their Wilson coefficients are very small, of the order $10^{-3} [h^{-1} \text{Mpc}]^2$. The inclusion of these corrections noticeably improves the fit at $k \sim 3 \, h \, \text{Mpc}^{-1}$, which is why we prefer to keep them. The theoretical rationale behind this choice is that these corrections can be treated as a proxy for higher-loop contributions, which can be partially absorbed into the counterterms (3.21). Thus, their inclusion may indeed improve the fit even if two-loop and three-loop contributions are not explicitly included.

As far as the stochastic corrections are concerned, their expression up to $(k/k_{\text{NL}})^2$ order is given by [86,126]

$$\langle \epsilon(\mathbf{k}) \epsilon(\mathbf{k}') \rangle = (2\pi)^3 \delta_D^{(3)}(\mathbf{k} + \mathbf{k}') \times \left( P_{\text{shot}} + a_0 \frac{k^2}{k_{\text{NL}}^2} + a_2 \frac{k^2 \mu^2}{k_{\text{NL}}^2} \right), \quad (3.22)$$

where $P_{\text{shot}}$, $a_{0,2}$ are dimensionful stochastic counterterms. The shot noise corrections can be ignored for the 3D correlators, but are important for the 1D power spectrum, see Sec. VI for more detail.

## D. IR resummation

Baryon acoustic oscillations are affected by large IR effects, which may be resummed along the lines of Refs. [127–133]. These effects are fully controlled by the displacement and velocity fields, which are both locally unobservable. In the context of the Eulerian fluid description, the structure of these IR-sensitive terms is dictated by the equivalence principle, which demands that the IR-enhanced contributions cancel in the formal limit $\{q_i\} \to 0$, where $\{q_i\}$ denote a set of loop momenta. The cancellation is inexact if some $q_i$'s are greater than the BAO scale $r_{\text{BAO}} \sim 110 \, h \, \text{Mpc}^{-1}$. In that case (IR) resummation is needed. Since IR resummation is controlled by the IR-divergent terms whose form is completely fixed by the equivalence principle, it would be unaffected by the line-of-sight selection bias operators, which are finite in the IR limit by construction. This implies that IR resummation for a generic line-of-sight dependent tracer would be identical to that of redshift space galaxies [132], as was first pointed out in [86]. Indeed, one can explicitly check that the new line-of-sight dependent operators do not produce any new IR singularities in the soft limit, see e.g. (3.20).

Even though IR resummation can be straightforwardly included, we defer its explicit implementation for future work. First, the main goal of this paper is to study the performance of the EFT on small scales, $k \sim 3 \, h \, \text{Mpc}^{-1}$, where the BAO feature is completely washed out. Second,

the hydrodynamical simulations that we use here do not have enough large-scale resolution for a significant detection of the BAO in the data. Given these reasons, we believe that the nonlinear effects on the BAO deserve a separate dedicated analysis that goes beyond the scope of this paper.

### E. Calculation of loop integrals with FFTLog

The one-loop expression (3.18) can be transformed to the form suitable for the evaluation with the FFTLog method [93] (see also [134,135]). The basic idea of this method is to represent the linear matter power spectrum, which is an input in all loop calculations, as a sum of the power-law functions. Then the loop integrals for each power law can be done analytically, and a loop calculation reduces to a matrix multiplication problem.

In redshift space, following Ref. [94] (see also [136]), one has to expand the loop integrands over a basis of master operators involving contractions of the line of sight vector $\hat{\mathbf{z}}$ and loop momenta. One technical difficulty with respect to the case of galaxies is that one needs such master expression up to eight momenta instead of four in the galaxy case. This is quite straightforward albeit the expressions are rather lengthy. The eventual expressions for the relevant master integrals after taking all the necessary contractions of the basis operators are given by

$$\int_{\mathbf{q}} \frac{(\hat{\mathbf{z}} \cdot \mathbf{q})^5}{q^{2\nu_1} |\mathbf{q} - \mathbf{k}|^{2\nu_2}} = k^{3-2\nu_{12}} \cdot k^5 \mu (A_5 + \mu^2 B_5 + \mu^4 C_5),$$

$$\int_{\mathbf{q}} \frac{(\hat{\mathbf{z}} \cdot \mathbf{q})^6}{q^{2\nu_1} |\mathbf{q} - \mathbf{k}|^{2\nu_2}} = k^{3-2\nu_{12}} \cdot k^6 (A_6 + \mu^2 B_6 + \mu^4 C_6 + \mu^6 D_6),$$

$$\int_{\mathbf{q}} \frac{(\hat{\mathbf{z}} \cdot \mathbf{q})^7}{q^{2\nu_1} |\mathbf{q} - \mathbf{k}|^{2\nu_2}} = k^{3-2\nu_{12}} \cdot k^7 \mu (A_7 + \mu^2 B_7 + \mu^4 C_7 + \mu^6 D_7),$$

$$\int_{\mathbf{q}} \frac{(\hat{\mathbf{z}} \cdot \mathbf{q})^8}{q^{2\nu_1} |\mathbf{q} - \mathbf{k}|^{2\nu_2}} = k^{3-2\nu_{12}} \cdot k^8 (A_8 + \mu^2 B_8 + \mu^4 C_8$$
$$+ \mu^6 D_8 + \mu^8 E_8), \quad (3.23)$$

where $\nu_{12} \equiv \nu_1 + \nu_2$ and the master functions $A_n, B_n, C_n, D_n, E_n$ for $n = 5, 6, 7, 8$ are given in Appendix A. The rest of the master integrals are presented in Appendix A of [94]. With the help of master integrals like (3.23), the total mode-coupling power spectrum may be written as

$$\Delta P^{1-\text{loop}} = \sum_{n=0}^{4} \mu^{2n} P_n^{(22)} + (b_1 - b_\eta f \mu^2) \sum_{n=0}^{2} \mu^{2n} P_n^{(13)},$$
$$(3.24)$$

where $P_n^{(22)}$ and $P_n^{(13)}$ depend on the biases that appear in Eq. (3.17).

An important aspect of the FFTLog method is the choice of the so-called FFTLog bias parameter $\nu$ which appears in the FFTLog power law approximation as $P_{\text{lin}} \propto k^\nu$, and

hence it controls the convergence of the loop integrals. Most of the 22-type integrals that we encounter converge for $-1 < \nu < 1/2$. The lower end of this range corresponds to spurious IR contributions that cancel in the power spectrum due to the equivalence principle [130,137]. If this IR contribution is taken into account, one can choose an FFTLog bias in the range $-3 < \nu < -1$. Certain bias integrals, like the ones proportional to $b_2^2$, converge only for $-3 < \nu < -3/2$. For $\nu > -3/2$ they have formally UV-divergent constant parts that behave as [93,117]

$$I_{\delta^2 \delta^2}(0) \equiv \frac{1}{2} \int_{\mathbf{q}} P_{\text{lin}}^2(q). \quad (3.25)$$

In the case of galaxies the standard practice is to subtract these terms from the final answer as they simply renormalize the constant shot-noise contribution. For the Lyman alpha, however, the intrinsic shot-noise contribution produced by tracer discreteness is negligibly small, while the constant piece (3.25) is quite large for the physical $\Lambda$CDM power spectrum,

$$I_{\delta^2 \delta^2}(0)|_{z=2.8} \approx 28 \ [h^{-1} \, \text{Mpc}]^3. \quad (3.26)$$

Note that this integral is saturated in the IR, so it would have the same value even if we cut it off at $\Lambda \sim k_{\text{NL}}$. Hence, Eq. (3.26) represents a calculable, physical constant power spectrum contribution that is deterministic by origin, and must be present in the model. Let us estimate its magnitude. When discussing the Tau model below, we will get a natural estimate $b_2 \sim 0.3$, so that

$$P_{\text{shot}} \sim \frac{b_2^2}{2} \int_{\mathbf{q}, |q| \le k_{\text{NL}}} P_{\text{lin}}^2(q) \approx b_2^2 \times I_{\delta^2 \delta^2}(0) \approx 2.5 \ [h^{-1} \, \text{Mpc}]^3.$$
$$(3.27)$$

This estimate is two orders of magnitude larger than the naive scaling Universe result $P_{\text{shot}} \sim k_{\text{NL}}^{-3} \sim 10^{-2} \ [h^{-1} \, \text{Mpc}]^3$, and also many orders of magnitudes larger than the actual discreteness shot noise.

The constant terms like (3.27) are fully calculable. They are produced mostly by perturbative modes and they do not require introducing new parameters as counterterms, as their UV sensitivity is very mild for $\Lambda$CDM. The deterministic constant pieces like (3.27) should be contrasted with the stochastic constant shot-noise contributions due to discreteness effects. The latter are extremely small for the Lyman alpha forest due to high-column densities, and hence can be neglected for the precision we are interested in. Note that unlike the stochastic constant pieces, the deterministic constant pieces do not require free parameters —their contributions are fully fixed in terms of nontrivial bias operators that survive in the limit $K_2(\mathbf{q}, -\mathbf{q})$, like $b_2$. In order to retain these terms, we choose the FFTLog bias for $P_{22}$-type integrals to be $\nu = -1.7$.

As far as the 13-type corrections are concerned, there is no single choice of $\nu$ that would make them converge both in the IR and UV. Following the discussion above, we use $\nu = -1.7$ that leads to the convergence in the UV, but misses the spurious IR-sensitive contributions. Together with our choice $\nu = -1.7$ for the $P_{22}$-type integrals, all spurious IR corrections are consistently absent in our loop integrals.

The convergent UV contributions of one-loop integrals are proportional to the displacement variance,

$$\sigma_v^2 = \frac{1}{3}\int_{\mathbf{q}} \frac{P_{\text{lin}}(q)}{q^2}|_{\Lambda\text{CDM}, z=2.8} = 4.0\ [h^{-1}\ \text{Mpc}]^2. \qquad (3.28)$$

With our choice of the FFTLog bias, this correction is computed over the entire range of scales. The physical calculable part, however, should only involve modes with $k \lesssim k_{\text{NL}}$. This means that our choice of the FFTLog bias will introduce an error of

$$\frac{1}{6\pi^2}\int_{k_{\text{NL}}}^{\infty} dq\, q^2\, \frac{P_{\text{lin}}(q)}{q^2} \approx 4 \times 10^{-3}\ [h^{-1}\ \text{Mpc}]^2. \qquad (3.29)$$

Even if this error is very small in absolute terms, we will find that the Sherwood data is actually sensitive to these corrections. This is another reason to keep the higher-derivative counterterms in the fit; they compensate for errors in loop calculations.

## IV. TOP-DOWN DERIVATION FROM THE EXPONENTIAL MAP

The symmetry-based EFT expansions (3.15) and (3.17) are complete and general. It is interesting to see directly how these expressions arise from the nonlinear transformation of the optical depth field. The optical depth itself is assumed to be a selection-free biased tracer of the underlying matter density, just like the galaxies. In that case all selection-dependent contributions in the flux bias model should stem from the exponential map. The main objective of this section is to show how this happens. Since we aim here at reproducing the known results (3.17), the content of this section would be somewhat academic in nature. We will argue that it still important to the general understanding of the perturbative Lyman alpha modeling.

The question of how the exponential map generates selection-dependent bias contributions was previously studied by Ref. [59]. Specifically, this work showed how the exponential map and the SPT kernels generate certain terms in the EFT expansion. In this chapter we build on results of [59] and study the relationship between the exponential map and the EFT bias expansion in more detail. The main novelty of our work is that we show explicitly that the mapping *and* the requirement of renormalization generate a full set of the line-of-sight dependent EFT operators (3.17). If we formally drop the requirement of renormalization, the exponential map will produce only a particular incomplete set of EFT operators with fixed Wilson coefficients, at the tree level. We call the corresponding perturbative model "the tree-level Tau model." Naively, this model is extremely predictive, as it requires only one extra parameter (velocity gradient bias, or the mean optical depth) in addition to the standard set of selection-free bias parameters. We show, however, that this model receives infinitely large-loop contributions, which renders it inconsistent. Once the loop corrections are appropriately renormalized, their finite pieces generate order one corrections to all bias parameters, which will break the tree-level constraints imposed by the exponential map. All in all, this means that even if we ignore counterterms in the perturbative expansion of the Lyman alpha forest flux at the beginning, the loop corrections will generate them and make the exponential map expansion equivalent to the full EFT.

### A. Renormalized exponential map expansion

We start with a top down derivation involving the renormalization of the flux contrast field. It is a nonlinear transformation of the optical depth field $\tau$, which we assume to be a selection-independent tracer of matter. The exponential map reads

$$F = e^{-\tau_0(1+\epsilon\delta_\tau)}, \qquad (4.1)$$

where $\tau_0$ is the mean optical depth. In this spirit of EFT, this is a "bare" parameter that has to be properly renormalized. We will address this issue soon. $\epsilon$ is our order counting parameter that keeps track of the order of our perturbative solution. It is to be set to 1 in the final result. Note that $\tau$ is a function of the redshift space space coordinate [5], i.e. the full RSD mapping (3.4) has already been applied to it. Taylor expanding Eq. (3.4) up to cubic order we obtain,[18]

$$\begin{aligned}
\delta_\tau^{(s)}(\mathbf{k}) = {} & \delta_\tau^{(r)}(\mathbf{k}) - \frac{ik_z v_{\tau,z}(\mathbf{k})}{\mathcal{H}} - \epsilon\frac{ik_z}{\mathcal{H}}[\delta_\tau^{(r)} v_{\tau,z}]_{\mathbf{k}} \\
& + \epsilon\frac{i^2 k_z^2}{2\mathcal{H}^2}[v_{\tau,z}^2]_{\mathbf{k}} + \epsilon^2\frac{i^2 k_z^2}{2\mathcal{H}^2}[v_{\tau,z}^2\delta_\tau^{(r)}]_{\mathbf{k}} \\
& - \epsilon^2\frac{i^3 k_z^3}{6\mathcal{H}^3}[v_{\tau,z}^2]_{\mathbf{k}}, \qquad (4.2)
\end{aligned}$$

where $\delta_\tau^{(r)}$ is the optical depth fluctuation field in real space, and we have used our bookkeeping parameter $\epsilon$ to trace perturbative order. In what follows we will drop the $(s)$ superscript and use $\delta_\tau$ for the optical depth contrast in redshift space. As a next step, we Taylor expand the expression (4.1),

---

[18]We use the notation $[g]_{\mathbf{k}} = \int d^3x\, e^{-i\mathbf{k}\mathbf{x}} g(\mathbf{x})$ for an arbitrary function $g(\mathbf{x})$.

$$F = e^{-\tau_0}\left(1 - \epsilon\tau_0\delta_\tau + \frac{(\epsilon\tau_0\delta_\tau)^2}{2} - \frac{(\epsilon\tau_0\delta_\tau)^3}{6} + O(\epsilon^4)\right), \quad (4.3)$$

We are interested in one-loop order so the series goes up to $O(\epsilon^4)$. At this order, assuming $\langle\delta_\tau\rangle = 0$, the mean flux is given by

$$\langle F \rangle = e^{-\tau_0}\left(1 + \epsilon^2\frac{\tau_0^2}{2}\langle\delta_\tau^2\rangle + \cdots\right). \quad (4.4)$$

The mean flux is a function of the "bare coupling" $\tau_0$ that receives corrections order by order in perturbation theory. These corrections are unobservable since they are absorbed into $\tau_0$ in order to produce the physically observable mean flux $\langle F \rangle$ after renormalization. The situation here is similar to the renormalization of the "bare" mean number density of galaxies in the context of the perturbative bias expansion [83]. The flux fluctuations are given by

$$\delta_F = -\tau_0\epsilon\delta_\tau + \frac{\tau_0^2}{2}\epsilon^2(\delta_\tau^2 - \langle\delta_\tau^2\rangle) - \frac{(\epsilon\tau_0\delta_\tau)^3}{6} + O(\epsilon^4). \quad (4.5)$$

Setting $\epsilon = 1$, and going into Fourier space we get,

$$\delta_F(\mathbf{k}) = -\tau_0\delta_\tau(\mathbf{k}) + \frac{\tau_0^2}{2}[\delta_\tau^2]_{\mathbf{k}} - \frac{(\tau_0)^3}{6}[\delta_\tau^3]_{\mathbf{k}}, \quad (4.6)$$

where $\delta_\tau$ is given in Eq. (4.2). Note that so far we have not used the selection-independent bias model for $\delta_\tau^{(r)}$. Similar to Eq. (4.2), the Taylor expansion above produces operators evaluated at the same point in space that are highly UV sensitive. In the EFT approach, we need to make sure that $\delta_F$ receives contributions only from modes up to $k_{\rm NL}$ that are under perturbative control. That means all functions in the rhs of Eq. (4.3), e.g. $\delta_\tau$ as well as the composite local operators $[\delta_\tau^2]$ and $[\delta_\tau^3]$ need to be renormalzied.

Let us start with the linear term $[\delta_\tau]$, see Eq. (4.2). First, one can plug the perturbative bias model for the real space $\delta_\tau$, which, according to our assumptions, does not have line-of-sight selection effects, see Eq. (3.1). This model is closed under renormalization so we do not need to add new counterterms. The velocity terms in Eq. (4.2) are renormalized in the standard way, see Ref. [122]. Hence, this term also does not require additional counterterms. Let us move to the operators $[\delta_\tau^2]$ and $[\delta_\tau^3]$. Their renormalized versions must include all possible counterterms built out of the long-wavelength fields and allowed by symmetries. In our case these are the equivalence principle and $SO(2)$ rotations around the line of sight. The equivalence principle means the counterterms can only be functions of $\partial_i\partial_j\Phi$ and $\partial_i v_j$ and time derivatives along the flow. Up to cubic order, these operators have already been introduced in Eq. (3.15). Thus, we write

$$[\delta_\tau^2]_{\mathbf{k}}|_{\rm ren} = [\delta_\tau^2]_{\mathbf{k}} + b_1'\delta + b_\eta'\hat{z}^i\hat{z}^j\partial_i\partial_j\Phi + \sum b_{\mathcal{O}}'\mathcal{O},$$

$$[\delta_\tau^3]_{\mathbf{k}}|_{\rm ren} = [\delta_\tau^3]_{\mathbf{k}} + b_1''\delta + b_\eta''\hat{z}^i\hat{z}^j\partial_i\partial_j\Phi + \sum b_{\mathcal{O}}''\mathcal{O}, \quad (4.7)$$

where $\sum b_{\mathcal{O}}'^{,''}\mathcal{O}$ stand for the quadratic and cubic operators in Eq. (3.15). This way we generate all the terms in the expansion that we already had before in the "bottom-up" case. The bias coefficients $b_{\mathcal{O}}'$ and $b_{\mathcal{O}}''$, along with the biases present in $[\delta_\tau^n]_{\mathbf{k}}$, will sum up into the bias coefficients of Eq. (3.15). Note that velocity-dependent contributions dictated by the equivalence principle are contained inside the expressions $\delta_\tau^2$ and $\delta_\tau^3$. They are unaffected by the counterterms, as the EFT cannot generate terms that depend on the velocity itself, only on its gradients. All in all, this way we have arrived at the same EFT expansion as Eq. (3.15). We see that even if we start directly from the exponential map, the smoothing and renormalization will generate all the necessary selection-dependent bias operators.

To sum up, the renormalization procedure requires that coarse-grained composite operators stemming from the exponential map contain all possible line-of-sight dependent bias operators as counterterms,

$$[\delta_\tau^n]_{\mathbf{k}}|_{\rm ren} = [\delta_\tau^n]_{\mathbf{k}} + \text{counterterms}. \quad (4.8)$$

This is similar to usual renormalization conditions for local operators in quantum field theory. If we were to ignore the counterterms, the perturbative expansion generated by the exponential map would only involve simple contractions of $\delta_\tau^n$ whose bias coefficients would be completely fixed by the mapping. It is instructive to study the structure of this expansion and contrast it with the full EFT. Since the counterterms are typically considered along the loop corrections, with some abuse of language we call such an expansion "the tree-level Tau model." The goal of this discussion is to give a pedagogical example of how the counterterms in Eq. (4.8) will reappear from loops even if we ignore them to begin with.

### B. Tree-level Tau model

Let us study in more detail the "unrenormalized" part of the exponential map expansion. A similar derivation was recently done by [59]. We reproduce parts of this derivation here and extend the results of [59] to nonlinear selection-dependent bias terms. It is interesting to re-derive them again in the context of the standard perturbation theory (SPT) without renormalization [88]. Our starting point would be the exponential map (4.1) that we will Taylor expand and arrive at Eq. (4.5) for the fluctuations. The difference now is that we assume that fluctuations of $\tau$ are perturbative in the matter density, and they satisfy the standard bias expansion similar to (3.1),[19]

---

[19]In the SPT context this assumption is wrong because it is precisely coarse-graining and renormalization that guarantee the adequacy of the perturbative regime.

$$\delta_\tau = \delta_\tau^{(1)} + \epsilon\delta_\tau^{(2)} + \epsilon^2\delta_\tau^{(3)},$$

where $\delta_\tau^{(n)} \sim Z_n[\delta^{(1)}]^n$. Plugging this into (4.5) we get,

$$\delta_F = -\tau_0\epsilon\delta_\tau^{(1)} - \tau_0\epsilon^2\delta_\tau^{(2)} - \tau_0\epsilon^3\delta_\tau^{(3)} + \frac{\tau_0^2\epsilon^2}{2}((\delta_\tau^{(1)})^2 + 2\epsilon\delta_\tau^{(2)}\delta_\tau^{(1)} - \langle\delta_\tau^2\rangle) - \frac{(\epsilon\tau_0\delta_\tau^{(1)})^3}{6} + O(\epsilon^4). \tag{4.9}$$

Using the explicit expression for the standard redshift-space kernels (3.8), the expansion above can be rewritten in Fourier space in the standard perturbation theory form as

$$\delta_g^{(s)}(\mathbf{k}) = \tilde{K}_1(\mathbf{k})\delta_{\mathbf{k}}^{(1)} + \int_{\mathbf{q}_1}\int_{\mathbf{q}_2}(2\pi)^3\delta_D(\mathbf{k}-\mathbf{q}_{12})\tilde{K}_2(\mathbf{q}_1,\mathbf{q}_2)\delta_{\mathbf{q}_1}^{(1)}\delta_{\mathbf{q}_2}^{(1)}$$
$$+ \int_{\mathbf{q}_1}\int_{\mathbf{q}_2}\int_{\mathbf{q}_3}(2\pi)^3\delta_D(\mathbf{k}-\mathbf{q}_{123})\tilde{K}_3(\mathbf{q}_1,\mathbf{q}_2,\mathbf{q}_3)\delta_{\mathbf{q}_1}^{(1)}\delta_{\mathbf{q}_2}^{(1)}\delta_{\mathbf{q}_3}^{(1)} + \cdots, \tag{4.10}$$

where

$$\tilde{K}_1(\mathbf{k}) = (-\tau_0 b_1^\tau) + (-\tau_0)f\mu^2,$$

$$\tilde{K}_2(\mathbf{k}_1,\mathbf{k}_2) = \frac{(-\tau_0 b_2^\tau)}{2} + (-\tau_0 b_{\mathcal{G}_2}^\tau)\left(\frac{(\mathbf{k}_1\cdot\mathbf{k}_2)^2}{k_1^2 k_2^2} - 1\right) + (-\tau_0 b_1^\tau)F_2(\mathbf{k}_1,\mathbf{k}_2) - \tau_0 f\mu^2 G_2(\mathbf{k}_1,\mathbf{k}_2)$$
$$- \tau_0\frac{f\mu k}{2}\left(\frac{\mu_1}{k_1}(b_1^\tau + f\mu_2^2) + \frac{\mu_2}{k_2}(b_1^\tau + f\mu_1^2)\right) + \frac{\tau_0^2}{2}((b_1^\tau)^2 + b_1^\tau f(\mu_1^2 + \mu_2^2) + f^2\mu_1^2\mu_2^2),$$

$$\tilde{K}_3(\mathbf{k}_1,\mathbf{k}_2,\mathbf{k}_3) = -\tau_0 Z_3(\mathbf{q}_1,\mathbf{q}_2,\mathbf{q}_3) + \tau_0^2[Z_2(\mathbf{q}_1,\mathbf{q}_2)Z_1(\mathbf{q}_3)]_{\text{symm}} - \frac{\tau_0^3}{3!}Z_1(\mathbf{q}_1)Z_1(\mathbf{q}_2)Z_1(\mathbf{q}_3). \tag{4.11}$$

Comparing the linear kernel $\tilde{K}_1$ with the EFT expression (3.19) we identify

$$b_1 = -\tau_0 b_1^\tau,$$
$$b_\eta = \tau_0. \tag{4.12}$$

As anticipated, the exponential map generates the velocity gradient bias already at the linear level [79]. Let us focus now on the quadratic kernel $\tilde{K}_2$. Rewriting an expression in second line of the $\tilde{K}_2$ expansion above as

$$-\tau_0\frac{f\mu k}{2}\left(\frac{\mu_1}{k_1}(b_1^\tau + f\mu_2^2) + \frac{\mu_2}{k_2}(b_1^\tau + f\mu_1^2)\right) + \frac{\tau_0^2}{2}(b_1^\tau f(\mu_1^2 + \mu_2^2) + f^2\mu_1^2\mu_2^2)$$
$$= -f(\tau_0 b_1^\tau - \tau_0^2 b_1^\tau)\frac{\mu_2^2 + \mu_1^2}{2} + \left(-\tau_0 + \frac{\tau_0^2}{2}\right)f^2\mu_1^2\mu_2^2$$
$$+ (-\tau_0 b_1^\tau)f\frac{\mu_1\mu_2}{2}\left(\frac{k_2}{k_1} + \frac{k_1}{k_2}\right) - \tau_0 f^2\frac{\mu_1\mu_2}{2}\left(\frac{k_2}{k_1}\mu_2^2 + \frac{k_1}{k_2}\mu_1^2\right), \tag{4.13}$$

and matching the entire kernel with (3.19) we obtain:

$$b_2 = -\tau_0 b_2^\tau + \tau_0^2(b_1^\tau)^2, \qquad b_{\mathcal{G}_2} = -\tau_0 b_{\mathcal{G}_2}^\tau, \qquad b_{\delta\eta} = \tau_0 b_1^\tau - \tau_0^2 b_1^\tau,$$

$$b_{\eta^2} = -\tau_0 + \frac{\tau_0^2}{2}, \qquad b_{(KK)_\parallel} = 0, \qquad b_{\Pi_\parallel^{[2]}} = 0. \tag{4.14}$$

Assuming that the bias parameters of the optical depth field are order-one numbers, just like those of galaxies, $b_1^\tau \sim b_2^\tau \sim 1$, we get an estimate $b_1 \sim b_2 \sim \tau_0 \approx 0.3$ [53].

As far as the $\tilde{K}_3$ are concerned, we see that in addition to the standard term $\sim Z_3$, there are new contributions proportional to $Z_1^3$ and $Z_2 Z_1$ kernels, which are generated by the exponential map. However, one can easily check that only the $Z_2 Z_1$ term contributes nontrivially to the one-loop power spectrum. More specifically, only the term containing $G_2$ has a finite contribution that consistency reproduces the cubic order terms that must stem from the nontrivial $\delta\eta$, $\eta^2$ and $\eta$ operators. The rest of the additional

contributions are proportional to the UV-diverging mass variance

$$\sigma_\Lambda^2 = \int_0^\Lambda \frac{dq}{2\pi^2} q^2 P_{\text{lin}}(q), \qquad (4.15)$$

where $\Lambda$ is a UV cutoff. We will discuss the renormalization of these 13-type terms shortly. At the kinematic configurations relevant for the one-loop power spectrum we thus have

$$\int_{\mathbf{q}} \tilde{K}_3(\mathbf{k}, \mathbf{q}, -\mathbf{q}) P_{\text{lin}}(q) = -\tau_0 b_1^\tau \int_{\mathbf{q}} F_3(\mathbf{k}, \mathbf{q}, -\mathbf{q}) P_{\text{lin}}(q) - f\tau_0 \mu^2 \int_{\mathbf{q}} G_3(\mathbf{q}, -\mathbf{q}, \mathbf{k}) P_{\text{lin}}(q) + \int_{\mathbf{q}} [1 - (\hat{\mathbf{k}} \cdot \hat{\mathbf{q}})^2] P_{\text{lin}}(q)$$

$$\times \left\{ \frac{4}{21}(5b_{\mathcal{G}_2} + 2b_{\Gamma_3}) \left[ \left( \frac{(\mathbf{k}-\mathbf{q})\cdot\mathbf{q}}{|\mathbf{k}-\mathbf{q}|q} \right)^2 - 1 \right] - \frac{2}{21}f\left( -\tau_0 + \frac{\tau_0^2}{2} \right) \left[ \frac{3(k_\parallel - q_\parallel)^2}{|\mathbf{k}-\mathbf{q}|^2} + \frac{5q_\parallel^2}{q^2} \right] \right.$$

$$+ \frac{4}{7}f^2(\tau_0 b_1^\tau - b_1^\tau \tau_0^2) \frac{q_\parallel^2}{q^2} \frac{(k_\parallel - q_\parallel)^2}{|\mathbf{k}-\mathbf{q}|^2} + \frac{2}{21}f(-\tau_0 b_1^\tau) \left[ 5\frac{q_\parallel(k_\parallel - q_\parallel)}{q^2} + 3\frac{q_\parallel(k_\parallel - q_\parallel)}{|\mathbf{k}-\mathbf{q}|^2} \right]$$

$$\left. - \frac{2}{7}f^2\tau_0 \frac{q_\parallel(k_\parallel - q_\parallel)}{q^2|\mathbf{k}-\mathbf{q}|^2} [(k_\parallel - q_\parallel)^2 + q_\parallel^2] \right\}. \qquad (4.16)$$

Comparing this with the full EFT expression, we observe that the Tau model predicts that all EFT cubic biases are zero except $b_{\Gamma_3} = -\tau_0 b_{\Gamma_3}^\tau$.

We call Eq. (4.11) the tree-level Tau model. This model involves only one extra parameter, $\tau_0$. It also suggests that most of the one-loop selection-dependent EFT operators vanish,

$$b_{(KK)_\parallel} = b_{\Pi_\parallel^{[2]}} = b_{\Pi_\parallel^{[3]}} = b_{\delta\Pi_\parallel^{[2]}} = b_{\eta\Pi_\parallel^{[2]}} = b_{(K\Pi^{[2]})_\parallel} = 0, \qquad (4.17)$$

and that all nontrivial quadratic selection-dependent biases in the EFT expansion can be expressed through linear biases as

$$b_{\delta\eta} = -b_1(1 - b_\eta), \qquad b_{\eta^2} = -b_\eta + \frac{b_\eta^2}{2}. \qquad (4.18)$$

Our discussion so far has not included the loop corrections, which we discuss in detail now.

### C. The effect of loop corrections

The inconsistencies of the tree-level Tau model become apparent once we take loops into account. In particular, they will generate formally infinite corrections to the tree-level bias parameters of the linear density and projected velocity-gradient fields. These biases get renormalized by the following $P_{13}$-type contribution:

$$\delta P_{13} = (b_1 - b_\eta f\mu^2) P_{\text{lin}}(k) \int_{\mathbf{q}} P_{\text{lin}}(q)[(-\tau_0)^3(b_1^\tau$$
$$+ f\mu^2) Z_1^2(\mathbf{q}) + 4\tau_0^2 Z_2(\mathbf{k}, \mathbf{q}) Z_1(\mathbf{q})], \qquad (4.19)$$

which produces the leading order in $k$ UV contributions. The above integral can be done exactly, except for the term that contains $\sim G_2$ in the rightmost term. The exact part of

this expression is simply proportional to the short-scale mass variance (4.15), see Appendix B. The nontrivial part of the $Z_2 Z_1$ contribution has the same UV limit, proportional to $\sigma_\Lambda^2$. Thus, for the purposes of complete renormalization of the UV behavior, we need to add this part. This way we obtain

$$\delta P_{13}|_{\text{UV}} = 2(b_1 - b_\eta f\mu^2) P_{\text{lin}}(k)(A_0 - A_2 f\mu^2)\sigma_\Lambda^2, \qquad (4.20)$$

where the order-one constants $A_0$ and $A_2$ can be found in Appendix B. Note that $b_1$ also receives contributions from the usual bias operators, but they can be treated in the standard way [117], and we will ignore these terms in our discussion for clarity.

It is convenient now to recover our bookkeeping perturbation theory parameter $\epsilon$. Adding the linear result, we obtain the following expression for the tree level plus the UV part of the one-loop power spectrum in the Tau model,

$$P_{\text{tree}}(k) + P_{1-\text{loop}}(k)|_{\text{UV}}$$
$$= (b_1 - b_\eta f\mu^2)^2 P_{\text{lin}}(k) + 2(b_1 - b_\eta f\mu^2)$$
$$\times P_{\text{lin}}(A_0 - A_2 f\mu^2)\epsilon^2\sigma_\Lambda^2$$
$$= P_{\text{lin}}(k)(b_1 + A_0\sigma_\Lambda^2\epsilon^2 - (\tau_0 + A_2\epsilon^2\sigma_\Lambda^2)f\mu^2)^2 + O(\epsilon^4), \qquad (4.21)$$

where $O(\epsilon^4)$ are formally two-loop corrections that can be ignored at the precision level we are interested in. We have seen that the leading-order loop corrections in the Tau model produce infinite contributions to the linear bias parameters, including the velocity gradient bias. This merely implies that the SPT expansion for the Lyman alpha forest is inconsistent, and one has to use the full EFT model that includes all operators allowed by symmetries.

In the EFT approach one must treat $b_1$ and $b_\eta$ as formally infinite "bare" parameters that absorb the leading order UV behavior from the loops. Then their finite, physically observable, renormalized values of $b_1$ and $b_\eta$ are given by the sum of the "bare" parameters and the UV-sensitive loop contribution,

$$b_\eta^{\rm ren} = \tau_0 + A_2\sigma_\Lambda^2, \qquad b_1^{\rm ren} = -\tau_0 b_1^\tau + A_0\sigma_\Lambda^2\epsilon^2. \qquad (4.22)$$

Let us estimate the finite part of $b_\eta^{\rm ren}$ now. To that end we can use $\Lambda \sim k_{\rm NL}$, so that $\sigma_{\rm NL}^2 \sim 1$ by definition. In the absence of fine tuning, it should be of the order of

$$b_\eta^{\rm ren} \sim A_2\sigma_{\rm NL}^2 \sim 1, \qquad b_1^{\rm ren} \sim A_0\sigma_{\rm NL}^2 \sim 1. \qquad (4.23)$$

Hence, even if we take the tree-level Tau model at face value, the loops would generate an order-one breaking[20] of the relationship between the EFT operators following from the tree-level Tau model. Specifically, Eq. (4.23) implies that $b_\eta^{\rm ren}$ and $b_1^{\rm ren}$ are order one different from $-\tau_0 b_1^\tau$ and $\tau_0$, and hence the tree-level exponential mapping constraints (4.18) do not hold once the loops are taken into account. This also suggests that the other constraint (4.17), i.e. the vanishing of specific selection-dependent EFT operators, would not hold true as well because of the loops. This is quite natural to expect, as there is no symmetry that would guarantee the vanishing of these operators in the presence of loops. In the EFT jargon one says that operators like $\Pi_\parallel^{[2]}$ are generated by loops even if they are not present in the exponential mapping at the tree level.

## V. COMPARISON WITH SIMULATIONS

### A. Fitting details

In this section we compare the one-loop EFT power spectrum model for the Lyman alpha-flux power spectrum against simulation data. To that end we use the state-of-the-art suite of Sherwood simulations [52]. These are large-scale, high-resolution hydrodynamic simulations that reproduce the evolution of intergalactic medium with a large number of particles (up to $1.7 \times 10^{10}$). The fiducial cosmology of these simulations is a flat $\Lambda$CDM with massless neutrinos and $\Omega_m = 0.308$, $\Omega_b = 0.0482$, $\sigma_8 = 0.829$, $n_s = 0.961$, $h = 0.678$. The details of the Sherwood simulations can be found in Refs. [52,60].

In this work, we fit the 3D Lyman alpha power spectrum at $z = 2.8$, extracted from the simulation box L160_N2048, which followed $2048^3$ gas and cold dark matter particles in a cub with side length L = 160 $h^{-1}$ Mpc. The simulations use a homogeneous ionizing background

model, and assume that the gas is in ionization equilibrium and optically thin [52]. The final 3D power spectrum measurements are publicly available.[21] They are presented as functions of the Fourier mode wavenumber $k$ and the cosine $\mu$ of the angle between the corresponding Fourier vector and the line of sight. In practice, the $\mu$ space is sampled by 16 bins, while the $k$ space is log-sampled in the range $[k_F, k_{\rm Ny}]$, where $k_F = 0.039 \, h\,{\rm Mpc}^{-1}$ is the fundamental mode, and $k_{\rm Ny} = 20 \, h\,{\rm Mpc}^{-1}$ is the Nyquist frequency.

Following [60], we fit the power spectrum by Monte Carlo Markov chain (MCMC) sampling the following pseudo-$\chi^2$ function,

$$\chi^2 = \sum_i \frac{[P_i^{\rm data} - P^{\rm model}(k_i, \mu_i)]^2}{2(P_i^{\rm data})^2/N_i}, \qquad (5.1)$$

where $P_i^{\rm data}$ are measurement power spectrum bins, and $N_i$ is the number of modes in the bin. Note that in Eq. (5.1) we have explicitly assumed a Gaussian diagonal covariance for the power spectrum. While this assumption is definitely correct on large scales, it has not been systematically validated on small scales, relevant for our analysis. Studies of the galaxy power spectrum covariance in Refs. [138–140] showed that the Gaussian approximation is very accurate on mildly nonlinear scales because in this regime the effective covariance is dominated by the theoretical error due to the marginalization over nuisance parameters [141–143]. In what follows we assume that the same argument is true for the Lyman alpha power spectrum, and we proceed with the Gaussian diagonal covariance. We warn, however, that the interpretation of our results is, strictly speaking, contingent upon our covariance matrix assumptions.

Note that unlike [60], we do no add the *ad hoc* noise floor correction to the covariance, as our goal here is to fit the data given its actual precision. This allows us to illustrate the main advantage of the EFT over phenomenological approaches; its high precision on the scales where the EFT is applicable.

The model vector $P^{\rm model}(k_i, \mu_i)$ is a one-loop EFT model that includes the necessary stochastic contributions and counterterms,

$$\begin{aligned}
P^{1-\rm loop}(k, \mu) &= (b_1 - b_\eta f\mu^2)^2 P_{\rm lin}(k) \\
&+ 2\int_{\mathbf{q}} K_2^2(\mathbf{q}, \mathbf{k} - \mathbf{q})P_{\rm lin}(|\mathbf{k} - \mathbf{q}|)P_{\rm lin}(q) \\
&+ 6K_1(\mathbf{k})P_{\rm lin}(k)\int_{\mathbf{q}} K_3(\mathbf{k}, -\mathbf{q}, \mathbf{q})P_{\rm lin}(q) \\
&- 2(c_0 + c_2\mu^2 + c_4\mu^4)k^2 P_{\rm lin}(k). \qquad (5.2)
\end{aligned}$$

The $k^2 P_{\rm lin}$ corrections are added here as proxy for the two-loop contributions. For the purposes of the data analysis,

---

[20]From the structure of the renormalization condition Eq. (4.22) one can expect certain suppressions of the loop corrections due to the smallness of the mean optical depth $\tau_0 \approx 0.3$. We will not entertain this possibility in what follows.

[21]https://github.com/andreufont/sherwood_p3d.

we switched to a simplified version of the higher-derivative contribution that is motivated by the EFT-based galaxy power spectrum analyses, e.g. [70]. We have checked that adding an extra parameter $\propto k^2 \mu^6 P_{\text{lin}}(k)$ has no impact on the fit. In addition, we found that the effect of the stochastic counterterms [see Eq. (3.22)] is negligible for our data, and hence we set them to zero. This is consistent with our theoretical arguments.

At face value, the one-loop EFT model depends on 16 free parameters; two linear biases, 11 nonlinear biases, and three higher-derivative operators. We found, however, that the quality of our data does not allow us to break the known degeneracy between $b_{\mathcal{G}_2}$ and $b_{\Gamma_3}$ that exists at the power spectrum level [67,72,78,144]. We thus set $b_{\Gamma_3} = 0$ following [67,145]. For the remaining parameters, we use the following priors:

$$b_1 \in [-2, 2], \qquad b_\eta \in [-2, 2], \qquad b_2 \sim \mathcal{N}(0, 2^2), \qquad b_{\mathcal{G}_2} \sim \mathcal{N}(0, 2^2),$$

$$b_{(KK)_\parallel} \sim \mathcal{N}(0, 2^2), \qquad b_{\Pi_\parallel^{[2]}} \sim \mathcal{N}(0, 2^2), \qquad b_{\Pi_\parallel^{[3]}} \sim \mathcal{N}(0, 2^2),$$

$$b_{\delta\eta} \sim \mathcal{N}(0, 2^2), \qquad b_{\eta^2} \sim \mathcal{N}(0, 2^2), \qquad \frac{c_{0,2,4}}{[h^{-1}\,\text{Mpc}]^2} \sim \mathcal{N}(0, 0.1^2),$$

$$b_{(K\Pi^{[2]})_\parallel} \sim \mathcal{N}(0, 2^2), \qquad b_{\delta\Pi_\parallel^{[2]}} \sim \mathcal{N}(0, 2^2), \qquad b_{\eta\Pi_\parallel^{[2]}} \sim \mathcal{N}(0, 2^2), \tag{5.3}$$

where $\mathcal{N}(\mu, \sigma^2)$ stands for a Gaussian distribution with mean $\mu$ and root mean square $\sigma$. Let us discuss in detail the motivation for this choice of priors. First, the priors for $b_1$ and $b_\eta$ are chosen to be flat and uninformative. Second, for all the quadratic and cubic selection-dependent bias parameters we choose large uninformative Gaussian priors with zero mean and variance square roots of 2. In general, the EFT naturalness arguments dictate that they should be $O(1)$ numbers, i.e. we expect them to roughly be in the range $[1, 10]$. We note, however, that some additional suppression may come from the mapping, i.e. the flux bias parameters are $O(1)$ bias parameters of the $\tau$ field that have got multiplied by $\tau_0 \simeq 0.3$. Given this reason, we reduced the root mean square of our prior to 2 instead, e.g. a conservative choice of 10 that could be made without any *a priori* knowledge.

As far as the counterterms are concerned, as we discussed earlier, we include them mainly in order to absorb some two-loop corrections that are not explicitly computed. Indeed, we have found that they actually improve the fit, which justifies their presence *a posteriori*. The typical size of these corrections expected in the EFT is $k_{\text{NL}}^{-2} \sim 0.05\,[h^{-1}\,\text{Mpc}]^2$. We additionally multiply this by 2 in order to be conservative. Indeed, one might expect the velocity field to be more nonlinear than the density one, and hence the $k^2$ contributions may be enhanced, as it is the case for galaxies [67,146]. Jumping ahead, let us note that we will actually find the higher-derivative corrections whose values are consistent with $k_{\text{NL}}^{-2}$, with errorbars that are much tighter than the priors.

Only the 15 nuisance parameters (5.3) are assumed to vary in our MCMC chains. We leave the fitting of cosmological parameters for future work. We sample the likelihood analytically marginalized over all parameters that enter the likelihood quadratically, i.e.

$$\{P_{\text{shot}}, c_0, c_2, c_4, b_{\Pi_\parallel^{[3]}}, b_{(K\Pi^{[2]})_\parallel}, b_{\delta\Pi_\parallel^{[2]}}, b_{\eta\Pi_\parallel^{[2]}}\},$$

as in Refs. [140,143]. The approximate posterior distributions and best-fit values for these parameters are later recovered from the MCMC chains for the marginalized likelihood. The rest of the EFT parameters in Eq. (5.3) are explicitly varied in our MCMC chains.

The MCMC chains are run with the Monte Python sampler [147,148] and analyzed with GetDist [149].

## B. Results

In Fig. 2 we present 1d and 2d marginalized posterior distributions for the bias parameters of the one-loop EFT model that were directly sampled in our chains. We show results for four choices of $k_{\text{max}} = 2, 3, 4$, and 5 $h\,\text{Mpc}^{-1}$. We see that the posteriors for $k_{\text{max}} = 2\,h\,\text{Mpc}^{-1}$ and $k_{\text{max}} = 3\,h\,\text{Mpc}^{-1}$ are fully consistent with each other. The contour for the $k_{\text{max}} = 4\,h\,\text{Mpc}^{-1}$ case is, however, significantly shifted w.r.t. the 2 and 3 $h\,\text{Mpc}^{-1}$ posteriors. Although the $k_{\text{max}} = 5\,h\,\text{Mpc}^{-1}$ contour shifts back inside the $k_{\text{max}} = 2\,h\,\text{Mpc}^{-1}$ posterior, it is still inconsistent with the $k_{\text{max}} = 3\,h\,\text{Mpc}^{-1}$ contour. These dramatic shifts and reduction of the posterior volume suggest that the fit is biased for $k_{\text{max}} = 4\,h\,\text{Mpc}^{-1}$ and $k_{\text{max}} = 5\,h\,\text{Mpc}^{-1}$ due to two-loop corrections that are not included in our model. As a frequentist confirmation of our scale cuts, we also see a significant deterioration of the best-fit $\chi^2$ statistic for $k_{\text{max}} > 3\,h\,\text{Mpc}^{-1}$. This suggests to choose the $k_{\text{max}} = 3\,h\,\text{Mpc}^{-1}$ case as a baseline. Note that a similar behavior of the posteriors when sliding $k_{\text{max}}$ was previously observed in the case of redshift-space galaxy mocks [145], where the same criterion of the "stability" and consistency of posteriors with respect to variations of $k_{\text{max}}$ was applied.

The best-fit values, 68% and 95% confidence limits for the fit parameters at $k_{\text{max}} = 3\,h\,\text{Mpc}^{-1}$ are presented in Table I. First, we see that the linear bias parameters $b_1$ and
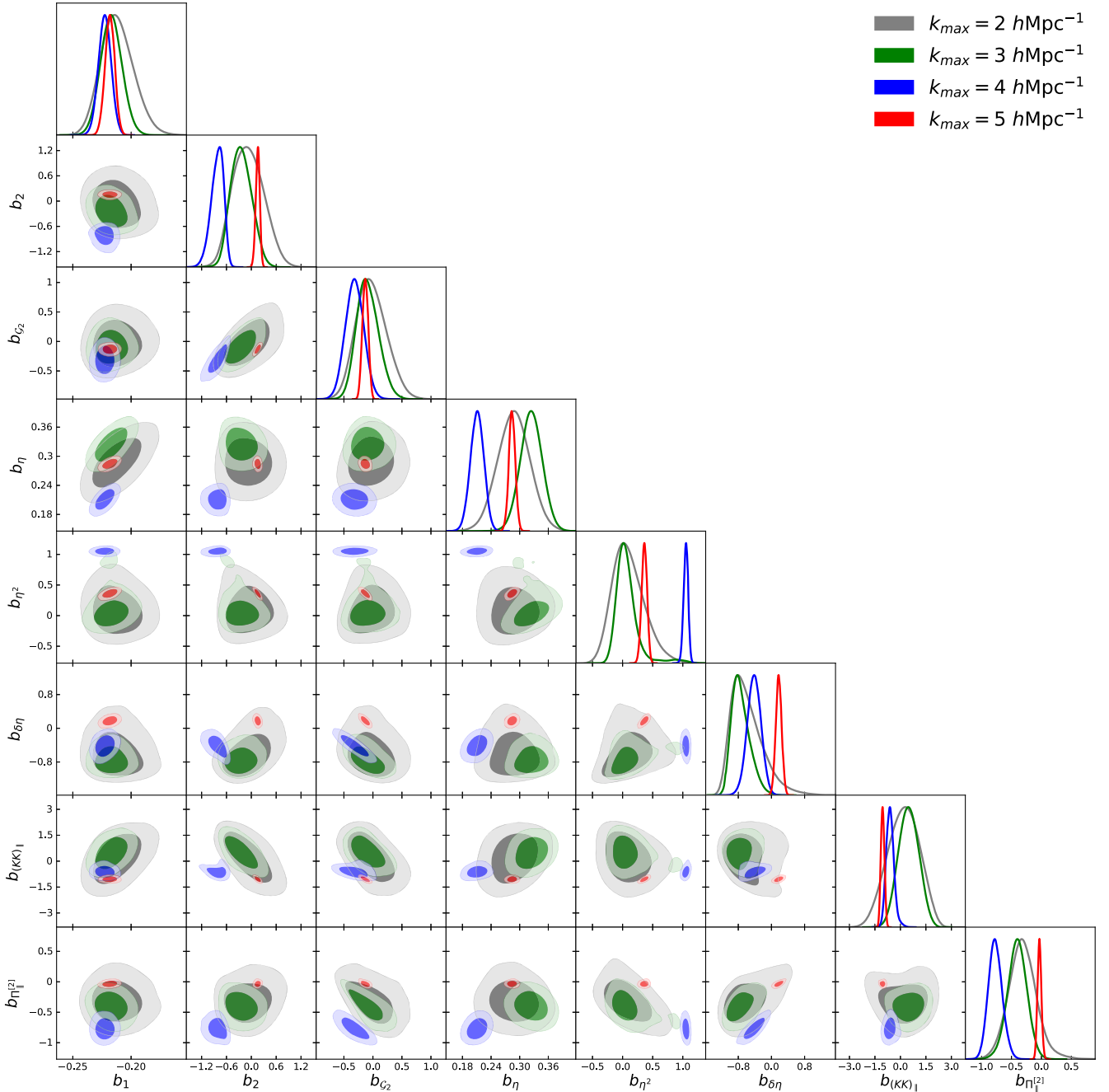
FIG. 2. Triangle plot and marginalized projections for bias parameters of the EFT model for the Lyman alpha flux power spectrum of the Sherwood simulations at $z = 2.8$. We show results for four choices of $k_{\max}$: 2, 3, 4, and 5 $h\,\mathrm{Mpc}^{-1}$ (gray, green, blue, red, respectively).

$b_{\eta}$ are measured to $\sim 5\%$ precision. The second important observation is that many Lyman-alpha bias parameters are detected at high significance; $b_{\delta\eta}$, $b_{\Pi^{[2]}_{\parallel}}$, $b_{\Pi^{[3]}_{\parallel}}$, $b_{(K\Pi^{[2]})_{\parallel}}$, $b_{\delta\Pi^{[2]}_{\parallel}}$, $b_{\eta\Pi^{[2]}_{\parallel}}$. Detections of these operators in the data clearly indicate an inconsistency of the tree-level Tau model, and the power of the EFT approach. The best-fit value of $b_{\delta\eta}$ is $4\sigma$ away from the prediction of the tree-level Tau model $\tilde{b}_{\delta\eta} = -b_1(1 - b_\eta) \approx 0.15$, evaluated with Eq. (4.18) using

the best-fit value of $b_\eta$. The apparent tension between the tree-level Tau model and the data is an "experimental" proof of the inconsistency of the tree-level calculations for the Lyman alpha forest. As far as higher-derivative counter-terms are concerned, we have a significant detection of $c_0$, and $c_2$.

The best-fit models for four angular bins are shown against the data in Fig. 3. The nominal $\chi^2$ statistics across the 161 data points is 188, which indicates a satisfactory fit

TABLE I. One-dimensional marginalized constraints on nuisance parameters of the one-loop EFT model fit to the Lyman alpha forest flux power spectrum of the Sherwood simulation at $z = 2.8$. The upper group of parameters were directly sampled in our MCMC chains. The lower parameters are analytically marginalized over in the likelihood. Their posteriors are recovered from the chains *a posteriori*.

| Parameters | Best-fit | Mean $\pm \sigma$ | 95% lower | 95% upper |
|---|---|---|---|---|
| $b_1$ | $-0.2168$ | $-0.2167^{+0.0093}_{-0.0096}$ | $-0.2356$ | $-0.1976$ |
| $b_\eta$ | $0.324$ | $0.325^{+0.023}_{-0.024}$ | $0.278$ | $0.373$ |
| $b_2$ | $-0.35$ | $-0.24^{+0.24}_{-0.28}$ | $-0.72$ | $0.27$ |
| $b_{\mathcal{G}_2}$ | $-0.14$ | $-0.087^{+0.18}_{-0.21}$ | $-0.46$ | $0.30$ |
| $b_{\eta^2}$ | $0.041$ | $0.072^{+0.1}_{-0.19}$ | $-0.28$ | $0.45$ |
| $b_{\delta\eta}$ | $-0.85$ | $-0.74^{+0.16}_{-0.26}$ | $-1.13$ | $-0.29$ |
| $b_{(KK)_\parallel}$ | $0.56$ | $0.48^{+0.6}_{-0.6}$ | $-0.63$ | $1.63$ |
| $b_{\Pi^{[2]}_\parallel}$ | $-0.41$ | $-0.41^{+0.16}_{-0.16}$ | $-0.72$ | $-0.08$ |
| $10^3 c_0/[h^{-1}\,\mathrm{Mpc}]^2$ | $4.90$ | $4.90^{+1.0}_{-1.0}$ | $2.80$ | $7.00$ |
| $10^3 c_2/[h^{-1}\,\mathrm{Mpc}]^2$ | $1.31$ | $1.31^{+0.62}_{-0.62}$ | $0.07$ | $2.54$ |
| $10^3 c_4/[h^{-1}\,\mathrm{Mpc}]^2$ | $-3.71$ | $-3.71^{+0.75}_{-0.75}$ | $-5.21$ | $-2.21$ |
| $b_{\Pi^{[3]}_\parallel}$ | $0.99$ | $0.99^{+0.05}_{-0.05}$ | $0.89$ | $1.08$ |
| $b_{\delta\Pi^{[2]}_\parallel}$ | $-1.03$ | $-1.03^{+0.05}_{-0.05}$ | $-1.13$ | $-0.93$ |
| $b_{(K\Pi^{[2]})_\parallel}$ | $-2.53$ | $-2.53^{+0.09}_{-0.09}$ | $-2.69$ | $-2.35$ |
| $b_{\eta\Pi^{[2]}_\parallel}$ | $1.67$ | $1.67^{+0.1}_{-0.1}$ | $1.47$ | $1.87$ |

for 15 free parameters. It is important to keep in mind, however, that our EFT parameters are quite degenerate and hence the counting of degrees of freedom is not straightforward in our case. In addition, our Gaussian covariance assumptions are likely not very accurate at the scales of interest. This is important to keep in mind when interpreting the $\chi^2$ statistics.

In order to illustrate the robustness of our fit, we extrapolate the $k_{\max} = 3\ h\,\mathrm{Mpc}^{-1}$ best fit model up to $k = 5\ h\,\mathrm{Mpc}^{-1}$ in Fig. 4. Remarkably, the model calibrated at $k_{\max} = 3\ h\,\mathrm{Mpc}^{-1}$ describes the data quite well, within 10%, even at $k = 3.5\ h\,\mathrm{Mpc}^{-1}$, beyond the regime of validity of the original fit. This can be interpreted as

evidence of absence of overfitting. We note, however, that the 10% residuals between the theory and the data are greater than the nominal errobars, which is why the fit at $k_{\max} = 4\ h\,\mathrm{Mpc}^{-1}$ was found earlier to be biased. The model breaks down gradually, reaching 20% at $k = 5\ h\,\mathrm{Mpc}^{-1}$, which is consistent with the effect of the higher-order corrections.

An important consistency check is that the one-loop corrections are smaller than the tree-level result. To verify that this is the case, in Fig. 5 we plot the one-loop contributions divided by the tree-level model (3.13). We see that the magnitude of the perturbative corrections does not exceed the linear theory power spectrum except for the
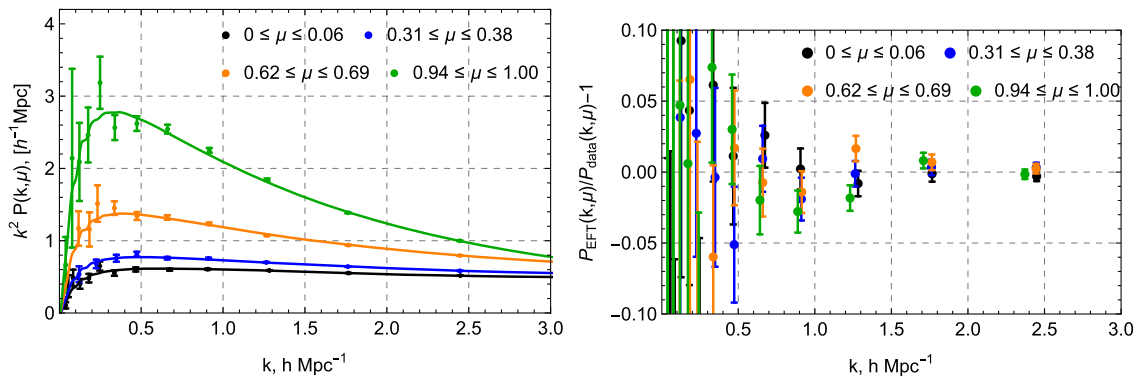


FIG. 3. Best-fit EFT models against the simulated power spectra (left panel), and the residuals between the model and the data (right panel).
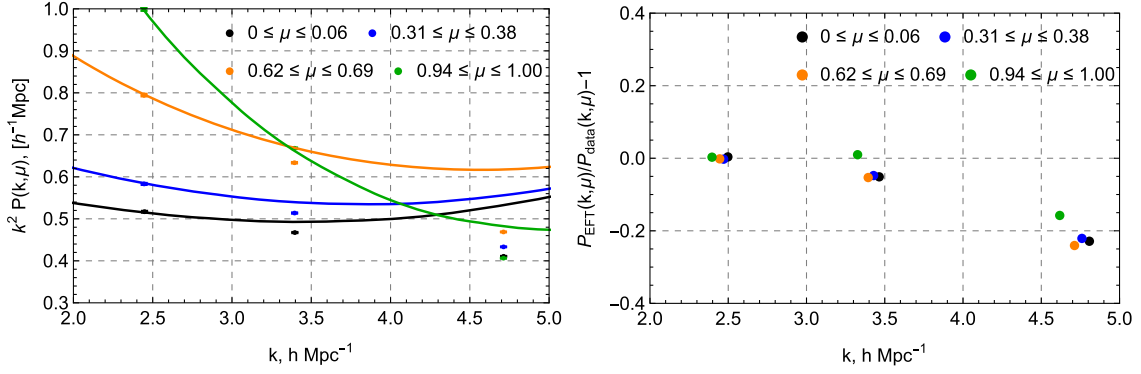
FIG. 4. Best-fit EFT models fit from $k_{max} = 3 \, h \, \text{Mpc}^{-1}$ against the simulated power spectra up to $k = 5 \, h \, \text{Mpc}^{-1}$ (left panel), and the residuals between them (right panel).

$\mu \simeq 0$ bin. The size of the one-loop corrections is comparable to the tree-level result for $k \simeq 3 \, h \, \text{Mpc}^{-1}$, which suggests that higher-loop corrections may not be negligible. Given that no biases are observed at the level of the parameter estimation, it is likely that the effect of the two-loop corrections was partly absorbed by the one-loop nuisance parameters and counterterms. A separate dedicated analysis is needed in order to quantify the effect of the two-loop corrections more accurately. We note however, that even if two-loop corrections are not negligible at $k = 3 \, h \, \text{Mpc}^{-1}$ in the strict sense, the EFT can still be applied on these scales as a phenomenological model that is capable of fitting the data with sub-percent accuracy.

Finally, the right panel of Fig. 5 illustrates that for the transverse ($\mu \approx 0$) modes the EFT provides a good fit even for $k_{max} = 4 \, h \, \text{Mpc}^{-1}$. This suggests that the breakdown of the one-loop model happens because of the velocity field that dominates the signal along the line of sight. Indeed, in general, the velocity field is more nonlinear than the density field for dark matter and galaxies [73,112,143,146,150]. Figure 5 shows, however, that the modes along the line of sight and transverse to the line of sight are roughly equally nonlinear for the Lyman alpha forest at $z = 2.8$. Overall, the quality of the $z = 2.8$ data does not allow us to make a

definitive conclusion about the role of the velocity nonlinearities. More insight may be obtained from the analysis of the $z = 3.2$ data, which we discuss below.

We present the analysis of the Lyman alpha forest power spectrum at $z = 3.2$ in Appendix C. At this redshift, the nonlinear wave number becomes significantly large, $k_{NL} = 10 \, h \, \text{Mpc}^{-1}$, suggesting that the EFT expansion should converge better and one can push the one-loop fit to smaller scales where the errorbars are smaller. We found that this is indeed the case. The EFT provides a good fit to the data up to $k_{max} = 5 \, h \, \text{Mpc}^{-1}$. The optimal values of the Lyman alpha bias parameters are larger at $z = 3.2$, and they are detected with higher significance, which is consistent with the expectations that tracers become more biased with redshift for uniform selection criteria. In particular, we have a significant detection of the RSD counterterms, whose impact increases towards $\mu = 1$, e.g. the $c_4$ counterterm is detected at almost $20\sigma$. This supports the above argument that the velocity field is primarily responsible for the breakdown of perturbation theory at small scales. On the practical side, this suggests that a more optimal strategy for parameter inference would be to use a $\mu$-dependent $k_{max}$ cutoff. We will explore this option in future work.
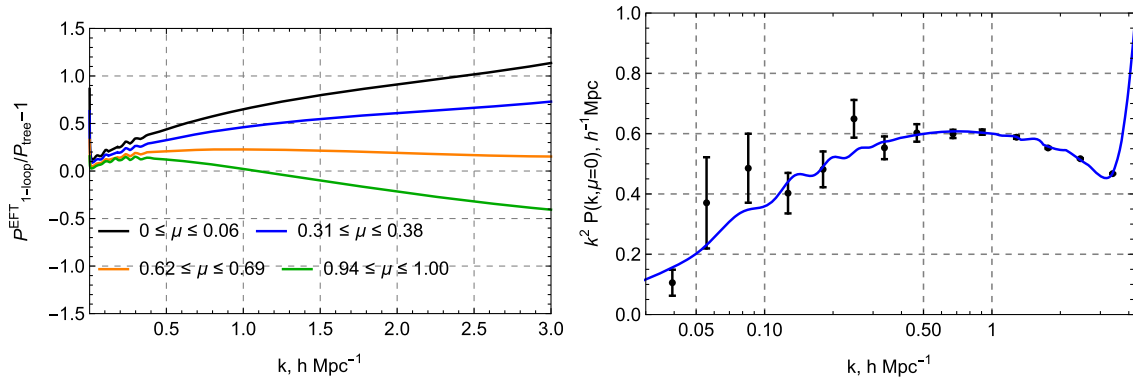


FIG. 5. Left panel: the magnitude of one-loop corrections relative to the linear theory answer. Right panel: the fit for the transverse modes.

## VI. ONE-DIMENSIONAL POWER SPECTRUM

We have seen that the EFT can accurately describe the full 3D power spectrum of the Lyman alpha forest. Let us show now how the EFT technique can be used to calculate the one-dimensional (1D) power spectrum of the Lyman alpha forests. Imagine that the flux fluctuations have an underlying power spectrum $P_{3D}(k, k_{\parallel})$ in 3D, where $k_{\parallel}$ is the wave vector projection along the line of sight. Then the power spectrum of these fluctuations seen only along the line of sight is given by [151]

$$P_{1D}(k_{\parallel}) = \frac{1}{2\pi} \int_{k_{\parallel}}^{\infty} dk\, k P_{3D}(k, k_{\parallel}). \qquad (6.1)$$

A conceptual difficulty of this observable is that the 1D power spectrum is an integral over the 3D power spectrum that involves UV modes that are not under robust analytic

control. This is precisely the issue that the EFT is aimed to resolve. In fact, Eq. (6.1) has the form of a loop integral, so we can treat this UV sensitivity along the lines of the one-loop EFT renormalization for the matter power spectrum [85]. To that end we assume that the integral in Eq. (6.1) is cut off at a scale $\Lambda \lesssim k_{NL}$. A first relevant observation is that in perturbation theory $P_{3D}(k, k_{\parallel})$ has a simple polynomial dependence on $k_{\parallel} = k \cdot \mu$. For instance, at one-loop order we have

$$P_{3D}(k, k_{\parallel}) = \sum_{n=0}^{4} \left( \frac{k_{\parallel}}{k} \right)^{2n} P_{2n}(k). \qquad (6.2)$$

A calculation of $P_{3D}(k, k_{\parallel})$ at a given order in perturbation theory is valid only up to a certain scale that we call $k_{trust}$. Then Eq. (6.1) can be equivalently recast as

$$P_{1D}(k_{\parallel}) = \frac{1}{2\pi} \int_{k_{\parallel}}^{k_{trust}} dk\, k P_{3D}(k, k_{\parallel}) + \frac{1}{2\pi} \int_{k_{trust}}^{\Lambda} dk\, k P_{3D}(k, k_{\parallel}). \qquad (6.3)$$

The rightmost integral is given by simple polynomials of $k_{\parallel}$ times some function of the cutoff,

$$\frac{1}{2\pi} \int_{k_{trust}}^{\Lambda} dk\, k P_{3D}(k, k_{\parallel}) = \sum_{n=0}^{4} k_{\parallel}^{2n} c_n^{\Lambda}, \qquad c_n^{\Lambda} \equiv \frac{1}{2\pi} \int_{k_{trust}}^{\Lambda} dk\, k^{1-2n} P_{2n}(k). \qquad (6.4)$$

These UV-sensitive contributions are naturally absorbed into the EFT stochastic counterterms, which have the scale dependence that exactly matches Eq. (6.4). Indeed, Eq. (3.22) implies that

$$P_{3D}^{stoch}(k, k_{\parallel}) = P_{shot} + a_0 \frac{k^2}{k_{NL}^2} + a_2 \frac{k_{\parallel}^2}{k_{NL}^2} + \cdots, \qquad (6.5)$$

where "$\cdots$" stand for terms higher order in $k/k_{NL}$. $P_{shot}, a_0, a_2$ above are $\Lambda$-dependent Wilson coefficients that cancel the UV sensitivity from the integrals (6.4). Plugging Eq. (6.5) into Eq. (6.3) we get

$$\begin{aligned}
\frac{1}{2\pi} \int_{k_{\parallel}}^{k_{trust}} dk\, k P_{3D}^{stoch}(k, k_{\parallel}) &= P_{shot} \frac{k_{trust}^2 - k_{\parallel}^2}{4\pi} + a_0 \frac{k_{trust}^4 - k_{\parallel}^4}{8\pi k_{NL}^2} + a_2 k_{\parallel}^2 \frac{k_{trust}^2 - k_{\parallel}^2}{4\pi k_{NL}^2} \\
&= \frac{2P_{shot}k_{trust}^2 + a_0 k_{trust}^4/k_{NL}^2}{8\pi} + k_{\parallel}^2 \left( a_2 \frac{k_{trust}^2}{4\pi k_{NL}^2} - \frac{P_{shot}}{4\pi} \right) + \frac{k_{\parallel}^4}{4\pi k_{NL}^2} \left( -\frac{a_0}{2} - a_2 \right), \\
&\equiv C_0' + k_{\parallel}^2 C_1' + k_{\parallel}^4 C_2'.
\end{aligned} \qquad (6.6)$$

Adding this to (6.4) we obtain a finite cutoff-independent expression,

$$\begin{aligned}
\frac{1}{2\pi} \int_{k_{\parallel}}^{k_{trust}} dk\, k P_{3D}^{shoch} + \frac{1}{2\pi} \int_{k_{trust}}^{\Lambda} dk\, k P_{3D} &= (C_0^{\Lambda} + C_0') + k_{\parallel}^2 (C_1^{\Lambda} + C_1') + k_{\parallel}^4 (C_2^{\Lambda} + C_2') + \cdots \\
&= C_0^{finite} + C_1^{finite} k_{\parallel}^2 + C_2^{finite} k_{\parallel}^4 + \cdots,
\end{aligned} \qquad (6.7)$$

where $c_n^{finite}$ are finite parts of the EFT coefficients that have to be matched to data. To sum up, in the EFT the 1D power spectrum calculation amounts to doing the integral over the deterministic part of the 3D spectrum up to $k_{trust}$, which is natural to identify with $k_{max}$ from our 3D fits, and supplementing it with simple power-law functions of $k_{\parallel}^2$ whose free parameters $c_n^{finite}$ need to be fit from the data,

$$P_{1D}^{EFT}(k_\parallel) = \frac{1}{2\pi} \int_{k_\parallel}^{k_{max}} dk\, k[P_{3D} - P_{stoch}] + C_0^{finite} + C_1^{finite} k_\parallel^2 + C_2^{finite} k_\parallel^4. \tag{6.8}$$

The part that contains "$-P_{stoch}$" can be reabsorbed into $c_0^{finite}$, yielding

$$P_{1D}^{EFT}(k_\parallel) = \frac{1}{2\pi} \int_{k_\parallel}^{k_{max}} dk\, k P_{3D}(k, k_\parallel) + C_0 + C_1 k_\parallel^2 + C_2 k_\parallel^4. \tag{6.9}$$

Note that counterterms similar to $C_n$ were first discussed in the context of regularization of the 1D Lyman alpha power spectrum integrals in [22]. In particular, our $C_0$ matches the counterterm $\bar{I}_0$ from [22].

Let us estimate calculable parts of the counter terms $C_n$ in our Universe for $z = 2.8$. To that end we can approximate them assuming $P_{3D}$ from linear theory up to $k_{max} = 3\ h\,\mathrm{Mpc}^{-1}$ and $k_{NL} = 5\ h\,\mathrm{Mpc}^{-1}$,

$$C_n \simeq \begin{cases} \int_{k_{max}}^{k_{NL}} \frac{dk}{2\pi}\, k b_1^2 P_{lin}(k) = 0.02\ [h^{-1}\,\mathrm{Mpc}], & n = 0, \\ \int_{k_{max}}^{k_{NL}} \frac{dk}{2\pi}\, k^{-1}(-2b_1 b_\eta) P_{lin}(k) = 4 \times 10^{-3}\ [h^{-1}\,\mathrm{Mpc}]^3, & n = 1, \\ \int_{k_{max}}^{k_{NL}} \frac{dk}{2\pi}\, k^{-3} b_\eta^2 P_{lin}(k) = 3 \times 10^{-4}\ [h^{-1}\,\mathrm{Mpc}]^5, & n = 2, \end{cases} \tag{6.10}$$

where we used the best-fit values for $b_1$ and $b_\eta$ from Table I. We see that the power law contributions in the rhs of Eq. (6.9) are suppressed for small $k_\parallel$, so they represent a convergent gradient expansion, which justifies dropping higher-order terms in Eq. (6.9). In a power law Universe these terms naturally scale as powers of $k_\parallel/k_{NL}$. Using Eq. (2.5) we get the following order-of-magnitude estimates for the 1D power spectrum

$$\frac{k_\parallel}{2\pi} P_{1D}(k_\parallel) \sim k_\parallel \int_{k_\parallel}^{k_{NL}} dk \left[ \underbrace{\frac{k^{n+1}}{k_{NL}^{n+3}}}_{linear} + \underbrace{\frac{k^{2n+4}}{k_{NL}^{2n+6}}}_{1-loop} + \underbrace{\frac{k}{k_{NL}^3} + \frac{k^3}{k_{NL}^5} + \frac{k k_\parallel^2}{k_{NL}^5}}_{stochastic} \right]$$

$$= \underbrace{\frac{k_\parallel}{k_{NL}} - \frac{k_\parallel^{n+3}}{k_{NL}^{n+3}}}_{linear} + \underbrace{\frac{k_\parallel}{k_{NL}} - \frac{k_\parallel^{2n+6}}{k_{NL}^{2n+6}}}_{1-loop} + \underbrace{\frac{k_\parallel}{k_{NL}} - \frac{k_\parallel^3}{k_{NL}^3} + \frac{k_\parallel^3}{k_{NL}^3} - \frac{k_\parallel^5}{k_{NL}^5}}_{stochastic}. \tag{6.11}$$

First, we see that each term in this expansion, even the deterministic ones, produce stochastic-type contributions $\propto k_\parallel/k_{NL}$ from the upper limit of the integration. They contribute to the calculable part of the constant shot-noise contribution in 1D. The calculable parts of the higher-derivative stochastic contributions in 3D scale as $(k_\parallel/k_{NL})^3$ and $(k_\parallel/k_{NL})^5$, and hence are clearly suppressed in the limit $k_\parallel/k_{NL} \to 0$. The deterministic parts of the linear and one-loop corrections dominate over the stochastic contributions, but not so strongly as they did in 3D. In particular, the proper one-loop part scales as $(k_\parallel/k_{NL})^1$, the same way as the shot noise $(k_\parallel/k_{NL})$ terms, in contrast with $(k_\parallel/k_{NL})$ against $(k_\parallel/k_{NL})^3$ in the 3D case, see Eq. (2.7). This explains why the stochastic counterterms $P_{shot}$, $a_0$ and $a_2$ were not needed in the 3D fits, but appeared important for the 1D correlations.

To illustrate how does the EFT model for the 1D power spectrum Eq. (6.9) work in practice, it is natural to evaluate this expression for the best-fit model to the 3D power spectrum from the previous section at $k_{max} = 3\ h\,\mathrm{Mpc}^{-1}$.

The 3D power spectrum was actually fit only up to $k_{max} \approx 2.5\ h\,\mathrm{Mpc}^{-1}$ since there were no data points in the range $2.5 < k/(h\mathrm{Mpc}^{-1}) < 3$. Extrapolating our 3D best-fit into this range leads to an additional error, which affects the 1D modes with $k_\parallel \simeq k_{trust}$. We found, however, that this error can be largely canceled by introducing a higher-order counterterm $C_6 k_\parallel^6$. Thus, in addition to the usual 3D EFT counterterms, we need to introduce four free parameters in order to describe the 1D power spectrum at the percent precision. We fit all these extra counterterms $C_{0,2,4,6}$ to the 1D power spectrum data extracted from the same simulation box. The best-fit counterterm piece is given by

$$\frac{P_{1D}^{stoch}}{h^{-1}\ \mathrm{Mpc}} = 0.085 + 1.8 \times 10^{-3}\ [h^{-1}\,\mathrm{Mpc}]^2 k_\parallel^2$$
$$+ 3.1 \times 10^{-4}\ [h^{-1}\,\mathrm{Mpc}]^4 k_\parallel^4$$
$$- 4.2 \times 10^{-5}\ [h^{-1}\,\mathrm{Mpc}]^6 k_\parallel^6. \tag{6.12}$$

Note that these best-fit values are in perfect agreement with our estimates (6.10). The results are shown in Fig. 6.
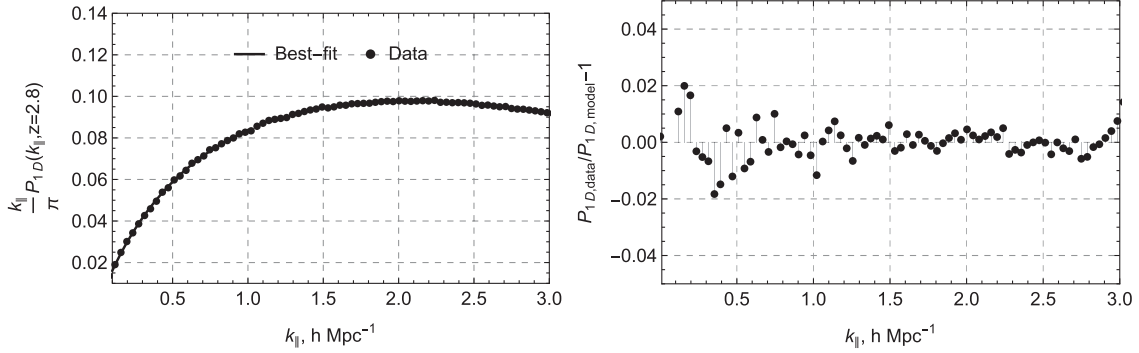
FIG. 6.   Left panel: dimensionless 1D flux power spectrum of the Sherwood simulations against the best-fit theory model from Eq. (6.9), where all the EFT parameters except $\mathcal{C}_n$'s are kept fixed to their 3D best-fit values. Right panel: residuals between the theory and the data.

We observe a perfect match between the theory and the data within the percent statistical scatter characteristic to the 1D power spectra of the Sherwood simulations, cf. Fig. 10 of [60]. Note however, that this good fit is obtained at the price of four extra parameters (6.12). Given that one can probe only line-of-sight modes, a large number of nuisance parameters may represent a problem in the context of actual cosmological analyses of the 1D Lyman-$\alpha$ flux power spectrum. We believe that the best way to proceed is to determine these parameters from high-fidelity Ly-$\alpha$ simulations and use these measurements as priors when analyzing the actual data. Similar ideas have been recently discussed in the context of galaxy clustering, see e.g. [114,152–154]. We leave this line of research for future work.

## VII. DISCUSSION AND CONCLUSIONS

We have developed a one-loop EFT model for the 3D and 1D power spectra of the Lyman alpha forest. As we discussed in Sec. III, this model is identical to that presented by Desjacques *et al.* [86] in the context of line-of-sight dependent selection effects in galaxy bias. We showed that the relevant loop integrals can be used to efficiently evaluated with the FFTLog method, which allows for an opportunity to carry out global full-shape analyses of the Lyman alpha data that include variations of cosmological parameters. This will enable one to explore the information content of the Lyman alpha forest along the lines of the recent EFT-based full-shape analyses of the galaxy power spectra [67,68]. This extension of our work is currently underway.

From the theoretical point of view, it is not immediately obvious that the line-of-sight dependent selection effect bias model of Desjacques *et al.* [86] would exactly match a perturbative expansion of the exponential map of the optical depth field in the context of the Lyman alpha forest transmission. The fact that the two should be in direct relationship was first pointed out by Chen *et al.* [59]. We have carried out an explicit deviations that shows how the full EFT model emerges from the exponential map of

the optical depth. From the technical point of view, the EFT expansion gets generated by the renormalization of the contact operators that stem down from the exponential map. To underline the importance of renormalization, we also carried out a naive expansion of the exponential map as one does in SPT. In that case an incomplete set of line-of-sight dependent operators is generated. Their bias coefficients are fixed by the optical depth contrast biases and the background optical depth value. We call this expansion the tree-level Tau model. We explicitly show this model is inconsistent as the loop corrections break constraints between the bias coefficients. Our calculation suggests that even if we ignored the counterterms to start with, the loop corrections would generate all line-of-sight dependent operators that are missing in the tree-level Tau model.[22]

On the data-related side, we have carried out a precision comparison of the one-loop EFT model and the highly accurate 3D Lyman alpha power spectra extracted from the Sherwood hydrodynamical simulations. We have found that the EFT model can successfully describe the broad-band shape of 3D and 1D power spectra, with $\lesssim 1\%$ residuals at $k_{\max} = 3\,h\,\mathrm{Mpc}^{-1}$ for $z = 2.8$. Note that at face value, these residuals are smaller than the ones of the phenomenological models used to fit the same the data in Ref. [60]. The results of this work, however, cannot be directly compared to ours, as in contrast to us, Ref. [60] assumed an additional 5% noise floor in their covariance.

As far as the measured values of the Lyman alpha biases are concerned, we have found strong deviations from the naive tree-level Tau model. First, we have observed a breakdown of the tight relationships between quadratic and linear bias parameters. In addition, we have detected quadratic and cubic line-of-sight operators missing in the tree-level Tau model. We warn, however, that our

---

[22]Although this exercise is of purely academic interest, the cleanest way to explicitly check this would be a calculation of the one-loop bispectrum of the Lyman alpha forest, which can be done along the lines of the recent one-loop redshift space galaxy bispectrum calculations [155,156].

measurements could be affected by degeneracies between the EFT nuisance parameters, covariance matrix assumptions, and simulations' systematics. It would be interesting to carry out a more detailed search for line-of-sight-dependent biases, especially at the bispectrum level. This line of research is also motivated by measurements of the Lyman alpha 3-point correlations in simulations [157] and the real data [7,158]. We leave this for future work.

Finally, we have also described how to consistently extend the EFT framework to the 1D power spectrum. Thus, our calculations can be applied to the one dimensional flux power spectrum data from BOSS [15].

Going forward, it would be important to explicitly implement IR resummation and use it to quantify the systematics of the BAO measurements. In addition, it would be interesting to study cross-correlations of galaxies and quasars with the Lyman alpha forest, similar to Refs. [60,159]. Another important line of work is to convert our formalism into configuration space, either using the FFTLog technique similar to [67], or developing the Lagrangian space EFT, along the lines of [136,160–164]. Eventually, we will have to account for realistic effects present in the actual data, such as the photoionization

fluctuations and patchy reionization. We leave all these research directions for future exploration.

## APPENDIX A: MASTER INTEGRALS

In this appendix we present master integrals that are necessary to compute the selection-dependent one-loop corrections. We will use the notation that $(\nu_{12} \equiv \nu_1 + \nu_2)$

$$J[\nu_1, \nu_2] \equiv \frac{1}{8\pi^{3/2}} \frac{\Gamma(\frac{3}{2} - \nu_1)\Gamma(\frac{3}{2} - \nu_2)\Gamma(\nu_{12} - \frac{3}{2})}{\Gamma(\nu_1)\Gamma(\nu_2)\Gamma(3 - \nu_{12})}. \quad (A1)$$

We have

$$
\begin{aligned}
A_5 = \frac{15}{256} (&J[-5 + \nu_1, \nu_2] - 5J[-4 + \nu_1, -1 + \nu_2] - 3J[-4 + \nu_1, \nu_2] \\
&+ 10J[-3 + \nu_1, -2 + \nu_2] + 4J[-3 + \nu_1, -1 + \nu_2] + 2J[-3 + \nu_1, \nu_2] \\
&- 10J[-2 + \nu_1, -3 + \nu_2] + 6J[-2 + \nu_1, -2 + \nu_2] \\
&+ 2J[-2 + \nu_1, -1 + \nu_2] + 2J[-2 + \nu_1, \nu_2] + 5J[-1 + \nu_1, -4 + \nu_2] \\
&- 12J[-1 + \nu_1, -3 + \nu_2] + 6J[-1 + \nu_1, -2 + \nu_2] + 4J[-1 + \nu_1, -1 + \nu_2] \\
&- 3J[-1 + \nu_1, \nu_2] - J[\nu_1, -5 + \nu_2] + 5J[\nu_1, -4 + \nu_2] - 10J[\nu_1, -3 + \nu_2] \\
&+ 10J[\nu_1, -2 + \nu_2] - 5J[\nu_1, -1 + \nu_2] + J[\nu_1, \nu_2]),
\end{aligned}
$$

$$
\begin{aligned}
B_5 = &-\frac{35}{128} J[-5 + \nu_1, \nu_2] + \frac{175}{128} J[-4 + \nu_1, -1 + \nu_2] + \frac{25}{128} J[-4 + \nu_1, \nu_2] \\
&-\frac{175}{64} J[-3 + \nu_1, -2 + \nu_2] + \frac{25}{32} J[-3 + \nu_1, -1 + \nu_2] + \frac{5}{64} J[-3 + \nu_1, \nu_2] \\
&+\frac{175}{64} J[-2 + \nu_1, -3 + \nu_2] - \frac{225}{64} J[-2 + \nu_1, -2 + \nu_2] + \frac{45}{64} J[-2 + \nu_1, -1 + \nu_2] \\
&+\frac{5}{64} J[-2 + \nu_1, \nu_2] - \frac{175}{128} J[-1 + \nu_1, -4 + \nu_2] + \frac{125}{32} J[-1 + \nu_1, -3 + \nu_2] \\
&-\frac{225}{64} J[-1 + \nu_1, -2 + \nu_2] + \frac{25}{32} J[-1 + \nu_1, -1 + \nu_2] + \frac{25}{128} J[-1 + \nu_1, \nu_2] \\
&+\frac{35}{128} J[\nu_1, -5 + \nu_2] - \frac{175}{128} J[\nu_1, -4 + \nu_2] + \frac{175}{64} J[\nu_1, -3 + \nu_2] \\
&-\frac{175}{64} J[\nu_1, -2 + \nu_2] + \frac{175}{128} J[\nu_1, -1 + \nu_2] - \frac{35}{128} J[\nu_1, \nu_2],
\end{aligned}
$$

$$C_5 = \frac{63}{256}J[-5+\nu_1,\nu_2] - \frac{315}{256}J[-4+\nu_1,-1+\nu_2] + \frac{35}{256}J[-4+\nu_1,\nu_2]$$
$$+ \frac{315}{128}J[-3+\nu_1,-2+\nu_2] - \frac{105}{64}J[-3+\nu_1,-1+\nu_2] + \frac{15}{128}J[-3+\nu_1,\nu_2]$$
$$- \frac{315}{128}J[-2+\nu_1,-3+\nu_2] + \frac{525}{128}J[-2+\nu_1,-2+\nu_2] - \frac{225}{128}J[-2+\nu_1,-1+\nu_2]$$
$$+ \frac{15}{128}J[-2+\nu_1,\nu_2] + \frac{315}{256}J[-1+\nu_1,-4+\nu_2] - \frac{245}{64}J[-1+\nu_1,-3+\nu_2]$$
$$+ \frac{525}{128}J[-1+\nu_1,-2+\nu_2] - \frac{105}{64}J[-1+\nu_1,-1+\nu_2] + \frac{35}{256}J[-1+\nu_1,\nu_2]$$
$$- \frac{63}{256}J[\nu_1,-5+\nu_2] + \frac{315}{256}J[\nu_1,-4+\nu_2] - \frac{315}{128}J[\nu_1,-3+\nu_2]$$
$$+ \frac{315}{128}J[\nu_1,-2+\nu_2] - \frac{315}{256}J[\nu_1,-1+\nu_2] + \frac{63}{256}J[\nu_1,\nu_2],$$

$$A_6 = -\frac{1}{1024} \times 5(J[-6+\nu_1,\nu_2] - 6J[-5+\nu_1,-1+\nu_2] - 6J[-5+\nu_1,\nu_2]$$
$$+ 15J[-4+\nu_1,-2+\nu_2] + 18J[-4+\nu_1,-1+\nu_2] + 15J[-4+\nu_1,\nu_2]$$
$$- 20J[-3+\nu_1,-3+\nu_2] - 12J[-3+\nu_1,-2+\nu_2] - 12J[-3+\nu_1,-1+\nu_2]$$
$$- 20J[-3+\nu_1,\nu_2] + 15J[-2+\nu_1,-4+\nu_2] - 12J[-2+\nu_1,-3+\nu_2]$$
$$- 6J[-2+\nu_1,-2+\nu_2] - 12J[-2+\nu_1,-1+\nu_2] + 15J[-2+\nu_1,\nu_2]$$
$$- 6J[-1+\nu_1,-5+\nu_2] + 18J[-1+\nu_1,-4+\nu_2] - 12J[-1+\nu_1,-3+\nu_2]$$
$$- 12J[-1+\nu_1,-2+\nu_2] + 18J[-1+\nu_1,-1+\nu_2] - 6J[-1+\nu_1,\nu_2]$$
$$+ J[\nu_1,-6+\nu_2] - 6J[\nu_1,-5+\nu_2] + 15J[\nu_1,-4+\nu_2]$$
$$- 20J[\nu_1,-3+\nu_2] + 15J[\nu_1,-2+\nu_2] - 6J[\nu_1,-1+\nu_2] + J[\nu_1,\nu_2]),$$

$$B_6 = \frac{105J[-6+\nu_1,\nu_2]}{1024} - \frac{315}{512}J[-5+\nu_1,-1+\nu_2] - \frac{135}{512}J[-5+\nu_1,\nu_2]$$
$$+ \frac{1575J[-4+\nu_1,-2+\nu_2]}{1024} + \frac{225}{512}J[-4+\nu_1,-1+\nu_2] + \frac{135J[-4+\nu_1,\nu_2]}{1024}$$
$$- \frac{525}{256}J[-3+\nu_1,-3+\nu_2] + \frac{225}{256}J[-3+\nu_1,-2+\nu_2] + \frac{45}{256}J[-3+\nu_1,-1+\nu_2]$$
$$+ \frac{15}{256}J[-3+\nu_1,\nu_2] + \frac{1575J[-2+\nu_1,-4+\nu_2]}{1024} - \frac{675}{256}J[-2+\nu_1,-3+\nu_2]$$
$$+ \frac{405}{512}J[-2+\nu_1,-2+\nu_2] + \frac{45}{256}J[-2+\nu_1,-1+\nu_2] + \frac{135J[-2+\nu_1,\nu_2]}{1024}$$
$$- \frac{315}{512}J[-1+\nu_1,-5+\nu_2] - \frac{675}{512}J[-1+\nu_1,-4+\nu_2] + \frac{405}{512}J[-1+\nu_1,-3+\nu_2]$$
$$+ \frac{225}{512}J[-1+\nu_1,-2+\nu_2] - \frac{135}{512}J[-1+\nu_1,-1+\nu_2] + \frac{105J[-1+\nu_1,\nu_2]}{1024}$$
$$+ \frac{105J[\nu_1,-6+\nu_2]}{1024} - \frac{315}{512}J[\nu_1,-5+\nu_2] + \frac{225}{512}J[\nu_1,-4+\nu_2]$$
$$- \frac{675}{512}J[\nu_1,-3+\nu_2] + \frac{1575J[\nu_1,-2+\nu_2]}{1024} - \frac{315}{512}J[\nu_1,-1+\nu_2] + \frac{105J[\nu_1,\nu_2]}{1024},$$

$$C_6 = -\frac{315J[-6+\nu_1,\nu_2]}{1024} + \frac{945}{512}J[-5+\nu_1,-1+\nu_2] + \frac{105}{512}J[-5+\nu_1,\nu_2]$$

$$-\frac{4725J[-4+\nu_1,-2+\nu_2]}{1024} + \frac{525}{512}J[-4+\nu_1,-1+\nu_2] + \frac{75J[-4+\nu_1,\nu_2]}{1024}$$

$$+\frac{1575}{256}J[-3+\nu_1,-3+\nu_2] - \frac{1575}{256}J[-3+\nu_1,-2+\nu_2] + \frac{225}{256}J[-3+\nu_1,-1+\nu_2]$$

$$+\frac{15}{256}J[-3+\nu_1,\nu_2] - \frac{4725J[-2+\nu_1,-4+\nu_2]}{1024} + \frac{2625}{256}J[-2+\nu_1,-3+\nu_2]$$

$$-\frac{3375}{512}J[-2+\nu_1,-2+\nu_2] + \frac{225}{256}J[-2+\nu_1,-1+\nu_2] + \frac{75J[-2+\nu_1,\nu_2]}{1024}$$

$$+\frac{945}{512}J[-1+\nu_1,-5+\nu_2] - \frac{3675}{512}J[-1+\nu_1,-4+\nu_2] + \frac{2625}{256}J[-1+\nu_1,-3+\nu_2]$$

$$-\frac{1575}{256}J[-1+\nu_1,-2+\nu_2] + \frac{525}{512}J[-1+\nu_1,-1+\nu_2] + \frac{105}{512}J[-1+\nu_1,\nu_2]$$

$$-\frac{315J[\nu_1,-6+\nu_2]}{1024} + \frac{945}{512}J[\nu_1,-5+\nu_2] - \frac{4725J[\nu_1,-4+\nu_2]}{1024}$$

$$+\frac{1575}{256}J[\nu_1,-3+\nu_2] - \frac{4725J[\nu_1,-2+\nu_2]}{1024} + \frac{945}{512}J[\nu_1,-1+\nu_2] - \frac{315J[\nu_1,\nu_2]}{1024},$$

$$D_6 = \frac{231J[-6+\nu_1,\nu_2]}{1024} - \frac{693}{512}J[-5+\nu_1,-1+\nu_2] + \frac{63}{512}J[-5+\nu_1,\nu_2]$$

$$+\frac{3465J[-4+\nu_1,-2+\nu_2]}{1024} - \frac{945}{512}J[-4+\nu_1,-1+\nu_2] + \frac{105J[-4+\nu_1,\nu_2]}{1024}$$

$$-\frac{1155}{256}J[-3+\nu_1,-3+\nu_2] + \frac{1575}{256}J[-3+\nu_1,-2+\nu_2] - \frac{525}{256}J[-3+\nu_1,-1+\nu_2]$$

$$+\frac{25}{256}J[-3+\nu_1,\nu_2] + \frac{3465J[-2+\nu_1,-4+\nu_2]}{1024} - \frac{2205}{256}J[-2+\nu_1,-3+\nu_2]$$

$$+\frac{3675}{512}J[-2+\nu_1,-2+\nu_2] - \frac{525}{256}J[-2+\nu_1,-1+\nu_2] + \frac{105J[-2+\nu_1,\nu_2]}{1024}$$

$$-\frac{693}{512}J[-1+\nu_1,-5+\nu_2] + \frac{2835}{512}J[-1+\nu_1,-4+\nu_2] - \frac{2205}{256}J[-1+\nu_1,-3+\nu_2]$$

$$+\frac{1575}{256}J[-1+\nu_1,-2+\nu_2] - \frac{945}{512}J[-1+\nu_1,-1+\nu_2] + \frac{63}{512}J[-1+\nu_1,\nu_2]$$

$$+\frac{231J[\nu_1,-6+\nu_2]}{1024} - \frac{693}{512}J[\nu_1,-5+\nu_2] + \frac{3465J[\nu_1,-4+\nu_2]}{1024}$$

$$-\frac{1155}{256}J[\nu_1,-3+\nu_2] + \frac{3465J[\nu_1,-2+\nu_2]}{1024} - \frac{693}{512}J[\nu_1,-1+\nu_2] + \frac{231J[\nu_1,\nu_2]}{1024},$$

$$A_7 = -\frac{1}{2048}\left(35J[-7+\nu_1,\nu_2] - 7J[-6+\nu_1,-1+\nu_2] - 5J[-6+\nu_1,\nu_2]\right.$$

$$+21J[-5+\nu_1,-2+\nu_2] + 18J[-5+\nu_1,-1+\nu_2] + 9J[-5+\nu_1,\nu_2]$$

$$-35J[-4+\nu_1,-3+\nu_2] - 15J[-4+\nu_1,-2+\nu_2] - 9J[-4+\nu_1,-1+\nu_2]$$

$$-5J[-4+\nu_1,\nu_2] + 35J[-3+\nu_1,-4+\nu_2] - 20J[-3+\nu_1,-3+\nu_2]$$

$$-6J[-3+\nu_1,-2+\nu_2] - 4J[-3+\nu_1,-1+\nu_2] - 5J[-3+\nu_1,\nu_2]$$

$$-21J[-2+\nu_1,-5+\nu_2] + 45J[-2+\nu_1,-4+\nu_2] - 18J[-2+\nu_1,-3+\nu_2]$$

$$-6J[-2+\nu_1,-2+\nu_2] - 9J[-2+\nu_1,-1+\nu_2] + 9J[-2+\nu_1,\nu_2]$$

$$+7J[-1+\nu_1,-6+\nu_2] - 30J[-1+\nu_1,-5+\nu_2] + 45J[-1+\nu_1,-4+\nu_2]$$

$$
\begin{aligned}
&- 20J[-1+\nu_1, -3+\nu_2] - 15J[-1+\nu_1, -2+\nu_2] + 18J[-1+\nu_1, -1+\nu_2] \\
&- 5J[-1+\nu_1, \nu_2] - J[\nu_1, -7+\nu_2] + 7J[\nu_1, -6+\nu_2] \\
&- 21J[\nu_1, -5+\nu_2] + 35J[\nu_1, -4+\nu_2] - 35J[\nu_1, -3+\nu_2] \\
&+ 21J[\nu_1, -2+\nu_2] - 7J[\nu_1, -1+\nu_2] + J[\nu_1, \nu_2]),
\end{aligned}
$$

$$
\begin{aligned}
B_7 = \frac{1}{2048} \big( &105(3J[-7+\nu_1, \nu_2] - 21J[-6+\nu_1, -1+\nu_2] - 7J[-6+\nu_1, \nu_2] \\
&+ 63J[-5+\nu_1, -2+\nu_2] + 14J[-5+\nu_1, -1+\nu_2] + 3J[-5+\nu_1, \nu_2] \\
&- 105J[-4+\nu_1, -3+\nu_2] + 35J[-4+\nu_1, -2+\nu_2] + 5J[-4+\nu_1, -1+\nu_2] \\
&+ J[-4+\nu_1, \nu_2] + 105J[-3+\nu_1, -4+\nu_2] - 140J[-3+\nu_1, -3+\nu_2] \\
&+ 30J[-3+\nu_1, -2+\nu_2] + 4J[-3+\nu_1, -1+\nu_2] + J[-3+\nu_1, \nu_2] \\
&- 63J[-2+\nu_1, -5+\nu_2] + 175J[-2+\nu_1, -4+\nu_2] - 150J[-2+\nu_1, -3+\nu_2] \\
&+ 30J[-2+\nu_1, -2+\nu_2] + 5J[-2+\nu_1, -1+\nu_2] + 3J[-2+\nu_1, \nu_2] \\
&+ 21J[-1+\nu_1, -6+\nu_2] - 98J[-1+\nu_1, -5+\nu_2] + 175J[-1+\nu_1, -4+\nu_2] \\
&- 140J[-1+\nu_1, -3+\nu_2] + 35J[-1+\nu_1, -2+\nu_2] + 14J[-1+\nu_1, -1+\nu_2] \\
&- 7J[-1+\nu_1, \nu_2] - 3J[\nu_1, -7+\nu_2] + 21J[\nu_1, -6+\nu_2] \\
&- 63J[\nu_1, -5+\nu_2] + 105J[\nu_1, -4+\nu_2] - 105J[\nu_1, -3+\nu_2] \\
&+ 63J[\nu_1, -2+\nu_2] - 21J[\nu_1, -1+\nu_2] + 3J[\nu_1, \nu_2]),
\end{aligned}
$$

$$
\begin{aligned}
C_7[\nu_1, \nu_2] = \frac{1}{2048} \big( &21(33J[-7+\nu_1, \nu_2] - 231J[-6+\nu_1, -1+\nu_2] - 21J[-6+\nu_1, \nu_2] \\
&+ 693J[-5+\nu_1, -2+\nu_2] - 126J[-5+\nu_1, -1+\nu_2] - 7J[-5+\nu_1, \nu_2] \\
&- 1155J[-4+\nu_1, -3+\nu_2] + 945J[-4+\nu_1, -2+\nu_2] - 105J[-4+\nu_1, -1+\nu_2] \\
&- 5J[-4+\nu_1, \nu_2] + 1155J[-3+\nu_1, -4+\nu_2] - 2100J[-3+\nu_1, -3+\nu_2] \\
&+ 1050J[-3+\nu_1, -2+\nu_2] - 100J[-3+\nu_1, -1+\nu_2] - 5J[-3+\nu_1, \nu_2] \\
&- 693J[-2+\nu_1, -5+\nu_2] + 2205J[-2+\nu_1, -4+\nu_2] - 2450J[-2+\nu_1, -3+\nu_2] \\
&+ 1050J[-2+\nu_1, -2+\nu_2] - 105J[-2+\nu_1, -1+\nu_2] - 7J[-2+\nu_1, \nu_2] \\
&+ 231J[-1+\nu_1, -6+\nu_2] - 1134J[-1+\nu_1, -5+\nu_2] + 2205J[-1+\nu_1, -4+\nu_2] \\
&- 2100J[-1+\nu_1, -3+\nu_2] + 945J[-1+\nu_1, -2+\nu_2] - 126J[-1+\nu_1, -1+\nu_2] \\
&- 21J[-1+\nu_1, \nu_2] - 33J[\nu_1, -7+\nu_2] + 231J[\nu_1, -6+\nu_2] \\
&- 693J[\nu_1, -5+\nu_2] + 1155J[\nu_1, -4+\nu_2] - 1155J[\nu_1, -3+\nu_2] \\
&+ 693J[\nu_1, -2+\nu_2] - 231J[\nu_1, -1+\nu_2] + 33J[\nu_1, \nu_2]),
\end{aligned}
$$

$$
\begin{aligned}
D_7 = \frac{1}{2048} \big( &429J[-7+\nu_1, \nu_2] - 3003J[-6+\nu_1, -1+\nu_2] + 231J[-6+\nu_1, \nu_2] \\
&+ 9009J[-5+\nu_1, -2+\nu_2] - 4158J[-5+\nu_1, -1+\nu_2] + 189J[-5+\nu_1, \nu_2] \\
&- 15015J[-4+\nu_1, -3+\nu_2] + 17325J[-4+\nu_1, -2+\nu_2] - 4725J[-4+\nu_1, -1+\nu_2] \\
&+ 175J[-4+\nu_1, \nu_2] + 15015J[-3+\nu_1, -4+\nu_2] - 32340J[-3+\nu_1, -3+\nu_2] \\
&+ 22050J[-3+\nu_1, -2+\nu_2] - 4900J[-3+\nu_1, -1+\nu_2] + 175J[-3+\nu_1, \nu_2] \\
&- 9009J[-2+\nu_1, -5+\nu_2] + 31185J[-2+\nu_1, -4+\nu_2] - 39690J[-2+\nu_1, -3+\nu_2]
\end{aligned}
$$

$$+ 22050J[-2 + \nu_1, -2 + \nu_2] - 4725J[-2 + \nu_1, -1 + \nu_2] + 189J[-2 + \nu_1, \nu_2]$$
$$+ 3003J[-1 + \nu_1, -6 + \nu_2] - 15246J[-1 + \nu_1, -5 + \nu_2] + 31185J[-1 + \nu_1, -4 + \nu_2]$$
$$- 32340J[-1 + \nu_1, -3 + \nu_2] + 17325J[-1 + \nu_1, -2 + \nu_2] - 4158J[-1 + \nu_1, -1 + \nu_2]$$
$$+ 231J[-1 + \nu_1, \nu_2] - 429J[\nu_1, -7 + \nu_2] + 3003J[\nu_1, -6 + \nu_2]$$
$$- 9009J[\nu_1, -5 + \nu_2] + 15015J[\nu_1, -4 + \nu_2] - 15015J[\nu_1, -3 + \nu_2]$$
$$+ 9009J[\nu_1, -2 + \nu_2] - 3003J[\nu_1, -1 + \nu_2] + 429J[\nu_1, \nu_2]),$$

$$A_8 = \frac{1}{32768}(35J[-8 + \nu_1, \nu_2] - 8J[-7 + \nu_1, -1 + \nu_2] - 8J[-7 + \nu_1, \nu_2]$$
$$+ 28J[-6 + \nu_1, -2 + \nu_2] + 40J[-6 + \nu_1, -1 + \nu_2] + 28J[-6 + \nu_1, \nu_2]$$
$$- 56J[-5 + \nu_1, -3 + \nu_2] - 72J[-5 + \nu_1, -2 + \nu_2] - 72J[-5 + \nu_1, -1 + \nu_2]$$
$$- 56J[-5 + \nu_1, \nu_2] + 70J[-4 + \nu_1, -4 + \nu_2] + 40J[-4 + \nu_1, -3 + \nu_2]$$
$$+ 36J[-4 + \nu_1, -2 + \nu_2] + 40J[-4 + \nu_1, -1 + \nu_2] + 70J[-4 + \nu_1, \nu_2]$$
$$- 56J[-3 + \nu_1, -5 + \nu_2] + 40J[-3 + \nu_1, -4 + \nu_2] + 16J[-3 + \nu_1, -3 + \nu_2]$$
$$+ 16J[-3 + \nu_1, -2 + \nu_2] + 40J[-3 + \nu_1, -1 + \nu_2] - 56J[-3 + \nu_1, \nu_2]$$
$$+ 28J[-2 + \nu_1, -6 + \nu_2] - 72J[-2 + \nu_1, -5 + \nu_2] + 36J[-2 + \nu_1, -4 + \nu_2]$$
$$+ 16J[-2 + \nu_1, -3 + \nu_2] + 36J[-2 + \nu_1, -2 + \nu_2] - 72J[-2 + \nu_1, -1 + \nu_2]$$
$$+ 28J[-2 + \nu_1, \nu_2] - 8J[-1 + \nu_1, -7 + \nu_2] + 40J[-1 + \nu_1, -6 + \nu_2]$$
$$- 72J[-1 + \nu_1, -5 + \nu_2] + 40J[-1 + \nu_1, -4 + \nu_2] + 40J[-1 + \nu_1, -3 + \nu_2]$$
$$- 72J[-1 + \nu_1, -2 + \nu_2] + 40J[-1 + \nu_1, -1 + \nu_2] - 8J[-1 + \nu_1, \nu_2]$$
$$+ J[\nu_1, -8 + \nu_2] - 8J[\nu_1, -7 + \nu_2] + 28J[\nu_1, -6 + \nu_2]$$
$$- 56J[\nu_1, -5 + \nu_2] + 70J[\nu_1, -4 + \nu_2] - 56J[\nu_1, -3 + \nu_2]$$
$$+ 28J[\nu_1, -2 + \nu_2] - 8J[\nu_1, -1 + \nu_2] + J[\nu_1, \nu_2]),$$

$$B_8[\nu_1, \nu_2] = -\frac{1}{8192}(35 \cdot 9J[-8 + \nu_1, \nu_2] - 72J[-7 + \nu_1, -1 + \nu_2] - 40J[-7 + \nu_1, \nu_2]$$
$$+ 252J[-6 + \nu_1, -2 + \nu_2] + 168J[-6 + \nu_1, -1 + \nu_2] + 60J[-6 + \nu_1, \nu_2]$$
$$- 504J[-5 + \nu_1, -3 + \nu_2] - 168J[-5 + \nu_1, -2 + \nu_2] - 72J[-5 + \nu_1, -1 + \nu_2]$$
$$- 24J[-5 + \nu_1, \nu_2] + 630J[-4 + \nu_1, -4 + \nu_2] - 280J[-4 + \nu_1, -3 + \nu_2]$$
$$- 60J[-4 + \nu_1, -2 + \nu_2] - 24J[-4 + \nu_1, -1 + \nu_2] - 10J[-4 + \nu_1, \nu_2]$$
$$- 504J[-3 + \nu_1, -5 + \nu_2] + 840J[-3 + \nu_1, -4 + \nu_2] - 240J[-3 + \nu_1, -3 + \nu_2]$$
$$- 48J[-3 + \nu_1, -2 + \nu_2] - 24J[-3 + \nu_1, -1 + \nu_2] - 24J[-3 + \nu_1, \nu_2]$$
$$+ 252J[-2 + \nu_1, -6 + \nu_2] - 840J[-2 + \nu_1, -5 + \nu_2] + 900J[-2 + \nu_1, -4 + \nu_2]$$
$$- 240J[-2 + \nu_1, -3 + \nu_2] - 60J[-2 + \nu_1, -2 + \nu_2] - 72J[-2 + \nu_1, -1 + \nu_2]$$
$$+ 60J[-2 + \nu_1, \nu_2] - 72J[-1 + \nu_1, -7 + \nu_2] + 392J[-1 + \nu_1, -6 + \nu_2]$$
$$- 840J[-1 + \nu_1, -5 + \nu_2] + 840J[-1 + \nu_1, -4 + \nu_2] - 280J[-1 + \nu_1, -3 + \nu_2]$$
$$- 168J[-1 + \nu_1, -2 + \nu_2] + 168J[-1 + \nu_1, -1 + \nu_2] - 40J[-1 + \nu_1, \nu_2] + 9J[\nu_1, -8 + \nu_2]$$
$$- 72J[\nu_1, -7 + \nu_2] + 252J[\nu_1, -6 + \nu_2] - 504J[\nu_1, -5 + \nu_2] + 630J[\nu_1, -4 + \nu_2] - 504J[\nu_1, -3 + \nu_2]$$
$$+ 252J[\nu_1, -2 + \nu_2] - 72J[\nu_1, -1 + \nu_2] + 9J[\nu_1, \nu_2]),$$

$$
\begin{aligned}
C_8 = \frac{1}{16384}\big(&105 \cdot 33 J[-8+\nu_1,\nu_2] - 264 J[-7+\nu_1,-1+\nu_2] - 72 J[-7+\nu_1,\nu_2] \\
&+ 924 J[-6+\nu_1,-2+\nu_2] + 168 J[-6+\nu_1,-1+\nu_2] + 28 J[-6+\nu_1,\nu_2] \\
&- 1848 J[-5+\nu_1,-3+\nu_2] + 504 J[-5+\nu_1,-2+\nu_2] + 56 J[-5+\nu_1,-1+\nu_2] \\
&+ 8 J[-5+\nu_1,\nu_2] + 2310 J[-4+\nu_1,-4+\nu_2] - 2520 J[-4+\nu_1,-3+\nu_2] \\
&+ 420 J[-4+\nu_1,-2+\nu_2] + 40 J[-4+\nu_1,-1+\nu_2] + 6 J[-4+\nu_1,\nu_2] \\
&- 1848 J[-3+\nu_1,-5+\nu_2] + 4200 J[-3+\nu_1,-4+\nu_2] - 2800 J[-3+\nu_1,-3+\nu_2] \\
&+ 400 J[-3+\nu_1,-2+\nu_2] + 40 J[-3+\nu_1,-1+\nu_2] + 8 J[-3+\nu_1,\nu_2] \\
&+ 924 J[-2+\nu_1,-6+\nu_2] - 3528 J[-2+\nu_1,-5+\nu_2] + 4900 J[-2+\nu_1,-4+\nu_2] \\
&- 2800 J[-2+\nu_1,-3+\nu_2] + 420 J[-2+\nu_1,-2+\nu_2] + 56 J[-2+\nu_1,-1+\nu_2] \\
&+ 28 J[-2+\nu_1,\nu_2] - 264 J[-1+\nu_1,-7+\nu_2] + 1512 J[-1+\nu_1,-6+\nu_2] \\
&- 3528 J[-1+\nu_1,-5+\nu_2] + 4200 J[-1+\nu_1,-4+\nu_2] - 2520 J[-1+\nu_1,-3+\nu_2] \\
&+ 504 J[-1+\nu_1,-2+\nu_2] + 168 J[-1+\nu_1,-1+\nu_2] - 72 J[-1+\nu_1,\nu_2] \\
&+ 33 J[\nu_1,-8+\nu_2] - 264 J[\nu_1,-7+\nu_2] + 924 J[\nu_1,-6+\nu_2] \\
&- 1848 J[\nu_1,-5+\nu_2] + 2310 J[\nu_1,-4+\nu_2] - 1848 J[\nu_1,-3+\nu_2] \\
&+ 924 J[\nu_1,-2+\nu_2] - 264 J[\nu_1,-1+\nu_2] + 33 J[\nu_1,\nu_2]\big),
\end{aligned}
$$

$$
\begin{aligned}
D_8 = -\frac{1}{8192}\big(&7 \cdot 429 J[-8+\nu_1,\nu_2] - 3432 J[-7+\nu_1,-1+\nu_2] - 264 J[-7+\nu_1,\nu_2] \\
&+ 12012 J[-6+\nu_1,-2+\nu_2] - 1848 J[-6+\nu_1,-1+\nu_2] - 84 J[-6+\nu_1,\nu_2] \\
&- 24024 J[-5+\nu_1,-3+\nu_2] + 16632 J[-5+\nu_1,-2+\nu_2] - 1512 J[-5+\nu_1,-1+\nu_2] \\
&- 56 J[-5+\nu_1,\nu_2] + 30030 J[-4+\nu_1,-4+\nu_2] - 46200 J[-4+\nu_1,-3+\nu_2] \\
&+ 18900 J[-4+\nu_1,-2+\nu_2] - 1400 J[-4+\nu_1,-1+\nu_2] - 50 J[-4+\nu_1,\nu_2] \\
&- 24024 J[-3+\nu_1,-5+\nu_2] + 64680 J[-3+\nu_1,-4+\nu_2] - 58800 J[-3+\nu_1,-3+\nu_2] \\
&+ 19600 J[-3+\nu_1,-2+\nu_2] - 1400 J[-3+\nu_1,-1+\nu_2] - 56 J[-3+\nu_1,\nu_2] \\
&+ 12012 J[-2+\nu_1,-6+\nu_2] - 49896 J[-2+\nu_1,-5+\nu_2] + 79380 J[-2+\nu_1,-4+\nu_2] \\
&- 58800 J[-2+\nu_1,-3+\nu_2] + 18900 J[-2+\nu_1,-2+\nu_2] - 1512 J[-2+\nu_1,-1+\nu_2] \\
&- 84 J[-2+\nu_1,\nu_2] - 3432 J[-1+\nu_1,-7+\nu_2] + 20328 J[-1+\nu_1,-6+\nu_2] \\
&- 49896 J[-1+\nu_1,-5+\nu_2] + 64680 J[-1+\nu_1,-4+\nu_2] - 46200 J[-1+\nu_1,-3+\nu_2] \\
&+ 16632 J[-1+\nu_1,-2+\nu_2] - 1848 J[-1+\nu_1,-1+\nu_2] - 264 J[-1+\nu_1,\nu_2] \\
&+ 429 J[\nu_1,-8+\nu_2] - 3432 J[\nu_1,-7+\nu_2] + 12012 J[\nu_1,-6+\nu_2] \\
&- 24024 J[\nu_1,-5+\nu_2] + 30030 J[\nu_1,-4+\nu_2] - 24024 J[\nu_1,-3+\nu_2] \\
&+ 12012 J[\nu_1,-2+\nu_2] - 3432 J[\nu_1,-1+\nu_2] + 429 J[\nu_1,\nu_2]\big),
\end{aligned}
$$

$$
\begin{aligned}
E_8 = \frac{1}{32768}\big(&6435 J[-8+\nu_1,\nu_2] - 51480 J[-7+\nu_1,-1+\nu_2] \\
&+ 3432 J[-7+\nu_1,\nu_2] + 180180 J[-6+\nu_1,-2+\nu_2] - 72072 J[-6+\nu_1,-1+\nu_2] \\
&+ 2772 J[-6+\nu_1,\nu_2] - 360360 J[-5+\nu_1,-3+\nu_2] + 360360 J[-5+\nu_1,-2+\nu_2] \\
&- 83160 J[-5+\nu_1,-1+\nu_2] + 2520 J[-5+\nu_1,\nu_2] + 450450 J[-4+\nu_1,-4+\nu_2] \\
&- 840840 J[-4+\nu_1,-3+\nu_2] + 485100 J[-4+\nu_1,-2+\nu_2] - 88200 J[-4+\nu_1,-1+\nu_2]
\end{aligned}
$$

$$
\begin{aligned}
&+ 2450J[-4+\nu_1,\nu_2] - 360360J[-3+\nu_1,-5+\nu_2] + 1081080J[-3+\nu_1,-4+\nu_2] \\
&- 1164240J[-3+\nu_1,-3+\nu_2] + 529200J[-3+\nu_1,-2+\nu_2] - 88200J[-3+\nu_1,-1+\nu_2] \\
&+ 2520J[-3+\nu_1,\nu_2] + 180180J[-2+\nu_1,-6+\nu_2] - 792792J[-2+\nu_1,-5+\nu_2] \\
&+ 1372140J[-2+\nu_1,-4+\nu_2] - 1164240J[-2+\nu_1,-3+\nu_2] + 485100J[-2+\nu_1,-2+\nu_2] \\
&- 83160J[-2+\nu_1,-1+\nu_2] + 2772J[-2+\nu_1,\nu_2] - 51480J[-1+\nu_1,-7+\nu_2] \\
&+ 312312J[-1+\nu_1,-6+\nu_2] - 792792J[-1+\nu_1,-5+\nu_2] + 1081080J[-1+\nu_1,-4+\nu_2] \\
&- 840840J[-1+\nu_1,-3+\nu_2] + 360360J[-1+\nu_1,-2+\nu_2] - 72072J[-1+\nu_1,-1+\nu_2] \\
&+ 3432J[-1+\nu_1,\nu_2] + 6435J[\nu_1,-8+\nu_2] - 51480J[\nu_1,-7+\nu_2] \\
&+ 180180J[\nu_1,-6+\nu_2] - 360360J[\nu_1,-5+\nu_2] + 450450J[\nu_1,-4+\nu_2] \\
&- 360360J[\nu_1,-3+\nu_2] + 180180J[\nu_1,-2+\nu_2] - 51480J[\nu_1,-1+\nu_2] \\
&+ 6435J[\nu_1,\nu_2]).
\end{aligned}
$$

## APPENDIX B: CALCULATION OF 13 CONTRIBUTIONS IN THE TAU MODEL

The 13-type loop correction due to contact operators from the exponential map is given by

$$
\delta P_{13} = (b_1 - b_\eta f\mu^2)P_{\text{lin}}(k) \int_{\mathbf{q}} P_{\text{lin}}(q)[(-\tau_0)^3(b_1^\tau + f\mu^2)Z_1^2(\mathbf{q}) + 4\tau_0^2 Z_2(\mathbf{k},\mathbf{q})Z_1(\mathbf{q})]. \tag{B1}
$$

The first integral $\propto \tau_0^3$ can be easily evaluated,

$$
\int_{\mathbf{q}} P_{\text{lin}}(q)(b_1^\tau + f(\hat{\mathbf{z}}\cdot\hat{\mathbf{q}})^2)^2 = \left((b_1^\tau)^2 + \frac{2b_1^\tau f}{3} + \frac{f^2}{5}\right) \int_0^\Lambda dq\, q^2 P_{\text{lin}}(q). \tag{B2}
$$

The rightmost term in Eq. (B1) has the following full expression:

$$
\begin{aligned}
\int_{\mathbf{q}} P_{\text{lin}}(q)(b_1^\tau + f(\hat{\mathbf{z}}\cdot\hat{\mathbf{q}})^2) &\left[\frac{b_2^\tau}{2} + b_{\mathcal{G}_2}^\tau\left(\frac{(\mathbf{q}\cdot\mathbf{k})^2}{k^2 q^2} - 1\right) + b_1^\tau F_2(\mathbf{q},\mathbf{k})\right. \\
&\left. + f\frac{(\hat{\mathbf{z}}\cdot(\mathbf{q}+\mathbf{k}))^2}{|\mathbf{q}+\mathbf{k}|^2}G_2(\mathbf{q},\mathbf{k}) + \frac{f(\hat{\mathbf{z}}\cdot(\mathbf{q}+\mathbf{k}))}{2}\left(\frac{\mu}{k}(b_1^\tau + f(\hat{\mathbf{z}}\cdot\hat{\mathbf{q}})^2) + \frac{(\hat{\mathbf{z}}\cdot\hat{\mathbf{q}})}{q}(b_1^\tau + f\mu^2)\right)\right].
\end{aligned}
$$

Let us compute these terms one by one,

$$
\int_{\mathbf{q}} P_{\text{lin}}(q)(b_1^\tau + f(\hat{\mathbf{z}}\cdot\hat{\mathbf{q}})^2)\frac{b_2^\tau}{2} = \frac{b_2^\tau}{2}\left(b_1^\tau + \frac{f}{3}\right)\sigma_\Lambda^2, \tag{B3}
$$

$$
\int_{\mathbf{q}} P_{\text{lin}}(q)(b_1^\tau + f(\hat{\mathbf{z}}\cdot\hat{\mathbf{q}})^2)b_{\mathcal{G}_2}^\tau\left(\frac{(\mathbf{q}\cdot\mathbf{k})^2}{k^2 q^2} - 1\right) = \left\{b_{\mathcal{G}_2}^\tau\left(-b_1^\tau\frac{2}{3} - \frac{4f}{15} + \frac{2\mu^2 f}{15}\right)\right\}\sigma_\Lambda^2, \tag{B4}
$$

$$
b_1^\tau \int_{\mathbf{q}} P_{\text{lin}}(q)(b_1^\tau + f(\hat{\mathbf{z}}\cdot\hat{\mathbf{q}})^2)\left[\frac{5}{7} + \frac{2}{7}(\hat{\mathbf{k}}\cdot\hat{\mathbf{q}})^2\right] = \left\{(b_1^\tau)^2\frac{17}{21} + \frac{9fb_1^\tau}{35} + \frac{4fb_1^\tau\mu^2}{105}\right\}\sigma_\Lambda^2, \tag{B5}
$$

$$
\begin{aligned}
&\int_{\mathbf{q}} P_{\text{lin}}(q)(b_1^\tau + f(\hat{\mathbf{z}}\cdot\hat{\mathbf{q}})^2)\frac{f(\hat{\mathbf{z}}\cdot(\mathbf{q}+\mathbf{k}))}{2}\left(\frac{\mu}{k}(b_1^\tau + f(\hat{\mathbf{z}}\cdot\hat{\mathbf{q}})^2) + \frac{(\hat{\mathbf{z}}\cdot\hat{\mathbf{q}})}{q}(b_1^\tau + f\mu^2)\right) \\
&= \left\{\mu^2\left(\frac{(b_1^\tau)^2 f}{2} + \frac{b_1^\tau f^2}{2} + \frac{f^3}{5}\right) + \frac{(b_1^\tau)^2 f}{6} + \frac{b_1^\tau f^2}{10}\right\}\sigma_\Lambda^2. \tag{B6}
\end{aligned}
$$

So far our analysis has been exact. In order to compute the UV contribution from the $G_2$ terms we need to use the high-$q$ expansion,

$$\int_{\mathbf{q}} P_{\text{lin}}(q)(b_1^\tau + f(\hat{\mathbf{z}} \cdot \hat{\mathbf{q}})^2)f(\hat{\mathbf{z}} \cdot \mathbf{q})^2 \left[\frac{3}{7} + \frac{4}{7}(\hat{\mathbf{k}} \cdot \hat{\mathbf{q}})^2\right]$$
$$= \left\{\frac{1}{735}f(133b_1^\tau + 75f) + \frac{8}{735}f\mu^2(7b_1^\tau + 6f)\right\}\sigma_\Lambda^2. \tag{B7}$$

Combining these terms together we find

$$\delta P_{13} = (b_1 - b_\eta f\mu^2)P_{\text{lin}}(k)[A_0 + \mu^2 A_2]\sigma_\Lambda^2, \tag{B8}$$

where

$$A_0 = -\frac{1}{735}\tau_0^2(-2380(b_1^\tau)^2 - 1470b_1^\tau b_2^\tau + 1960b_1^\tau b_{\mathcal{G}_2}^\tau - 1288b_1^\tau f - 490b_2^\tau f + 784b_{\mathcal{G}_2}^\tau f$$
$$- 300f^2 + 147b_1^\tau f^2(2 - \tau_0) + 490(b_1^\tau)^2 f(1 - \tau_0) + 735(b_1^\tau)^3\tau_0),$$
$$A_2 = -\frac{1}{735}(-336b_1^\tau f - 392b_{\mathcal{G}_2}^\tau f + 3f^2(-64 + 49f(-4 + \tau_0))$$
$$+ 490b_1^\tau f^2(-3 + \tau_0) + 735(b_1^\tau)^2 f(-2 + \tau_0))\tau_0^2. \tag{B9}$$

## APPENDIX C: FITS TO THE SIMULATIONS FOR $z = 3.2$

In this section we present results for the Sherwood simulation data analysis at $z = 3.2$. This redshift is somewhat higher than $z = 2.8$ used in the main text, so one may expect that the nonlinear corrections would be suppressed and the fit would be better down to smaller $k_{\text{max}}$. This is indeed the case. In Fig. 7 we show the results for four choices of $k_{\text{max}}$; 3, 4, 5, and 6 $h\,\text{Mpc}^{-1}$. We see that the posteriors for $k_{\text{max}} = 3, 4, 5\,h\,\text{Mpc}^{-1}$ are fully consistent with each other. The posteriors for $k_{\text{max}} = 3, 4$ are highly non-Gaussian, and even feature a multi-island structure for

certain parameters. This is likely due to a large number of parameters in the fit, which the data at a given $k_{\text{max}}$ cannot constrain.

The $k_{\text{max}} = 5\,h\,\text{Mpc}^{-1}$ posterior has significant overlap with those of the $k_{\text{max}} = 3, 4$ cases. In contrast, the $k_{\text{max}} = 5\,h\,\text{Mpc}^{-1}$ and $k_{\text{max}} = 6\,h\,\text{Mpc}^{-1}$ posteriors are in noticeable tension with each other in the $b_{\delta\eta} - b_\eta$ plane. This suggests that the $k_{\text{max}} = 6\,h\,\text{Mpc}^{-1}$ results are biased. Thus, we select $k_{\text{max}} = 5\,h\,\text{Mpc}^{-1}$ as a baseline for $z = 3.2$. As anticipates, this is larger than our baseline choice $k_{\text{max}} = 3\,h\,\text{Mpc}^{-1}$ for $z = 2.8$. The 1d marginalized posteriors for this case are shown in Table II.
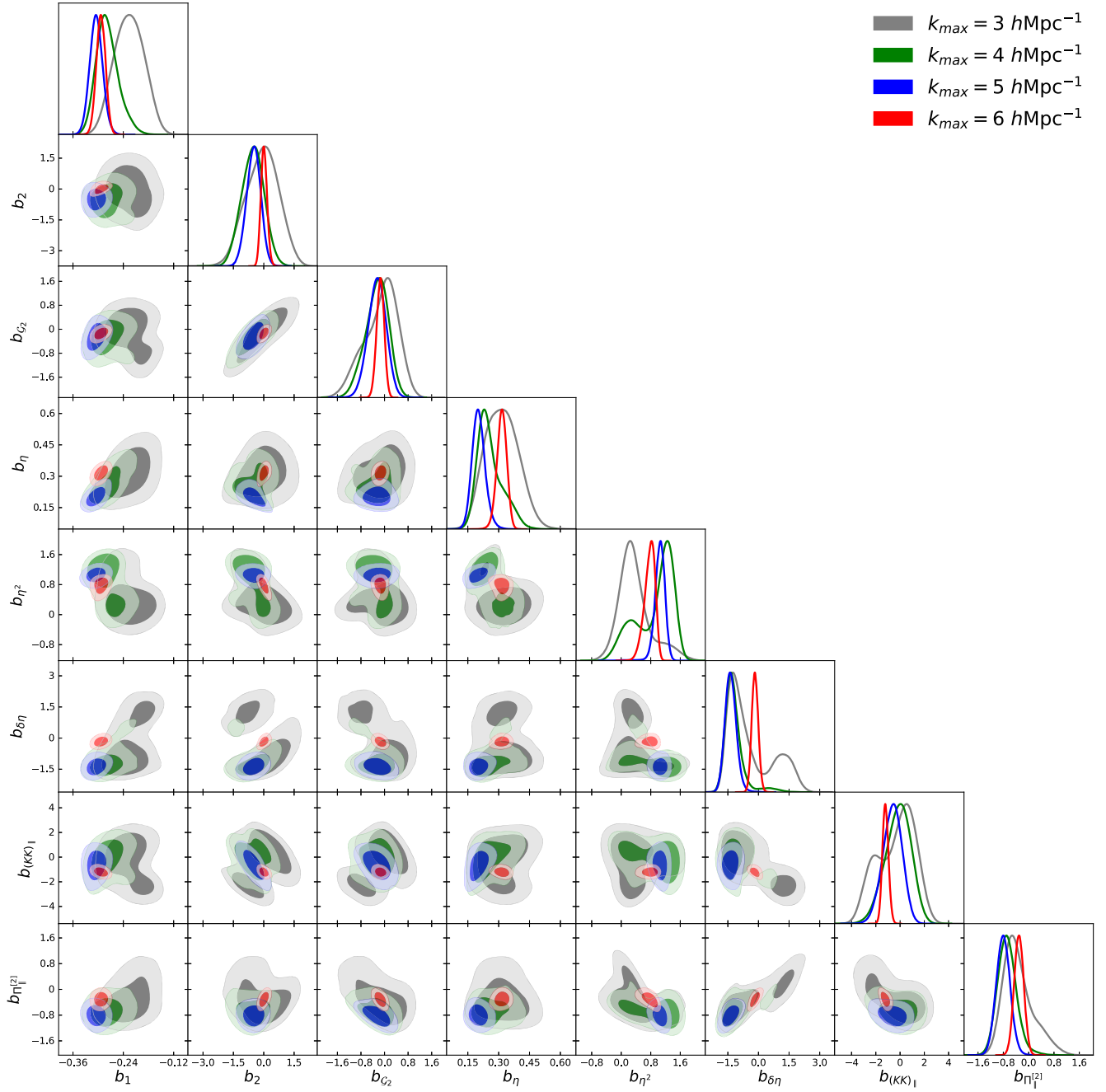
FIG. 7.   Triangle plot and marginalized projections for bias parameters of the EFT model for the Lyman alpha flux power spectrum of the Sherwood simulations at $z = 3.2$. We show results for four choices of $k_{\max}$; 3, 4, 5 and 6 $h\,\mathrm{Mpc}^{-1}$ (gray, green, blue, red, respectively).

TABLE II. Same as Table I, but for $z = 3.2$ and $k_{max} = 5\,h\,\mathrm{Mpc}^{-1}$ data.

| Parameters | Best-fit | Mean $\pm \sigma$ | 95% lower | 95% upper |
|---|---|---|---|---|
| $b_1$ | $-0.3049$ | $-0.3051^{+0.015}_{-0.016}$ | $-0.3362$ | $-0.2738$ |
| $b_\eta$ | $0.2037$ | $0.2026^{+0.029}_{-0.034}$ | $0.1402$ | $0.2679$ |
| $b_2$ | $-0.6221$ | $-0.5054^{+0.36}_{-0.34}$ | $-1.206$ | $0.1749$ |
| $b_{\mathcal{G}_2}$ | $-0.3887$ | $-0.2627^{+0.32}_{-0.29}$ | $-0.8758$ | $0.3404$ |
| $b_{\eta^2}$ | $1.052$ | $1.044^{+0.15}_{-0.12}$ | $0.764$ | $1.331$ |
| $b_{\delta\eta}$ | $-1.461$ | $-1.376^{+0.26}_{-0.28}$ | $-1.918$ | $-0.8311$ |
| $b_{(KK)_\parallel}$ | $-0.5014$ | $-0.6172^{+0.82}_{-0.73}$ | $-2.16$ | $0.8908$ |
| $b_{\Pi^{[2]}_\parallel}$ | $-0.81$ | $-0.8054^{+0.21}_{-0.22}$ | $-1.243$ | $-0.3755$ |
| $10^3 c_0/[h^{-1}\,\mathrm{Mpc}]^2$ | $7.91$ | $7.91^{+0.90}_{-0.90}$ | $6.12$ | $9.69$ |
| $10^3 c_2/[h^{-1}\,\mathrm{Mpc}]^2$ | $4.43$ | $4.43^{+0.57}_{-0.57}$ | $3.29$ | $5.57$ |
| $10^3 c_4/[h^{-1}\,\mathrm{Mpc}]^2$ | $-12.4$ | $-12.4^{+0.57}_{-0.57}$ | $-13.5$ | $-11.3$ |
| $b_{\Pi^{[3]}_\parallel}$ | $2.36$ | $2.36^{+0.09}_{-0.09}$ | $2.18$ | $2.55$ |
| $b_{\delta\Pi^{[2]}_\parallel}$ | $-5.15$ | $-5.15^{+0.11}_{-0.11}$ | $-5.36$ | $-4.94$ |
| $b_{(K\Pi^{[2]})_\parallel}$ | $-3.16$ | $-3.16^{+0.16}_{-0.16}$ | $-3.48$ | $-2.83$ |
| $b_{\eta\Pi^{[2]}_\parallel}$ | $0.13$ | $0.13^{+0.19}_{-0.19}$ | $-0.25$ | $0.52$ |

[1] L. Hernquist, N. Katz, D. H. Weinberg, and J. Miralda-Escude, The Lyman alpha forest in the cold dark matter model, Astrophys. J. Lett. **457,** L51 (1996).

[2] J. Miralda-Escude, R.-y. Cen, J. P. Ostriker, and M. Rauch, The Lyman alpha forest from gravitational collapse in the CDM + Lambda model, Astrophys. J. **471,** 582 (1996).

[3] R. A. C. Croft, D. H. Weinberg, N. Katz, and L. Hernquist, Intergalactic helium absorption in cold dark matter models, Astrophys. J. **488,** 532 (1997).

[4] R. A. C. Croft, D. H. Weinberg, N. Katz, and L. Hernquist, Recovery of the power spectrum of mass fluctuations from observations of the Lyman alpha forest, Astrophys. J. **495,** 44 (1998).

[5] P. McDonald, J. Miralda-Escude, M. Rauch, W. L. W. Sargent, T. A. Barlow, R. Cen, and J. P. Ostriker, The observed probability distribution function, power spectrum, and correlation function of the transmitted flux in the Lyα forest, Astrophys. J. **543,** 1 (2000).

[6] R. A. C. Croft, D. H. Weinberg, M. Bolte, S. Burles, L. Hernquist, N. Katz, D. Kirkman, and D. Tytler, Towards a precise measurement of matter clustering: Lyman alpha forest data at redshifts 2-4, Astrophys. J. **581,** 20 (2002).

[7] M. Zaldarriaga, U. Seljak, and L. Hui, Correlations across scales in the Lyman alpha forest: Testing the gravitational instability paradigm, Astrophys. J. **551,** 48 (2001).

[8] M. Zaldarriaga, L. Hui, and M. Tegmark, Constraints from the Lyman alpha forest power spectrum, Astrophys. J. **557,** 519 (2001).

[9] M. Zaldarriaga, R. Scoccimarro, and L. Hui, Inferring the linear power spectrum from the Lyman-alpha forest, Astrophys. J. **590,** 1 (2003).

[10] P. McDonald et al. (SDSS Collaboration), The linear theory power spectrum from the Lyman-alpha forest in the Sloan Digital Sky Survey, Astrophys. J. **635,** 761 (2005).

[11] P. McDonald et al. (SDSS Collaboration), The Lyα forest power spectrum from the Sloan Digital Sky Survey, Astrophys. J. Suppl. Ser. **163,** 80 (2006).

[12] U. Seljak, A. Slosar, and P. McDonald, Cosmological parameters from combining the Lyman-alpha forest with CMB, galaxy clustering and SN constraints, J. Cosmol. Astropart. Phys. 10 (2006) 014.

[13] A. Slosar, A. Font-Ribera, M. M. Pieri, J. Rich, J.-M. Le Goff, É. Aubourg et al., The Lyman-α forest in three dimensions: Measurements of large scale flux correlations from BOSS 1st-year data, J. Cosmol. Astropart. Phys. 09 (2011) 001.

[14] V. Iršič et al., The Lyman α forest power spectrum from the XQ-100 legacy survey, Mon. Not. R. Astron. Soc. **466,** 4332 (2017).

[15] S. Chabanier et al., The one-dimensional power spectrum from the SDSS DR14 Lyα forests, J. Cosmol. Astropart. Phys. 07 (2019) 017.

[16] S. Bird, M. Viel, and M. G. Haehnelt, Massive neutrinos and the non-linear matter power spectrum, Mon. Not. R. Astron. Soc. **420,** 2551 (2012).

[17] N. Palanque-Delabrouille *et al.*, Constraint on neutrino masses from SDSS-III/BOSS Lyα forest and other cosmological probes, J. Cosmol. Astropart. Phys. 02 (2015) 045.

[18] C. Pedersen, A. Font-Ribera, T. D. Kitching, P. McDonald, S. Bird, A. Slosar, K. K. Rogers, and A. Pontzen, Massive neutrinos and degeneracies in Lyman-alpha forest simulations, J. Cosmol. Astropart. Phys. 04 (2020) 025.

[19] M. Garny, T. Konstandin, L. Sagunski, and M. Viel, Neutrino mass bounds from confronting an effective model with BOSS Lyman-α data, J. Cosmol. Astropart. Phys. 03 (2021) 049.

[20] N. Afshordi, P. McDonald, and D. N. Spergel, Primordial black holes as dark matter: The power spectrum and evaporation of early structures, Astrophys. J. Lett. **594,** L71 (2003).

[21] C. Dvorkin, K. Blum, and M. Kamionkowski, Constraining dark matter-baryon scattering with linear cosmology, Phys. Rev. D **89,** 023519 (2014).

[22] M. Garny, T. Konstandin, L. Sagunski, and S. Tulin, Lyman-α forest constraints on interacting dark sectors, J. Cosmol. Astropart. Phys. 09 (2018) 011.

[23] L. Fuß and M. Garny, Decaying dark matter and Lyman-α forest constraints, J. Cosmol. Astropart. Phys. 10 (2023) 020.

[24] S. Goldstein, J. C. Hill, V. Iršič, and B. D. Sherwin, Canonical Hubble-tension-resolving early dark energy cosmologies are inconsistent with the Lyman-α forest, Phys. Rev. Lett. **131,** 201001 (2023).

[25] M. Viel, J. Lesgourgues, M. G. Haehnelt, S. Matarrese, and A. Riotto, Constraining warm dark matter candidates including sterile neutrinos and light gravitinos with WMAP and the Lyman-alpha forest, Phys. Rev. D **71,** 063534 (2005).

[26] U. Seljak, A. Makarov, P. McDonald, and H. Trac, Can sterile neutrinos be the dark matter?, Phys. Rev. Lett. **97,** 191303 (2006).

[27] A. Boyarsky, J. Lesgourgues, O. Ruchayskiy, and M. Viel, Lyman-alpha constraints on warm and on warm-plus-cold dark matter models, J. Cosmol. Astropart. Phys. 05 (2009) 012.

[28] M. Viel, G. D. Becker, J. S. Bolton, and M. G. Haehnelt, Warm dark matter as a solution to the small scale crisis: New constraints from high redshift Lyman-α forest data, Phys. Rev. D **88,** 043502 (2013).

[29] J. Baur, N. Palanque-Delabrouille, C. Yèche, C. Magneville, and M. Viel, Lyman-alpha forests cool warm dark matter, J. Cosmol. Astropart. Phys. 08 (2016) 012.

[30] A. Garzilli, A. Boyarsky, and O. Ruchayskiy, Cutoff in the Lyman α forest power spectrum: Warm IGM or warm dark matter?, Phys. Lett. B **773,** 258 (2017).

[31] J. Baur, N. Palanque-Delabrouille, C. Yeche, A. Boyarsky, O. Ruchayskiy, E. Armengaud, and J. Lesgourgues, Constraints from Ly-α forests on non-thermal dark matter including resonantly-produced sterile neutrinos, J. Cosmol. Astropart. Phys. 12 (2017) 013.

[32] A. Boyarsky, M. Drewes, T. Lasserre, S. Mertens, and O. Ruchayskiy, Sterile neutrino dark matter, Prog. Part. Nucl. Phys. **104,** 1 (2019).

[33] N. Palanque-Delabrouille, C. Yèche, N. Schöneberg, J. Lesgourgues, M. Walther, S. Chabanier, and E. Armengaud, Hints, neutrino bounds and WDM constraints from SDSS DR14 Lyman-α and Planck full-survey data, J. Cosmol. Astropart. Phys. 04 (2020) 038.

[34] A. Garzilli, A. Magalich, O. Ruchayskiy, and A. Boyarsky, How to constrain warm dark matter with the Lyman-α forest, Mon. Not. R. Astron. Soc. **502,** 2356 (2021).

[35] L. Hui, J. P. Ostriker, S. Tremaine, and E. Witten, Ultralight scalars as cosmological dark matter, Phys. Rev. D **95,** 043541 (2017).

[36] V. Iršič, M. Viel, M. G. Haehnelt, J. S. Bolton, and G. D. Becker, First constraints on fuzzy dark matter from Lyman-α forest data and hydrodynamical simulations, Phys. Rev. Lett. **119,** 031302 (2017).

[37] K. K. Rogers and H. V. Peiris, Strong bound on canonical ultralight axion dark matter from the Lyman-alpha forest, Phys. Rev. Lett. **126,** 071302 (2021).

[38] A. Slosar *et al.*, Measurement of baryon acoustic oscillations in the Lyman-alpha forest fluctuations in BOSS data release 9, J. Cosmol. Astropart. Phys. 04 (2013) 026.

[39] A. Font-Ribera *et al.* (BOSS Collaboration), Quasar-Lyman α forest cross-correlation from BOSS DR11: Baryon acoustic oscillations, J. Cosmol. Astropart. Phys. 05 (2014) 027.

[40] E. Aubourg *et al.*, Cosmological implications of baryon acoustic oscillation measurements, Phys. Rev. D **92,** 123516 (2015).

[41] H. du Mas des Bourboux *et al.*, The completed SDSS-IV extended baryon oscillation spectroscopic survey: Baryon acoustic oscillations with Lyα forests, Astrophys. J. **901,** 153 (2020).

[42] A. Slosar *et al.*, The Lyman-alpha forest in three dimensions: measurements of large scale flux correlations from BOSS 1st-year data, J. Cosmol. Astropart. Phys. 09 (2011) 001.

[43] A. Cuceu, A. Font-Ribera, B. Joachimi, and S. Nadathur, Cosmology beyond BAO from the 3D distribution of the Lyman-α forest, Mon. Not. R. Astron. Soc. **506,** 5439 (2021).

[44] A. Cuceu, A. Font-Ribera, S. Nadathur, B. Joachimi, and P. Martini, Constraints on the cosmic expansion rate at redshift 2.3 from the Lyman-α forest, Phys. Rev. Lett. **130,** 191003 (2023).

[45] C. Gordon *et al.*, 3D correlations in the Lyman-α forest from early DESI data, J. Cosmol. Astropart. Phys. 11 (2023) 045.

[46] R. A. C. Croft *et al.* (BOSS Collaboration), Large-scale clustering of Lyman α emission intensity from SDSS/BOSS, Mon. Not. R. Astron. Soc. **457,** 3541 (2016).

[47] A. Aghamousa *et al.* (DESI Collaboration), The DESI experiment part I: Science, targeting, and survey design, arXiv:1611.00036.

[48] C. Ramirez-Perez *et al.* (DESI Collaboration), The Lyman-α forest catalog from the dark energy spectroscopic instrument early data release, arXiv:2306.06312.

[49] A. Borde, N. Palanque-Delabrouille, G. Rossi, M. Viel, J. S. Bolton, C. Yèche, J.-M. LeGoff, and J. Rich, New approach for precise computation of Lyman-α forest power

spectrum with hydrodynamical simulations, J. Cosmol. Astropart. Phys. 07 (2014) 005.

[50] G. Rossi, N. Palanque-Delabrouille, A. Borde, M. Viel, C. Yeche, J. S. Bolton, J. Rich, and J.-M. Le Goff, Suite of hydrodynamical simulations for the Lyman-$\alpha$ forest with massive neutrinos, Astron. Astrophys. **567,** A79 (2014).

[51] S. Bird, M. Vogelsberger, M. Haehnelt, D. Sijacki, S. Genel, P. Torrey, V. Springel, and L. Hernquist, Damped Lyman-$\alpha$ absorbers as a probe of stellar feedback, Mon. Not. R. Astron. Soc. **445,** 2313 (2014).

[52] J. S. Bolton, E. Puchwein, D. Sijacki, M. G. Haehnelt, T.-S. Kim, A. Meiksin, J. A. Regan, and M. Viel, The Sherwood simulation suite: Overview and data comparisons with the Lyman $\alpha$ forest at redshifts $2 \leq z \leq 5$, Mon. Not. R. Astron. Soc. **464,** 897 (2017).

[53] A. Arinyo-i Prats, J. Miralda-Escudé, M. Viel, and R. Cen, The non-linear power spectrum of the Lyman alpha forest, J. Cosmol. Astropart. Phys. 12 (2015) 017.

[54] L. Anderson, A. Pontzen, A. Font-Ribera, F. Villaescusa-Navarro, K. K. Rogers, and S. Genel, Cosmological hydrodynamic simulations with suppressed variance in the Ly$\alpha$ forest power spectrum, Astrophys. J. **871,** 144 (2019).

[55] A. Smith, R. Kannan, E. Garaldi, M. Vogelsberger, R. Pakmor, V. Springel, and L. Hernquist, The THESAN project: Lyman-$\alpha$ emission and transmission during the Epoch of reionization, Mon. Not. R. Astron. Soc. **512,** 3243 (2022).

[56] M. T. Tillman *et al.*, An exploration of AGN and stellar feedback effects in the intergalactic medium via the low redshift Lyman-$\alpha$ forest, Astron. J. **166,** 228 (2023).

[57] B. Greig, E. Komatsu, and J. S. B. Wyithe, Cosmology from clustering of Lyman-alpha galaxies: Breaking non-gravitational Lyman-alpha radiative transfer degeneracies using the bispectrum, Mon. Not. R. Astron. Soc. **431,** 1777 (2013).

[58] J. J. Givans and C. M. Hirata, Redshift-space streaming velocity effects on the Lyman-$\alpha$ forest baryon acoustic oscillation scale, Phys. Rev. D **102,** 023515 (2020).

[59] S.-F. Chen, Z. Vlah, and M. White, The Ly$\alpha$ forest flux correlation function: a perturbation theory perspective, J. Cosmol. Astropart. Phys. 05 (2021) 053.

[60] J. J. Givans, A. Font-Ribera, A. Slosar, L. Seeyave, C. Pedersen, K. K. Rogers, M. Garny, D. Blas, and V. Iršič, Non-linearities in the Lyman-$\alpha$ forest and in its cross-correlation with dark matter halos, J. Cosmol. Astropart. Phys. 09 (2022) 070.

[61] N. Aghanim *et al.* (Planck Collaboration), Planck 2018 results. VI. Cosmological parameters, Astron. Astrophys. **641,** A6 (2020).

[62] R. Murgia, V. Iršič, and M. Viel, Novel constraints on noncold, nonthermal dark matter from Lyman-$\alpha$ forest data, Phys. Rev. D **98,** 083540 (2018).

[63] D. C. Hooper, N. Schöneberg, R. Murgia, M. Archidiacono, J. Lesgourgues, and M. Viel, One likelihood to bind them all: Lyman-$\alpha$ constraints on non-standard dark matter, J. Cosmol. Astropart. Phys. 10 (2022) 032.

[64] K. K. Rogers, H. V. Peiris, A. Pontzen, S. Bird, L. Verde, and A. Font-Ribera, Bayesian emulator optimisation for cosmology: Application to the Lyman-alpha forest, J. Cosmol. Astropart. Phys. 02 (2019) 031.

[65] S. Bird, K. K. Rogers, H. V. Peiris, L. Verde, A. Font-Ribera, and A. Pontzen, An emulator for the Lyman-alpha forest, J. Cosmol. Astropart. Phys. 02 (2019) 050.

[66] C. Pedersen, A. Font-Ribera, K. K. Rogers, P. McDonald, H. V. Peiris, A. Pontzen, and A. Slosar, An emulator for the Lyman-$\alpha$ forest in beyond-$\Lambda$CDM cosmologies, J. Cosmol. Astropart. Phys. 05 (2021) 033.

[67] M. M. Ivanov, M. Simonović, and M. Zaldarriaga, Cosmological parameters from the BOSS galaxy power spectrum, J. Cosmol. Astropart. Phys. 05 (2020) 042.

[68] G. D'Amico, J. Gleyzes, N. Kokron, D. Markovic, L. Senatore, P. Zhang, F. Beutler, and H. Gil-Marín, The cosmological analysis of the SDSS/BOSS data from the effective field theory of large-scale structure, J. Cosmol. Astropart. Phys. 05 (2020) 005.

[69] M. M. Ivanov, M. Simonović, and M. Zaldarriaga, Cosmological parameters and neutrino masses from the final Planck and full-shape BOSS data, Phys. Rev. D **101,** 083504 (2020).

[70] A. Chudaykin, K. Dolgikh, and M. M. Ivanov, Constraints on the curvature of the Universe and dynamical dark energy from the full-shape and BAO data, Phys. Rev. D **103,** 023507 (2021).

[71] M. M. Ivanov, E. McDonough, J. C. Hill, M. Simonović, M. W. Toomey, S. Alexander, and M. Zaldarriaga, Constraining early dark energy with large-scale structure, Phys. Rev. D **102,** 103502 (2020).

[72] O. H. E. Philcox and M. M. Ivanov, BOSS DR12 full-shape cosmology: $\Lambda$CDM constraints from the large-scale galaxy power spectrum and bispectrum monopole, Phys. Rev. D **105,** 043517 (2022).

[73] M. M. Ivanov, Cosmological constraints from the power spectrum of eBOSS emission line galaxies, Phys. Rev. D **104,** 103514 (2021).

[74] M. White *et al.*, Cosmological constraints from the tomographic cross-correlation of DESI luminous red galaxies and Planck CMB lensing, J. Cosmol. Astropart. Phys. 02 (2022) 007.

[75] S.-F. Chen, Z. Vlah, and M. White, A new analysis of galaxy 2-point functions in the BOSS survey, including full-shape information and post-reconstruction BAO, J. Cosmol. Astropart. Phys. 02 (2022) 008.

[76] S.-F. Chen, M. White, J. DeRose, and N. Kokron, Cosmological analysis of three-dimensional BOSS galaxy clustering and Planck CMB lensing cross correlations via Lagrangian perturbation theory, J. Cosmol. Astropart. Phys. 07 (2022) 041.

[77] A. Chudaykin and M. M. Ivanov, Cosmological constraints from the power spectrum of eBOSS quasars, Phys. Rev. D **107,** 043518 (2023).

[78] M. M. Ivanov, O. H. E. Philcox, G. Cabass, T. Nishimichi, M. Simonović, and M. Zaldarriaga, Cosmology with the galaxy bispectrum multipoles: Optimal estimation and application to BOSS data, Phys. Rev. D **107,** 083515 (2023).

[79] U. Seljak, Bias, redshift space distortions, and primordial non-Gaussianity of nonlinear transformations: application to Lyman alpha forest, J. Cosmol. Astropart. Phys. 03 (2012) 004.

[80] A. M. Cieplak and A. Slosar, Towards physics responsible for large-scale Lyman-$\alpha$ forest bias parameters, J. Cosmol. Astropart. Phys. 03 (2016) 016.

[81] D. Baumann, A. Nicolis, L. Senatore, and M. Zaldarriaga, Cosmological non-linearities as an effective fluid, J. Cosmol. Astropart. Phys. 07 (2012) 051.

[82] J. J. M. Carrasco, M. P. Hertzberg, and L. Senatore, The effective field theory of cosmological large scale structures, J. High Energy Phys. 09 (2012) 082.

[83] V. Desjacques, D. Jeong, and F. Schmidt, Large-scale galaxy bias, Phys. Rep. 733, 1 (2018).

[84] G. Cabass, M. M. Ivanov, M. Lewandowski, M. Mirbabayi, and M. Simonović, Snowmass white paper: Effective field theories in cosmology, Phys. Dark Universe 40, 101193 (2023).

[85] M. M. Ivanov, Effective field theory for large scale structure, arXiv:2212.08488.

[86] V. Desjacques, D. Jeong, and F. Schmidt, The galaxy power spectrum and bispectrum in redshift space, J. Cosmol. Astropart. Phys. 12 (2018) 035.

[87] C. M. Hirata, Tidal alignments as a contaminant of redshift space distortions, Mon. Not. R. Astron. Soc. 399, 1074 (2009).

[88] F. Bernardeau, S. Colombi, E. Gaztanaga, and R. Scoccimarro, Large scale structure of the universe and cosmological perturbation theory, Phys. Rep. 367, 1 (2002).

[89] Z. Zheng, R. Cen, H. Trac, and J. Miralda-Escude, Radiative transfer modeling of Lyman alpha emitters. II. New effects in galaxy clustering, Astrophys. J. 726, 38 (2010).

[90] S. Wyithe and M. Dijkstra, Non-gravitational contributions to the clustering of Ly$\alpha$ selected galaxies: Implications for cosmological surveys, Mon. Not. R. Astron. Soc. 415, 3929 (2011).

[91] D. Martens, C. M. Hirata, A. J. Ross, and X. Fang, A radial measurement of the galaxy tidal alignment magnitude with BOSS data, Mon. Not. R. Astron. Soc. 478, 711 (2018).

[92] A. Obuljen, W. J. Percival, and N. Dalal, Detection of anisotropic galaxy assembly bias in BOSS DR12, J. Cosmol. Astropart. Phys. 10 (2020) 058.

[93] M. Simonovic, T. Baldauf, M. Zaldarriaga, J. J. Carrasco, and J. A. Kollmeier, Cosmological perturbation theory using the FFTLog: Formalism and connection to QFT loop integrals, J. Cosmol. Astropart. Phys. 04 (2018) 030.

[94] A. Chudaykin, M. M. Ivanov, O. H. E. Philcox, and M. Simonović, Nonlinear perturbation theory extension of the Boltzmann code CLASS, Phys. Rev. D 102, 063533 (2020).

[95] M. Rauch, The Lyman alpha forest in the spectra of quasistellar objects, Annu. Rev. Astron. Astrophys. 36, 267 (1998).

[96] A. Loeb and S. R. Furlanetto, *The First Galaxies in the Universe* (Princeton University Press, Princeton, NJ, 2013), https://ui.adsabs.harvard.edu/abs/2013fgu..book.....L/abstract.

[97] D. Blas, M. M. Ivanov, and S. Sibiryakov, Testing Lorentz invariance of dark matter, J. Cosmol. Astropart. Phys. 10 (2012) 057.

[98] B. Audren, D. Blas, M. M. Ivanov, J. Lesgourgues, and S. Sibiryakov, Cosmological constraints on deviations from Lorentz invariance in gravity and dark matter, J. Cosmol. Astropart. Phys. 03 (2015) 016.

[99] J. E. Gunn and B. A. Peterson, On the density of neutral hydrogen in intergalactic space, Astrophys. J. 142, 1633 (1965).

[100] S. Alam *et al.* (eBOSS Collaboration), Completed SDSS-IV extended baryon oscillation spectroscopic survey: Cosmological implications from two decades of spectroscopic surveys at the Apache Point Observatory, Phys. Rev. D 103, 083533 (2021).

[101] N. Y. Gnedin and L. Hui, Probing the universe with the Lyman alpha forest: 1. Hydrodynamics of the low density IGM, Mon. Not. R. Astron. Soc. 296, 44 (1998).

[102] L. Hui and N. Y. Gnedin, Equation of state of the photo-ionized intergalactic medium, Mon. Not. R. Astron. Soc. 292, 27 (1997).

[103] T. Theuns, J. Schaye, and M. Haehnelt, Broadening of QSO Ly$\alpha$ forest absorbers, Mon. Not. R. Astron. Soc. 315, 600 (2000).

[104] A. Pontzen, Scale-dependent bias in the baryonic-acoustic-oscillation-scale intergalactic neutral hydrogen, Phys. Rev. D 89, 083010 (2014).

[105] S. Gontcho A Gontcho, J. Miralda-Escudé, and N. G. Busca, On the effect of the ionizing background on the Ly$\alpha$ forest autocorrelation function, Mon. Not. R. Astron. Soc. 442, 187 (2014).

[106] A. D'Aloisio, M. McQuinn, and H. Trac, Large opacity variations in the high-redshift Ly$\alpha$ forest: The signature of relic temperature fluctuations from patchy reionization, Astrophys. J. Lett. 813, L38 (2015).

[107] P. Montero-Camacho, C. M. Hirata, P. Martini, and K. Honscheid, Impact of inhomogeneous reionization on the Lyman-$\alpha$ forest, Mon. Not. R. Astron. Soc. 487, 1047 (2019).

[108] G. Cabass and F. Schmidt, A new scale in the bias expansion, J. Cosmol. Astropart. Phys. 05 (2019) 031.

[109] E. Pajer and M. Zaldarriaga, On the renormalization of the effective field theory of large scale structures, J. Cosmol. Astropart. Phys. 08 (2013) 037.

[110] D. Blas, M. Garny, and T. Konstandin, Cosmological perturbation theory at three-loop order, J. Cosmol. Astropart. Phys. 01 (2014) 010.

[111] T. Konstandin, R. A. Porto, and H. Rubira, The effective field theory of large scale structure at three loops, J. Cosmol. Astropart. Phys. 11 (2019) 027.

[112] S. Pueblas and R. Scoccimarro, Generation of vorticity and velocity dispersion by orbit crossing, Phys. Rev. D 80, 043504 (2009).

[113] M. Schmittfull, M. Simonović, M. M. Ivanov, O. H. E. Philcox, and M. Zaldarriaga, Modeling galaxies in redshift space at the field level, J. Cosmol. Astropart. Phys. 05 (2021) 059.

[114] G. Cabass, M. M. Ivanov, O. H. E. Philcox, M. Simonović, and M. Zaldarriaga, Constraints on single-field inflation from the BOSS galaxy survey, Phys. Rev. Lett. 129, 021301 (2022).

[115] G. Cabass, M. M. Ivanov, O. H. E. Philcox, M. Simonović, and M. Zaldarriaga, Constraints on multi-field inflation from the BOSS galaxy survey, Phys. Rev. D 106, 043506 (2022).

[116] L. Senatore, Bias in the effective field theory of large scale structures, J. Cosmol. Astropart. Phys. 11 (2015) 007.

[117] V. Assassi, D. Baumann, D. Green, and M. Zaldarriaga, Renormalized halo bias, J. Cosmol. Astropart. Phys. 08 (2014) 056.

[118] M. Mirbabayi, F. Schmidt, and M. Zaldarriaga, Biased tracers and time evolution, J. Cosmol. Astropart. Phys. 07 (2015) 030.

[119] T. Lazeyras and F. Schmidt, Beyond LIMD bias: A measurement of the complete set of third-order halo bias parameters, J. Cosmol. Astropart. Phys. 09 (2018) 008.

[120] T. Lazeyras and F. Schmidt, A robust measurement of the first higher-derivative bias of dark matter halos, J. Cosmol. Astropart. Phys. 11 (2019) 041.

[121] P. U. Sanderbeck, V. Iršič, M. McQuinn, and A. Meiksin, Estimates for the impact of ultraviolet background fluctuations on galaxy clustering measurements, Mon. Not. R. Astron. Soc. **485,** 5059 (2019).

[122] L. Senatore and M. Zaldarriaga, Redshift space distortions in the effective field theory of large scale structures, arXiv:1409.1225.

[123] M. Lewandowski, L. Senatore, F. Prada, C. Zhao, and C.-H. Chuang, EFT of large scale structures in redshift space, Phys. Rev. D **97,** 063526 (2018).

[124] N. Kaiser, Clustering in real space and in redshift space, Mon. Not. R. Astron. Soc. **227,** 1 (1987).

[125] J. J. M. Carrasco, S. Foreman, D. Green, and L. Senatore, The 2-loop matter power spectrum and the IR-safe integrand, J. Cosmol. Astropart. Phys. 07 (2014) 056.

[126] A. Perko, L. Senatore, E. Jennings, and R. H. Wechsler, Biased tracers in redshift space in the EFT of large-scale structure, arXiv:1610.09321.

[127] L. Senatore and M. Zaldarriaga, The IR-resummed effective field theory of large scale structures, J. Cosmol. Astropart. Phys. 02 (2015) 013.

[128] Z. Vlah, U. Seljak, M. Y. Chu, and Y. Feng, Perturbation theory, effective field theory, and oscillations in the power spectrum, J. Cosmol. Astropart. Phys. 03 (2016) 057.

[129] T. Baldauf, M. Mirbabayi, M. Simonović, and M. Zaldarriaga, Equivalence principle and the baryon acoustic peak, Phys. Rev. D **92,** 043514 (2015).

[130] D. Blas, M. Garny, M. M. Ivanov, and S. Sibiryakov, Time-sliced perturbation theory for large scale structure I: General formalism, J. Cosmol. Astropart. Phys. 07 (2016) 052.

[131] D. Blas, M. Garny, M. M. Ivanov, and S. Sibiryakov, Time-sliced perturbation theory II: Baryon acoustic oscillations and infrared resummation, J. Cosmol. Astropart. Phys. 07 (2016) 028.

[132] M. M. Ivanov and S. Sibiryakov, Infrared resummation for biased tracers in redshift space, J. Cosmol. Astropart. Phys. 07 (2018) 053.

[133] A. Vasudevan, M. M. Ivanov, S. Sibiryakov, and J. Lesgourgues, Time-sliced perturbation theory with primordial non-Gaussianity and effects of large bulk flows on inflationary oscillating features, J. Cosmol. Astropart. Phys. 09 (2019) 037.

[134] J. E. McEwen, X. Fang, C. M. Hirata, and J. A. Blazek, FAST-PT: A novel algorithm to calculate convolution integrals in cosmological perturbation theory, J. Cosmol. Astropart. Phys. 09 (2016) 015.

[135] X. Fang, J. A. Blazek, J. E. McEwen, and C. M. Hirata, FAST-PT II: An algorithm to calculate convolution integrals of general tensor quantities in cosmological perturbation theory, J. Cosmol. Astropart. Phys. 02 (2017) 030.

[136] S.-F. Chen, Z. Vlah, and M. White, Consistent modeling of velocity statistics and redshift-space distortions in one-loop perturbation theory, J. Cosmol. Astropart. Phys. 07 (2020) 062.

[137] D. Blas, M. Garny, and T. Konstandin, On the non-linear scale of cosmological perturbation theory, J. Cosmol. Astropart. Phys. 09 (2013) 024.

[138] D. Wadekar and R. Scoccimarro, The galaxy power spectrum multipoles covariance in perturbation theory, Phys. Rev. D **102,** 123517 (2020).

[139] D. Wadekar, M. M. Ivanov, and R. Scoccimarro, Cosmological constraints from BOSS with analytic covariance matrices, Phys. Rev. D **102,** 123521 (2020).

[140] O. H. E. Philcox, M. M. Ivanov, M. Zaldarriaga, M. Simonovic, and M. Schmittfull, Fewer mocks and less noise: Reducing the dimensionality of cosmological observables with subspace projections, Phys. Rev. D **103,** 043508 (2021).

[141] T. Baldauf, M. Mirbabayi, M. Simonović, and M. Zaldarriaga, LSS constraints with controlled theoretical uncertainties, arXiv:1602.00674.

[142] A. Chudaykin and M. M. Ivanov, Measuring neutrino masses with large-scale structure: Euclid forecast with controlled theoretical error, J. Cosmol. Astropart. Phys. 11 (2019) 034.

[143] A. Chudaykin, M. M. Ivanov, and M. Simonović, Optimizing large-scale structure data analysis with the theoretical error likelihood, Phys. Rev. D **103,** 043525 (2021).

[144] M. M. Ivanov, O. H. E. Philcox, T. Nishimichi, M. Simonović, M. Takada, and M. Zaldarriaga, Precision analysis of the redshift-space galaxy bispectrum, Phys. Rev. D **105,** 063512 (2022).

[145] T. Nishimichi, G. D'Amico, M. M. Ivanov, L. Senatore, M. Simonović, M. Takada, M. Zaldarriaga, and P. Zhang, Blinded challenge for precision cosmology with large-scale structure: Results from effective field theory for the redshift-space galaxy power spectrum, Phys. Rev. D **102,** 123541 (2020).

[146] M. M. Ivanov, O. H. E. Philcox, M. Simonović, M. Zaldarriaga, T. Nischimichi, and M. Takada, Cosmological constraints without nonlinear redshift-space distortions, Phys. Rev. D **105,** 043531 (2022).

[147] B. Audren, J. Lesgourgues, K. Benabed, and S. Prunet, Conservative constraints on early cosmology: An illustration of the Monte Python cosmological parameter inference code, J. Cosmol. Astropart. Phys. 02 (2013) 001.

[148] T. Brinckmann and J. Lesgourgues, MontePython 3: Boosted MCMC sampler and other features, Phys. Dark Universe **24,** 100260 (2019).

[149] A. Lewis, GetDist: A Python package for analysing Monte Carlo samples, arXiv:1910.13970.

[150] L. Mercolli and E. Pajer, On the velocity in the effective field theory of large scale structures, J. Cosmol. Astropart. Phys. 03 (2014) 006.

[151] S. L. Lumsden, A. F. Heavens, and J. A. Peacock, The clustering of peaks in a random Gaussian field, Mon. Not. R. Astron. Soc. **238,** 293 (1989).

[152] A. Barreira, T. Lazeyras, and F. Schmidt, Galaxy bias from forward models: Linear and second-order bias of IllustrisTNG galaxies, J. Cosmol. Astropart. Phys. 08 (2021) 029.

[153] T. Lazeyras, A. Barreira, and F. Schmidt, Assembly bias in quadratic bias parameters of dark matter halos from forward modeling, J. Cosmol. Astropart. Phys. 10 (2021) 063.

[154] G. Cabass, M. M. Ivanov, O. H. E. Philcox, M. Simonovic, and M. Zaldarriaga, Constraining single-field inflation with megaMapper, Phys. Lett. B **841,** 137912 (2023).

[155] O. H. E. Philcox, M. M. Ivanov, G. Cabass, M. Simonović, M. Zaldarriaga, and T. Nishimichi, Cosmology with the redshift-space galaxy bispectrum monopole at one-loop order, Phys. Rev. D **106,** 043530 (2022).

[156] G. D'Amico, Y. Donath, M. Lewandowski, L. Senatore, and P. Zhang, The one-loop bispectrum of galaxies in redshift space from the effective field theory of large-scale structure, arXiv:2211.17130.

[157] S. S. Tie, D. H. Weinberg, P. Martini, W. Zhu, S. Peirani, T. Suarez, and S. Colombi, UV background fluctuations and three-point correlations in the large-scale clustering of the Lyman $\alpha$ forest, Mon. Not. R. Astron. Soc. **487,** 5346 (2019).

[158] T.-T. Fang and M. J. White, Probing the statistics of the temperature—density relation of the IGM, Astrophys. J. Lett. **606,** L9 (2004).

[159] A. Font-Ribera et al., The large-scale Quasar-Lyman $\alpha$ forest cross-correlation from BOSS, J. Cosmol. Astropart. Phys. 05 (2013) 018.

[160] R. A. Porto, L. Senatore, and M. Zaldarriaga, The Lagrangian-space effective field theory of large scale structures, J. Cosmol. Astropart. Phys. 05 (2014) 022.

[161] Z. Vlah, M. White, and A. Aviles, A Lagrangian effective field theory, J. Cosmol. Astropart. Phys. 09 (2015) 014.

[162] Z. Vlah, E. Castorina, and M. White, The Gaussian streaming model and convolution Lagrangian effective field theory, J. Cosmol. Astropart. Phys. 12 (2016) 007.

[163] Z. Vlah and M. White, Exploring redshift-space distortions in large-scale structure, J. Cosmol. Astropart. Phys. 03 (2019) 007.

[164] S.-F. Chen, Z. Vlah, E. Castorina, and M. White, Redshift-space distortions in Lagrangian perturbation theory, J. Cosmol. Astropart. Phys. 03 (2021) 100.